TAMPEREEN TEKNILLINEN YLIOPISTO
TAMPERE UNIVERSITY OF TECHNOLOGY

Jean-Baptiste Izard

Development of Remote Handling Technologies Tolerant to Operation Ready Fusion Reactor Conditions

Tampere 2013

Jean-Baptiste Izard

Development of Remote Handling Technologies Tolerant to Operation Ready Fusion Reactor Conditions

Thesis for the degree of Doctor of Science in Technology to be presented with due permission for public examination and criticism in Konetalo Building, Auditorium K1703, at Tampere University of Technology, on the 14th of June 2013, at 12 noon.

ABSTRACT

The International Thermonuclear Experimental Reactor (ITER) will be the next step towards fusion power plants, featuring deuterium-tritium plasma to generate 500 MW of fusion power. Using tritium will result in the activation of the vacuum vessel materials, requiring robotic manipulators to carry out the maintenance of the machine.

One of these robots must perform inspection tasks, such as carrying the ITER In-Vessel Viewing System (IVVS), and will need to be deployed in conditions as close as possible to the operating machine; the vacuum inside the vessel should be kept clean, the wall temperature and radiation level will be high, and the toroidal magnetic field should still be on. The robot should be able to place the probe within view of a good percentage of the plasma-facing wall covering the whole vacuum vessel.

This study aims to provide technical solutions for every system of a robotic manipulator in this environment. The effects of the magnetic field on the different systems of a robot will be investigated,[*] from the fundamentals of theory to practical experimentation, using a specially designed magnetic field generator. Solutions for actuation, sensing, logic system, and command that are tolerant of the magnetic field or actively use it to enhance the performance of the robotic manipulator are provided.[†]

A preliminary design of a robot using the technical solutions developed in this thesis as per the specifications of the IVVS is presented. The design is meant to demonstrate the feasibility of a robotic manipulator featuring multiple degrees of freedom within the constraints considered. Guidelines for geometry, actuation, sensing and logic systems design are provided that should allow the robotic manipulator to place its probe for it to view more than 99% of the first wall.

Finally, a summary of the major contributions of the thesis is given in conclusion. The major effects of a magnetic field on robot components are listed with guidelines on how to cope with them in the design. This chapter also sums up the different technologies, their advantages, and their limitations.

---

[*] Review of Design Principles for ITER VV Remote Inspection in Magnetic Field, J.-B. Izard, Y. Perrot, J.-P. Friconneau, Fusion Engineering and Design, Vol. 84, Part A, pp.969–973, 2009.

[†] Hardening Inspection Devices to Ultra-High Vacuum, Temperature and High Magnetic Field, J.-B. Izard, L. Gargiulo, D. Keller, Y. Perrot, 21st Int'l Conf. on Magnet Tech. (MT-21), 2009.

PREFACE

This work was executed through the PREFIT program (Preparing Remote handling Engineers For ITER), which resulted in the association of the CEA-LIST Interactive Robotics Unit in France, Oxford Technologies Ltd. in the United Kingdom, and VTT (Technological Research Centre of Finland) and the Institute of Hydraulics and Automation of the Tampere University of Technology in Finland. PREFIT is one of the European Fusion Training Schemes; it has been funded by Euratom as part of the Framework Programme n°6 for Research and Development.

Aside from the academic work that is the subject of this thesis, the PREFIT program is a permanent feature in the training programs at each of the associated partners' sites, includes an internship at each of the partners' premises, and a common school in each partner country to share specific knowledge. I would first like to express my deepest gratitude to those who made such a complex but definitely enriching program possible, namely Alan Rolfe at Oxford Technologies Ltd., Jouni Mattila at TUT, Arto Timperi and Mikko Siuko at VTT and Jean-Pierre Friconneau and Olivier David at CEA-LIST.

For the help, warm welcome and friendship they gave me during my periods out of France, I would like to thank Harri Kuusela and Boris Krassi from VTT, and Richard Meek, Edward Robbins and Paul Murcutt from Oxford Technologies Ltd. My special thanks are addressed to Arto Timperi, formerly at VTT, who took great care of me during my stay in Finland, and gave me a lot of his time despite his responsibilities.

I would also like to thank Jean-Pierre Martins, now working for ITER, for his support and teaching that aroused my interest in hardened robotics; Yvan Measson, from CEA-LIST, for his first-class advice on the big picture surrounding ITER and for his help in finalising the manuscript; Patrick Hertout, from the CEA Cryomagnetism Laboratory at Cadarache, for agreeing to spend time answering the many, and probably often silly, questions on electromagnetism and its effects in the real world from an uprooted mechanical engineer. Finally, I would like to address a special thank you to my supervisor Yann Perrot for his help, patience and faith in my capabilities.

On a more personal note, I express my gratitude to everyone I met at the CEA-LIST Fontenay-aux-Roses laboratories, be they permanent or temporary workers, apprentices, doctors or trainees, as each of them somehow participate in the greatly studious, leading-edge but also truly friendly atmosphere on site. A special thank you to the PREFIT researchers, Karoliina Salminen, Gregory Dubus, Teemu Kekalainen, Ryan King, and Robin Shuff, for the great memories we have shared during these last few years; and another one to my office mates Jonathan and Ziad for their constantly new tricks and surprises over the three years – and hoping that my own did not greatly disturb their work too much either.

Finally, I would like to direct a great and massive thank you to my family, my friends, and my dearest Marie for their love, friendship and support.

Paris, Feb. 4th 2010.

TABLE OF CONTENTS

TABLE OF ILLUSTRATIONS

TERMS AND DEFINITIONS

AIA	Articulated Inspection Arm.
AISI 316	General application austenitic stainless steel (18Cr-12Ni-Mo). 316L indicates a variant with lower carbon content to provide better weldability.
Activation	Nuclear process that consists in making an atom radioactive through the absorption of a neutron.
CEA-LIST	Commissariat à l'Energie Atomique, the French research institute on technologies regarding nuclear energy. CEA-LIST (Laboratoire d'Integration des Systèmes et des Technologies) within the Technological Research Department deals with technical development of embedded systems, interactive systems, sensors and signal processing.
CERN	Conseil Européen pour la Recherche Nucléaire, the main European research organisation on nuclear physics, hosting a series of particle accelerators, among which the LHC.
Contamination	Process in which tritium sets into porosities on part surface.
CSA	Canadian Space Agency
Diagnostics	Sensors and associated moving systems embedded in the tokamak's wall for plasma sensing.
Divertor	Lower region of the tokamak composed of 56 individual cassettes that carry the plasma facing components.
D-T campaign	Operation of a tokamak using deuterium-tritium nuclear fusion reaction. It is much faster than the classical deuterium-deuterium reaction but is also more harmful, as it generates high-energy neutrons that activate the environment and uses tritium, which is contaminating.
ENEA	Italian national agency for new technologies, energy, and sustainable economic development.
ERA	European Robotic Arm
ESA	European Space Agency
FEMM	Finite Elements Method Magnetics, an open-source finite element simulation program for electromagnetics.
JET	The Joint European Torus has been operating since 1997 in Culham, United Kingdom. It focuses on operation of high

energy plasma, achieving the record fusion power produced on Earth of 26 MW for a few seconds.

IRFM   Institut de Recherche sur la Fusion Magnétique, part of the CEA, running the Tore Supra experiment.

ISS   International Space Station

ITER   The International Thermonuclear Experimental Reactor (*iter*, the way in latin), the to-be largest tokamak in the world, is the next step towards fusion power plants, built through international cooperation. Research in ITER will focus on plasma research to ensure long stable fusion-capable plasmas, a major issue for future economically-sustainable fusion energy.

IVVS   In-Vessel Viewing System, used for viewing and metrology inside the torus, which is critical for erosion measurement. The available prototype is a 22 kg probe that uses laser range finding for metrology and reflected light measurement for image reconstruction.

LHC   Large Hadron Collider, located at CERN in Lausanne, Switzerland, a 27 km long particle accelerator whose accelerating line is made with 8 T superconducting magnets. It features large experimentation chambers named ATLAS, CMS, ALICE, and LHCb.

MRI   Magnetic Resonance Imaging, a medical imaging method based on the resonance of atoms in a high magnetic field. Current machines use 3 T magnets. This value is expected to reach 11 T with further superconductor developments.

PAC   Porteur Articulé en Cellule (in-cell articulated carrier).

PFC   Plasma Facing Component, some of the most solicited components in a Tokamak, as it has to evacuate the heat generated by plasma, up to 10 MW/m² in ITER.

Quench   Failure of the superconducting coils when they pass from a superconducting to a non-superconducting state, usually followed by a fast decrease in the current (and therefore the magnetic field) to prevent the coils from overheating.

Remote Handling   Generic expression for the specific work organisation, tools, and equipment around the teleoperated inspection of maintenance devices.

SCK-CEN	Centre d'Etude sur l'Energie Nucléaire (research centre on nuclear energy), based in Mol, Belgium.
Ti-6-4	Common high strength titanium alloy.
Tokamak	Plasma machine layout, widely used today for fusion experiment machines. It is the first design that uses magnetism for plasma confinement inside a torus-shaped vacuum vessel.
Tore Supra	Operating in Cadarache, France, under operation by CEA, this tokamak specialized in long-time plasmas uses superconductive coils for generating the toroidal magnetic field. It holds the record of the longest plasma achieved in a tokamak, lasting close to 3 minutes in a row.
UHV	Ultra-High Vacuum

LIST OF SYMBOLS

ε_0 Electric permittivity of vacuum.

μ_0 Magnetic permeability of vacuum ($4\pi \times 10^{-7}$ SI).

χ_m Magnetic susceptibility of a para- or diamagnetic material. Material property.

$\mathbf{B}$ Magnetic field flux density (T).

$\mathbf{div}$ Divergence operator.

$\mathbf{grad}$ Gradient operator.

$\mathbf{H}$ Magnetic field strength (A/m).

$\mathbf{rot}$ Rotational operator.

$\mathbf{Q}$ Energy confinement ratio of a tokamak. Q=1 means that the energy produced by fusion reactions is equal to the amount of energy introduced in the plasma.

1. INTRODUCTION

1.1. ITER Presentation

ITER 0, the next generation fusion experimental reactor that will be operational in 2020, is a massive step forward in the development of fusion as a source of energy. The main operative objective is to prove the possibility of stabilising a plasma that is hot and large enough to reach and overcome the 'Q=5' point for 8 consecutive minutes, at which the energy produced by the fusion reaction exceeds by five times the amount of energy that is fed to the plasma. This Q=5 point is generally assumed to be required in order to prove the possibility of running a stable plasma producing fusion, while a viable power plant should reach as high as Q=10. Therefore, ITER will show that it is possible to actually produce energy on Earth based on hydrogen fusion reaction, even if the commercial demonstration is yet to be proven.

In terms of physics, a large and stable plasma at high temperatures implies extremely precise plasma confinement, massive heating systems (and of course the auxiliary systems that have to be sized in respect) and operation using deuterium and tritium. The fusion power rating of the installation should reach 500 MW at full power. Previous records in tokamak are currently and have been held by Joint European Torus (JET) since 1997, with a 16 MW power pulse lasting 2 s as the most powerful fusion pulse achieved (at this point, the confinement ratio was measured at Q=0.8). On the other hand, the longest plasma pulse record in a tokamak is held by Tore Supra with its 390 s long pulse in 2003, which did not produce fusion power. Therefore, ITER is a huge step forward from current tokamaks. Yet technological challenges still remain to be overcome for the machine to operate.

One of these challenges is the accessibility of the machine, which greatly influences the machine's availability for research. As previously mentioned, in order to generate 500 MW of fusion power, ITER will have to use deuterium-tritium plasmas extensively. The consequence is that the vacuum vessel will be contaminated, and its first wall components activated by neutrons, which means that human access inside the vacuum vessel will be prohibited, even during planned maintenance shutdowns. In response to this problem, the ITER Organisation has set up a Remote Handling scheme pictured in Fig. 1-1 for maintenance, inspection and intervention in the vacuum vessel [14]. This scheme includes several robotic manipulators for each task.

1.2.   Remote Handling in ITER

Maintenance operations consist in retrieving consumable parts from the vessel, mainly the Plasma Facing Components (PFC), and taking them out of the vacuum vessel to be refurbished and then replaced by new ones [37]. There is therefore a need for extraction systems (Blanket Handling, Divertor Cassette Movers, which already have their test platform in operation [17][40]) and specific Remote Handling system for critical components just outside of the vacuum vessel (Neutral Beam Injector). An In-Vessel Multi-Purpose Deployer is also planned to be used for installing and retrieving smaller components from the first wall, for example diagnostic systems to be repaired at the Hot Cell.

These systems cannot be housed permanently in the ports of the vacuum vessel. A Transfer Cask System has been designed for carrying in and out the different Remote Handling System and the components to be replaced and transport them in the Hot Cells, where the fine operations for dismantling and installing PFCs, cleaning modules and testing the systems are carried out using master-slave arms controlled by a human worker at the Control Room.

In addition to these systems, an inspection device, the In-Vessel Viewing System (IVVS), is planned to be installed permanently within the first wall for carrying out regular inspections of the first wall.
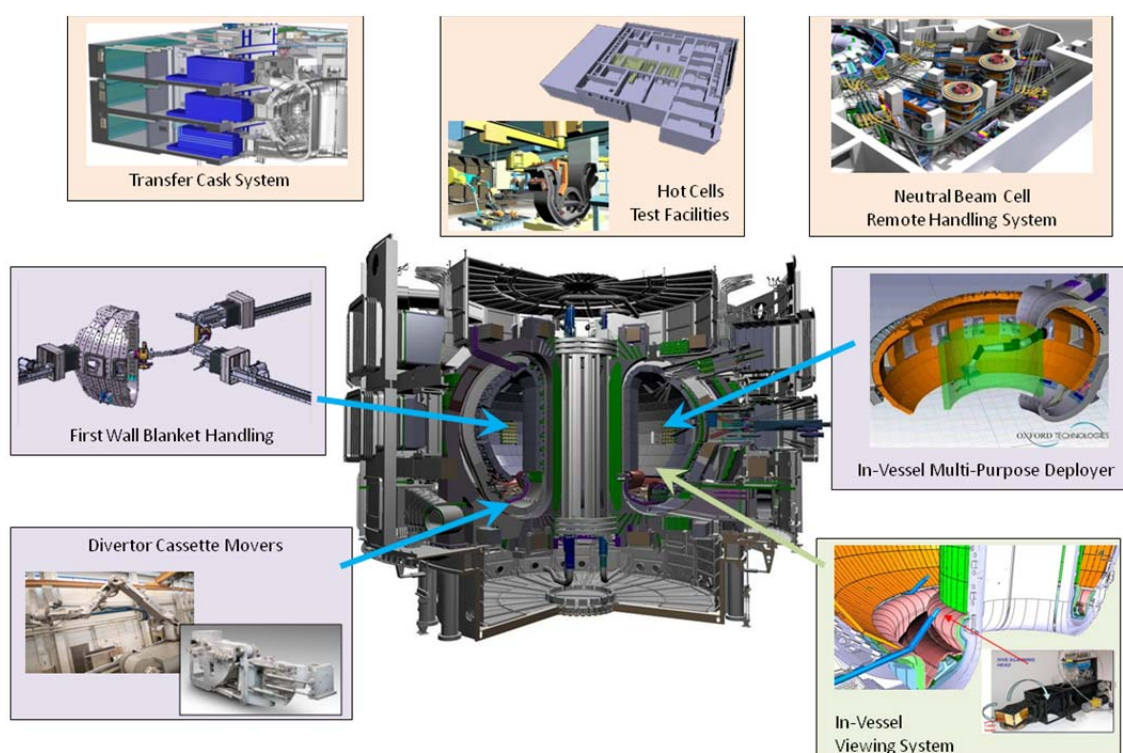
Fig. 1-1: Remote Handling Systems in and around the ITER Tokamak.
Maintenance systems are pictured on blue background, while inspection systems are pictured on green background. Red background systems do not operate inside the vacuum vessel.

Each of these systems (Fig. 1-1) is a different system, provided by different teams and different kinds of funding: Blanket Handling system is in-kind procurement by Japan, Divertor Handling, Neural Beam, Transfer Cask system and IVVS are in-kind procurement from Europe, while the other systems are paid by ITER Organization through direct funding. Depending on their use, they have been classified as maintenance or inspection devices as indicated above. There is indeed a distinction that matches very different environmental constraints summed up in Table 1-1.

	SCHEDULED INSPECTION	UNSCHEDULED INSPECTION	MACHINE MAINTENANCE
Postulated operational Scenario	1 day after plasma operations	1 hour after plasma operations	2 weeks after plasma operations
Atmosphere	UHV conditions (>10-5 Pa)		Dry air (approx 1 bar)
Temperature	Normal case <120 ˚C Off-normale case <240 ˚C		<50˚C
Magnetic field (deployed)	5 – 8 Tesla		Approx. zero
Magnetic field (stored)	0.3 Tesla		Approx. zero
Radiation * (dose rate) (deployed)	1,500 Gy/h	15,000 Gy/h	300 Gy/h
Radiation * (accumulated dose) (stored)	Total Neutron Fluence (Basic Perfomance Phase BPP) est. 5.07 E13 n/cm2 Gamma dose (BPP) est. 1.41 E+02 Gy Additional radiation from divertor cooling water ^{16}N (TBD)		
Assumed inspection duration *	12 h/week, twice monthly, over 7.5 years	12 h/week, twice monthly, over 7.5 years	60 h/month over 32 months
Total dose gamma Total dose neutron	2.7 MGy 5.07 E13 n/cm2	27 MGy 5.07 E13 n/cm2	0.6 MGy 5.07 E13 n/cm2

*estimated data

Table 1-1: Inspection and maintenance environmental conditions in ITER [58].

1.2.1. Maintenance operations

PFC tiles are fixed on modules, whose weight range from 1 tonne to 10 tonne for divertor cassettes. Therefore, maintenance of PFCs includes heavy manipulations at low velocity to extract the modules out of the vacuum vessel and transport them to the hot cells for refurbishment. These operations are incredibly time consuming. In the current design, the complete replacement of the 54 divertor modules in the lower region of the vacuum vessel will take 179 days [14], and the complete replacement of the blankets (the 440 modules carrying the PFC plugged on the vacuum vessel first wall) will take 276 days [14]. For these massive maintenance operations, waiting a few weeks after plasma shut down to introduce the robotic manipulator is justified to allow the temperature and radiation levels to decrease. These maintenance operations are also carried out at atmospheric pressure. The radiation level is still far too high for a human to enter the reactor (the legal dose for a nuclear worker is reached in just a few seconds under these conditions) and requires a lot of hardening research and development work for the maintenance robotic manipulators.

1.2.2.   Inspection operations: description of the IVVS

Inspection has different design requirements compared to maintenance robotic manipulators. Inspection tasks are usually less complex tasks that are carried out between two plasma shots, typically to detect a potential defect or to visually inspect the tokamak to ensure that the next plasma operation will be safe. The current ITER baseline predicts the use of a viewing system, the In-Vessel Viewing System (IVVS) [14], carried by a basic deploying rod (Fig. 1-2). The goal of the IVVS is to provide a view of the inside of the vacuum vessel and to provide a 3D point cloud map of the first wall in order to evaluate erosion of the PFC tiles with precision down to the millimetre. This metrology data will be used as well for estimating the mass of tritium present in the dust within the machine, which is a regulation requirement for installations using tritium. A prototype probe for the IVVS has been developed by ENEA [31][59] using laser-based accurate distance measurement. This probe weights 22 kg and uses light emitted by a laser placed outside of the vacuum vessel. The ray of light is deflected by a prism which orientation is set by two ultrasonic motors guided by optical encoders. The probe is capable of carrying out metrology measurement with 0.5 mm accuracy every millimetre, with stay time per pixel of 20 µs. Considering the surface of first wall to be measured by each probe, the time required for measuring the whole first wall is estimated to be less than one hour.
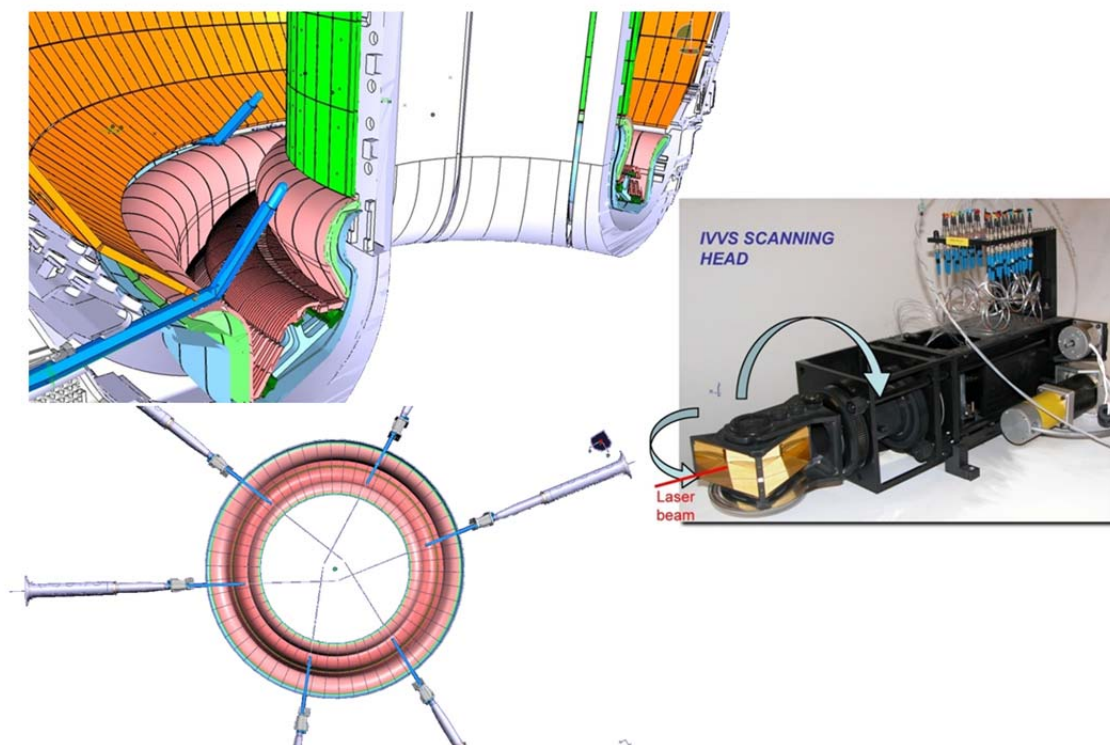
Fig. 1-2: IVVS specifications as per the current ITER baseline.
Left: Schematics on IVVS deployment, with the IVVS deployed in the vacuum vessel.
Right: View of the probe prototype for IVVS developed by ENEA.

In the current ITER baseline, deployment of the IVVS is carried out autonomously by a two degrees of freedom deployer with the probe at its end. The degrees of freedom are insertion (linear joint) and segment elevation (pivot joint). There are 6 IVVS systems in the tokamak, which altogether give an almost complete view of the first wall.

1.3. Scope of work

Considering the shape of the first wall section and particularly the shape of the divertor, it is impossible with this configuration to have a complete view of the vacuum vessel by making a measurement at only the 6 positions specified for the IVVS, since part of the divertor is not in the line of sight of the probes. In addition, the actual design of the probe has inherent limitations: the probe is unable to make a measurement as per the requirements on surfaces showing a beam incidence angle of more than 70 deg [59]. The result of this is that even more of the first wall surface cannot be viewed using this probe, particularly on the edges of the divertor, to an extent that has not been evaluated yet.

This fact is actually impairing for tritium dust inventory since the outer edges of the divertor illustrated in Fig. 1-2, are where dust and flakes due to erosion of PFC tiles are gathered – and this is where a major part of the tritium will be. The situation is mainly due to the design of the deployer rod. The design had to be very simple due to very demanding environmental conditions. Moreover, the design at the time did not take into account that the IVVS could be used for tritium dust inventory as well.

In order for the IVVS to be able to view the whole first wall surface, another deployment strategy should be chosen, using a robotic manipulator with multiple degrees of freedom, allowing a good dexterity in a large workspace. The workspace is considered large in comparison to the insertion section, which measures only 150 by 140 mm, while the reach of the robot is between 5 and 6 meters with the current deployment baseline. As a comparison, it may be noted that standard industrial robots in the 30 kg capacity range provide a reach of a couple meters for a section in excess of 300 mm in diameter. On the other hand, dexterity describes the fact that the robotic manipulator must feature enough degrees of freedom to allow adapting the configuration of the robot to the task to be accomplished, as opposed to the deployer rod of the IVVS in the current state of design, which is made for placing the probe in a single position because of a limited number of joints in the kinematics.

But in order to be able to design such a robot for the ITER inspection environment, it is necessary to understand which robotic components are operational or how they may be modified to operate in ITER inspection conditions. In addition, the development of the Articulated Inspection Arm (AIA) for Tore Supra inspection tasks has proven to be of great interest to physicists and operations engineers. The tasks identified for this in-vessel long-reach inspection robotic manipulator with many degrees of freedom (nine in the case of the AIA) are low impact interventions such as leak sniffing, for example, in cooling and vacuum circuits, dust removal, laser ablation or diagnostics calibration.

These intervention tasks must have a minimal effect on plasma scheduling; they should be done in a minimal time in environmental conditions that are as close to the operational environment of the machine as possible. The interest in this design for Tore Supra proves that such a highly dextrous inspection robotic manipulator would be valuable for ITER operation, despite the environmental constraint, with a good availability which the Multi-Purpose Deployer does not offer since it operates in maintenance conditions.

An inspection robotic manipulator should be able to reach and inspect various parts spread around vacuum vessel parts while carrying tools for different intervention tasks, not limited to the IVVS probe. This requirement implies that this robotic manipulator should be a highly dextrous long-reach robotic manipulator with multiple degrees of freedom. Such a feature sets it apart from ITER diagnostic moving systems (most of which being two-position shutters) that are permanently installed close to the first wall and feature minimal movements. Therefore, the design of intervention and inspection robotic systems should be completely different from what already exists in ITER, which means that the problems related to their design must be addressed.

1.4.   Thesis goal and plan

The goal of this thesis is to address the extreme design constraints that will be faced by ITER dexterous long-reach inspection robotic manipulators. The thesis will address the multi-objective design constraints that the ITER environment sets on inspection robot design. The ITER environment is extreme and unique as it unites design constraints that have never before been faced together, in particular the high magnetic field that very few robots have had to tolerate. The state of the art chapter of this thesis reviews numerous techniques used to cope with design constraints similar to those for ITER. Thereafter, the thesis focuses on the identified design knowledge that have been developed in thesis for designing a dextrous robotic manipulator for ITER inspection. A novel design method for robot actuation and sensing components is proposed. These components use the ITER magnetic field to improve the performance of the robotic manipulator. Among other developments, as an example, a solution using the actuation principle of a DC-motor is proposed that dramatically reduces the typical weight to power ratio of the technology and thus enables robot performance improvements. Design of proposed magnet-less DC-motor is presented and prototype actuator is build. This prototype DC-motor actuator design is verified in 1.0 Tesla magnetic field generator testbed designed and constructed in this thesis. Based on an off-the shelf DC-motor, the proofed design is shown to provide an equal power for a weight improved by 50% and a reduced velocity output. Finally, a novel conceptual inspection robotic manipulator for ITER wall inspection carrying a 22 kg IVVS viewing probe is designed using the developments presented in the thesis, and the inspection robotic manipulator first wall viewing performance is assessed by a simulation program.

The study is structured as follows:

First, the technical design issues due to ITER environment and the requirement for the long-reach and dexterity of the ITER inspection robotic maniplulators are defined and then compared to existing state of the art systems. The state of the art chapter reviews existing hardening design technologies for high temperatures, Ultra-High Vacuum (UHV), and radiation. The main design focus rests on the unaddressed issues, mainly the presence of the high magnetic field.

Once the state of the art is reviewed, the focus of the present thesis is specified in more detail. Considering the novelty of the high magnetic field design constraint on robots, this topic will be the main thesis objective for designing an array of component technologies for the structure, sensing, actuation and data processing. The hardening to temperature, UHV and radiation will be a secondary objective, using the principles that have been developed previously in robotics. In chapter 2, current state of the art review is followed by presentation of basic equations of classical electromagnetics relevant for understanding the application of these equations to different robot component materials and concepts developed in this thesis. In more detail, the focus of section 2.5 Magnetism concepts and effects is on the basic theories that are necessary for understanding theoretical basics and for estimating the effects of a high magnetic field on different types of robot components. In particular, three magnetic field effects that affect robot design are introduced : induced voltages, eddy current drag in conducting materials, and magnetisation forces due to the magnetic susceptibility of the materials.

Based on these equations, chapter 3 reviews robotics technologies with respect to ITER inspection environment requirements. A set of material choices and technologies are presented and discussed with respect to the functionalities required in a robotic manipulator. In the structural design, this chapter discusses different materials considering the magnetisation force they will face in ITER, and proposes a solution for increasing the natural damping of a long-reach robotic manipulator. For robot actuation, a novel conceptual design of a magnet-less DC brushed motor for actuation under high magnetic field is proposed. In addressing data processing, a comparison of wiring techniques and data transfer systems with regard to the effect of the magnetic field is considered. Finally, in order to determine the position of the robotic manipulator in the vacuum vessel, chapter 3 presents a solution using the local measurement of the magnetic field and comparing it to its mapping, leading to accurate absolute positioning that can be useful for ITER metrology operations. In order to validate the operation of some of these developed technologies, a magnetic field generator for verifying the designed magnet-less motor performance is designed.

Some of these technologies required proper testing in high magnetic field conditions. The verification tests and the results for proposed and designed magnet-less DC-motor prototype in the 1.0 Tesla magnetic field is presented in chapter 4. In particular, the magnet-less motor proved to operate as planned at the same power rating as the original motor from which it was taken, for a weight reduced by the weight of the magnet, that is 50% of the motor weight. Tests have been carried out on transistors as

well, showing no effect during operation. Finally, a new conceptual ITER inspection robotic manipulator design is proposed. It is built in 3 actuated segments with 6 DOFs, for a reach of 5 m, weighting in total 140 kg for a probe weight of 22 kg. This novel conceptual robotic manipulator design proposal is based on the developed technologies with a design verified with respect to the forces due to the ITER high magnetic field and is tested with a simulation program for reachability and dexterity for IVVS ITER first wall inspection task. This new ITER inspection robotic manipulator concept allows almost full coverage of the first wall (99%) using a probe based on the principle and design of the IVVS prototype.

Finally, the last chapter of this thesis presents a summary of the principal advantages and disadvantages of the different technologies developed in this thesis. The other fields of application for these new developments are also suggested, including of course inspection robotics for tokamaks but also for the first wall diagnostics for fusion or particle accelerators. A list of the contributions of the thesis is also given.

1.5.   Thesis contributions to the state of art

The effects of a high magnetic field have been detailed on the different components for building a robot: the structure, the actuators, the sensors and the data processing hardware. Structure effects deal with loads on inert structure due to the material properties in the magnetic field. Actuation has some difficulties in the presence of high magnetic field: a series of solutions are presented, based on water hydraulics and DC motors – a mock-up of the latter solution, using the local magnetic field, is verified in a magnetic field generator specially designed and build for this thesis objectives. Sensors are sensitive equipment; the operation of various types of sensors has been assessed, and innovative solutions using the magnetic field for measuring the position of the robotic manipulator is presented. Data processing with copper line wiring is difficult due to the effects of induction and the behaviour of the electronic hardware. These behaviours are estimated and measured through testing, and solutions for limiting the effects of induction are developed. In addition, the possibility of using fibre optics is discussed.

The solutions developed in this thesis have been designed by focusing on the effects of the high magnetic field. However, the other design constraints of the ITER inspection environment have been taken into account as well, and all of the presented solutions can be utilized through appropriate design. Design rules for dealing with UHV, temperature and high level of radiation are presented in the state of art section. Therefore, it has been proven that it is possible to match the requirements of the combined constraints from temperature, UHV, radiation and magnetic field for every element of a robotic manipulator. Moreover, among the solutions, a couple of them turn the magnetic field design constraint over to enhance the design, providing improved performance compared to what can be achieved in a magnetic field free environment.

This thesis also reveals which technologies can be used in the ITER inspection environment to build a complete long-reach dextrous inspection robotic manipulator that is temperature, UHV, radiation and magnetic hardened for the deployment of an IVVS probe and for other ITER inspection task requirements. With additional hardening to radiation, these technologies can also be used for actuation, sensing and data processing on advanced first wall diagnostics devices.

In order to verify developed technologies, a preliminary inspection robotic manipulator conceptual model has been designed. This novel long-reach dextreous ITER inspection robotic manipulator concept is based on state-of-the-art robot architecture for long-reach dextrous manipulation can carry a 22 kg IVVS probe or tool, for a total weight of 140 kg. It is built with 3 individual segments featuring 6 DOFs, reaching 5 m in length. According to the simulation results mainly targeted for proposed inspection robotic manipulator reach and, on the other hand, workspace and dexterity studies with respect to IVVS task presented in this thesis, this robotic manipulator ensures more than 99% coverage of the ITER vacuum vessel first wall with the current IVVS prototype probe. The regions that are out of sight are between the blankets and the divertor – these regions are impossible to inspect with the current probe due to the configuration of the first wall and the IVVS probe limitations - and the last few millimetres of the divertor's edges, due to positioning errors that have been calculated on simulation.

1.5.1. Structure: magnetic forces

Two effects have been proven to generate forces on a robot structure. The first one generates a volume force linked to the magnetisation of the material, directed towards the centre of the torus in the case of ITER. Magnetisation force is always present. Section 3.2.1 details the values for these forces in unit of kgf/kg for different materials commonly used in robot designs. Magnetisation force values range from 50 kgf/kg for Cobalt Iron to 0.02 kgf/kg for Ti-6-4 Titanium alloy. Paramagnetic materials in fact do not have zero magnetisation force and should be compared with their magnetic susceptibility values. For example, AISI 316L stainless steel, coined as paramagnetic material, suffers a magnetisation force that is up to 2.1 kgf/kg.

The second effect under consideration generates a drag on rotational movement due to eddy current generated into the parts. Translation movement do not generate such drag with the configuration of the magnetic field in ITER. The drag value is directly linked to the conductivity of the materials used. Again, values of this drag are given for different materials in section 3.2.2. An innovative design guideline is presented, using cautiously designed conductive parts in key places to generate drag to a level that allows damping the natural vibrations of a long-reach inspection robotic manipulator.

1.5.2. Actuation

Two cases have been separated for actuation, depending on the power required. For low power joints, typically below 10W, hypersonic piezomotors are available on the market. These amagnetic and radiation tolerant motors run at low velocities and lead to accurate positioning, providing a correct control board is brought inside the robot.

For higher power above 10W, other kinds of actuators should be used. Such actuators can be found using water hydraulics, provided that a series of ITER design constraints are respected that include fluid cooling down to 50°C to avoid cavitation, using jacks only, with the hydraulic valves outside of the magnetic field, and using specially designed elements – or dealing with the high forces generated by magnetic field on the water hydraulic components made out of AISI 316L stainless steel material.

DC brushed electric motors seems to be a promising high power actuation solution for inspection robotic manipulators. A standard brushed DC motor can operate both with and without the magnetic field, provided two constraints are respected: the motor does not move or is displaced in a radial section of the torus, and its magnet poles are oriented parallel to the ITER local field. However, the motor will, operate at different velocities for a given input voltage when the ITER field is on or off. Such a motor will also suffer from high magnetisation forces arising from its saturated core when in the ITER field.

An attractive design alternative when the robotic manipulator should operate only when the field is on is to use a magnet-less motor, using the ITER local field for motor operation. This type of motor without stator magnets can use standard coreless rotor and brushes for a lower velocities and higher torques than its original construction is specified to. Magnet-less motor without stator magnets means that the weight of the motor is reduced by more than 50%. With a higher operating voltage, the power rating of the original motor can even be further increased, providing the motor elements can withstand it electro-mechanically. The nominal output torque and other motor parameters are local field position-dependant, therefore advanced control solutions and local magnetic field sensing should be provided. Such a concept has been proved to work in the magnetic field generator designed in this thesis, up to a field of 1.0 T, through the change of the torque constant (linking on the one hand current and torque and on the other hand voltage and rotor velocity) in function of the value and direction of the local magnetic field.

Once the electric motors are sized and selected for joint actuation, reduction gears are almost always necessary. The gear first stages have usually high rotational velocities that may generate high eddy current drags. Therefore, section 3.3.3 presents and makes a comparison on spur and planetary gears for different reduction ratios.

1.5.3. Sensing

For position sensing, the typical solution tolerant to high magnetic field uses a slotted wheel with a deported light source and sensor. This optical encoder principle is the most

secure solution for position sensing, and is used for previous high magnetic field position sensor designs such as for the IVVS pan and tilt motions.

A coreless resolver can be built with a special design and special data processing to provide both a position and a local magnetic field measurement on high velocity shafts.

Absolute velocity measurement can be achieved through measuring the voltage of a coil placed in the robotic manipulator. It requires a good knowledge of the local value of the magnetic field to achieve this. In addition, through using the magnetic field map of ITER and very precise magnetic sensors, it is possible to retrieve the absolute position of the robotic manipulator. Both of these measurements can only be done when the field is on.

1.5.4. Data processing

Radiation tolerance is actually the most constraining design requirement when it comes to electronics, as the ITER magnetic fields intensity is not high enough to perturb electronic component operation with the exception of iron core coils and transformers. Experiments carried out in this thesis have proved that transistors were not disturbed by the presence of a magnetic field up to $1.0\,\mathrm{T}$. State of the art solutions in radiation tolerant electronics has given promising results with the very simple and rugged designs, up to the complexity of a signal multiplexer circuit.

Induction in the sensor and power wiring can be dealt with by avoiding loops in the design of the electric circuits and twisting systematically inputs and outputs together. In case loops cannot be avoided on some boards, it is important to make sure they are on the horizontal plane when the robotic manipulator is parked, as quenches (fast shutoff of the magnetic field) may occur in this situation.

Optical circuits are a powerful way to avoid induction. An exception subsists when using polarized light, in which input and output fibres should be twisted together in the same way than input and output of a copper wires. Of course, radiation tolerant fibres should be used in this situation.

2. REVIEW OF HARDENED TECHNOLOGIES AND ELECTROMAGNETICS CONCEPTS

This chapter reviews the state of the art in hardening technology solutions that meet the ITER inspection environment requirements. Special attention is given to robotic solutions with long-reach and dexterity on the one hand, and tolerance to high magnetic fields on the other.

The environmental conditions in ITER are not yet matched by an inspection robotic manipulator design that has sufficient number of degrees of freedom to match the dexterity required for the complete inspection of the first wall and required long-reach capability. A first focus is therefore set on smaller systems that are capable of operating in the ITER inspection environment in order to review already proven design principles and solutions that could be potentially applied in an inspection robotic manipulator. In this category, developed fusion reactor diagnostics devices are discussed, as well as the In-Vessel Viewing System (IVVS) design proposal by ENEA for ITER. Diagnostics used in other large scientific machines that use magnetic fields higher than 1 T, such as the Large Hadron Collider (LHC) in CERN and other particle accelerators, are reviewed in this chapter. The radiation hardening campaigns for ITER diagnostics components are also reviewed.

In a second part, this chapter reviews literature of existing long-reach inspection robotic manipulator designs and components that are able to match some of the ITER environmental constraints. The aim is to select technical solutions that are already proven to be compatible with part of the ITER inspection environment conditions, and look into their architecture to choose the most fitted to IVVS probe deployment. The presented systems – namely; the Articulated Inspection Arm (AIA), Porteur Articulé en Cellule (PAC), and MASCOT Boom –provide a series of proven technical solutions that can be adapted for long-reach ITER inspection robotic manipulators. However, ITER unmatched environmental conditions require these solution to be adjusted to meet ITER inspection requirements.

Because robots that are able to operate in high magnetic fields are scarce, a description of the different solutions developed for manipulation inside medical Magnetic Resonance Imaging (MRI) devices will also be presented. These robots are able to carry out simple operations, such as placing seeds in a patient, with the feedback of the MRI with three degrees of freedom. This type of robots are called MRI compatible robots because they have been designed with materials and actuation

systems n that endure the high local magnetic field and that do not disturb the imaging system.

The section 2.4 sums up the different solutions encountered when analysing existing solutions. Based on this existing solutions review, knowledge gaps in the technical designs and developments needed for the enhanced conceptual design for long-reach dextrous ITER inspection are identified.

The novelty of the work resides in the magnetic field design constraint on robots which is the central topic of this thesis. In order to be able to review the effects of a magnetic field on the different elements of a robot, the section 2.5 on magnetism concepts and effects, will briefly present the theory of magnetostatics and detail the different phenomena that will result in perturbations or potential new applications for robots.

Section 2.6 presents the chapter conclusions.

2.1. Diagnostic systems

2.1.1. Tokamak diagnostics deployment

In addition to the UHV and temperature, fusion diagnostics systems have to withstand tremendous doses of gamma and neutron radiation and high temperatures as they are used during plasma operation itself. They also must cope with the eddy currents that are generated throughout their structure in the case of a quench in addition to the local field. Therefore, the environmental constraint on these systems is quite limiting.

For these reasons, fusion diagnostics are rugged and simple systems with limited degrees of freedom to avoid failure. Pneumatic actuation using inflated steel bellows that generate linear movement is extensively used. More complex and exotic systems such as temperature-actuated mechanisms and designs that use the local field to generate movement were also used in previous tokamaks [36][44]. This type of technology will likely be used in ITER in applications where the required motion range and force are large. In a diagnostics environment, most of the loading of the actuator is due to the eddy currents generated in the moving parts and in case of quenches, generating both intense heating and high forces.

2.1.2. Coil-based magnetic field probes

As is well known, a simple way to measure a magnetic field is to move a coil in this field and measure its voltage. This principle, in fact, allows quite accurate field measurements. Therefore, this principle is used in many magnet characterisation probes, such as the Mole for superconducting magnets presented in [41]. This probe allows the precise measurement of the ramping and alignment of different kinds of magnets. This performance is achieved by featuring a modular approach and actuated segments that perform the position feedback. Therefore, this device performs position feedback and actuation; position feedback is carried out by encoders and actuation by ultrasonic

rotary piezomotors. These components are not affected by the high magnetic field (up to 4 T). There is no electronic processing circuit in the probe.

2.1.3. ENEA design for the IVVS probe

The ITER IVVS is designed to take measurements and provide visual feedback of the inside of the ITER vacuum vessel for visual inspection tasks under inspection conditions. Fig. 2-1 shows the prototype [30][31][59] that was built by the Italian Fusion Association ENEA. The IVVS prototype operation is based on an optical laser that is directed towards the head of the probe using hardened optical fibres, and is then directed towards the target wall with a prism whose position is set by two actuated degrees of freedom. The most recent IVVS design weighs 22 kg. The probe is made of stainless steel (AISI 304) and actuated with ultrasonic motors and gears. The mirror frame is made of titanium alloy to reduce the eddy current drag, as its pan and tilt motion velocities are expected at 360 deg/s. The material used in the gears is also AISI 304 stainless steel coated with titanium nitride for lubrication. The radiation tolerance of the key components of the probe has been assessed in [50] at 50°C.

Fig. 2-1: ENEA proposal probe for the IVVS.

The maximum power required to drive the prism tilt axis at 360 deg/s has been estimated to be 25 W through finite element analysis.

Due to the position of the prism and the size of the frame holding the gearings and the motors, the mechanism has a blind cone behind its insertion axis of 20 deg.

In the current ITER baseline, the IVVS is deployed through 6 ports in the divertor: ports number 03, 05, 09, 11, 15 and 17, which means a port every 40 deg, then 80 deg, then 40 deg, etc. The entrance point of the robotic manipulator is where the divertor and the blanket regions join, on the outer wall, with a 6 deg slope.

With this design, the maximum incidence angle between the laser beam issued by the prism and the viewed surface is 70 deg [30], with performance on metrology lower than the ITER requirements (0.5 mm [58]) for higher incidence angles. The lowest viewing distance is 1 m on the current design [30], but a suggested design would have two focus areas, between 0.5 m and 2 m and between 2 m and 10 m and feature a high-energy laser for measuring accurately with incidence angles up to 80 deg[59].

2.1.4. LHC power electronics for in-field components

High-energy experimental particle physics accelerators, like the ones built by the world famous CERN, feature strong magnetic fields as high as 8 T. However, the volume flowed by the magnetic field is a long but small tube; quite different from the one in ITER, which is a torus, large respective to its height and diameter. For example, the LHC is 27 km long and features a magnetic field as high as 8 T, but the diameter of the volume within this field is only 30 mm in most sections. However, large volumes are swept by high magnetic fields in the so-called large sensor areas in which the field sweeps a cubic volume of several cubic meters. These areas feature particle detection sensors and the electronics driving them that must thus withstand the high field.

Experimental particle physics requires radiation and magnetic tolerant components and systems like those presented in the Topical Workshop on Electronics for Particle Physics, TWEPP [61]. In these accelerators, the magnetic field interferes with the DC-DC power converters used at the sensors areas, as they face a field of up to 4 T and radiation of up to 1 MGy. One design proposal for in-field operation is to replace the inductance coils with air-core coils [61]. No information is given on the in-field operation of other diagnostics components.

2.1.5. Electronics radiation hardening for ITER

Embedded electronics is a critical design problem when dealing with the radiation levels in ITER. The ITER design documentation includes a Radiation Hardness Manual [3], which contains a list of maximum radiation doses for a wide range of components that are foreseen to be used in the vacuum vessel. The listed components range from optical fibres and lubricants to actuators and video cameras. Although complex electronic systems such as multiplexing systems are not currently rated higher than 10 kGy, some single transistors are rated as high as 10 MGy. The design of some of the simplest electronic systems rated at 10 MGy of the total accumulated dose using these transistors are likely realistic. The Radiation Hardness Manual also features a few digital circuits (JK flip-flops and bit to bit invertors) using discrete transistors that withstand doses in the 10 MGy range, with the transistors chosen rated 10 MGy-hard. The European Fusion Development Agreement (EFDA) RADTOL final report [50] gives further explanations for electrical component failures at 10 MGy doses.

Among the several teams that have worked on the electronics hardening for ITER and EFDA, the Centre d'Etude sur l'Energie Nucléaire (SCK-CEN) teams [60] have

developed a range of radiation-hardened designs for ITER. SCK-CEN performed radiation hardness characterisation for a set of transistors [51]. Additionally, a higher level design of electronic systems was also carried out, with particular attention to radiation-hardened optical networks and transceivers [2][22][23]. Based on the impressive results achieved in these campaigns, it will be possible to build electronic designs that are compatible with the ITER inspection task requirements.

2.2. Dextrous long-reach robotic manipulators

2.2.1. Articulated Inspection Arm

The AIA[10][13][18] (Fig. 2-2), currently under development at CEA-LIST and IRFM laboratories, is an articulated long-reach robotic manipulator designed for in-vessel inspection. The AIA is designed to operate in the following conditions:

- Ultra-High Vacuum (10^{-5}Pa)
- High temperature (operating at 120°C, baking at parking at 200°C).
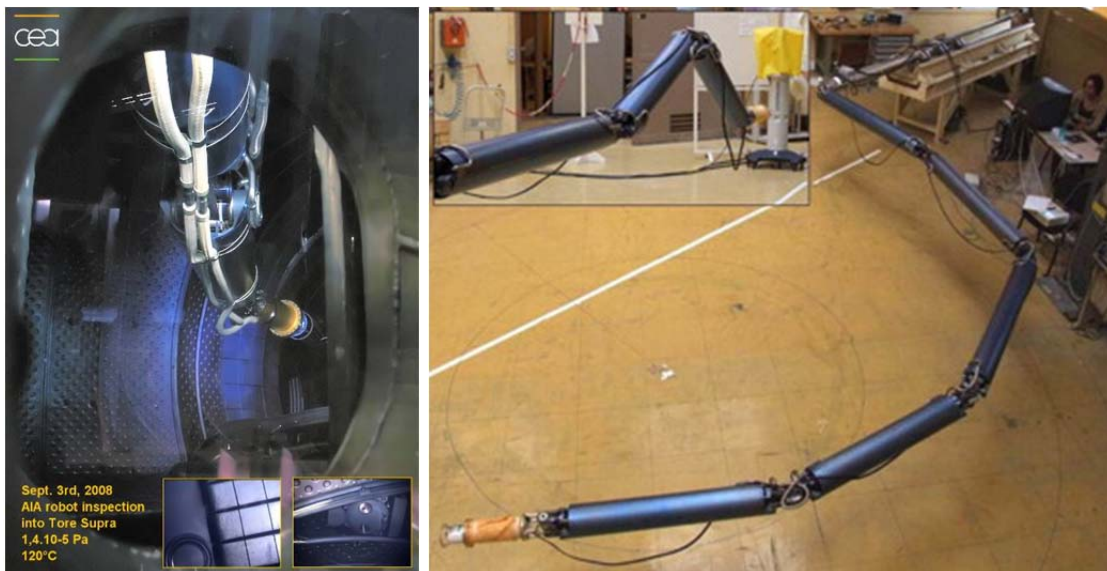
Fig. 2-2: Operational views of the AIA robotic manipulator.
Left: AIA robot and vision diagnostic deployment in Tore Supra under UHV and 120 degC.
Right: examples of deployment configurations during identification campaign [13], picturing yaw (main image) and pitch (miniature) degrees of freedom.

The AIA is a 5-segmented robotic manipulator with a load capacity of 10 kg and a total length of 7.4 m. Each segment has two degrees of freedom – yaw and pitch – featuring a parallelogram structure. In total, the robot has 9 degrees of freedom (pitch on segment 1 and 3 are fixed, and there is an additional yaw joint for the payload). The AIA requires a penetration hole of 250 mm diameter, its segmented body being 160 mm in diameter. The difference between the two is necessary to allow the electrical cables to run from one segment to the next. The total weight of the device is 130 kg.

The first introduction of the AIA in Tore Supra operating under UHV and temperature conditions occurred in September 2008. The robot carried a hardened viewing probe that allowed watching limiter tile erosion and the operation of diagnostic shutters. Plasma operations were resumed 15h after removing the robot – the time needed to power up the superconducting coils. A full range of end-effectors are now studied, ranging from laser detritiation to diagnostic calibration. Some contact tasks with gripping tools have been included among these tasks.

As mentioned, each AIA segment has a parallelogram structure, described in more detail in Appendix A. The parallelograms in segments 2, 4 and 5 are actuated in pitch by an electrical jack that is composed of a DC motor, a gearbox and a satellite roller screw. The pitch actuator is situated on the parallelogram diagonal. Segments that are not actuated in pitch are fitted with a fixed length rod on their diagonal.
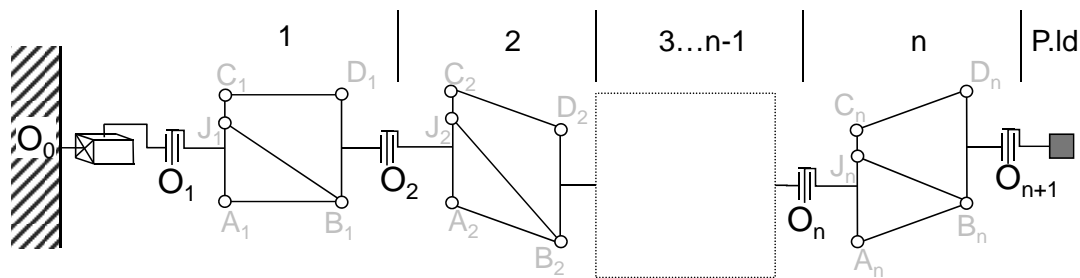
Fig. 2-3: Kinematics of the AIA long-reach robotic manipulator.

Between each parallelogram, a vertical pivot joint, which is called the yaw joint, separates the two segments. The pivot joint is operated with an electrical jack similar to the pitch actuator that is pulling a stainless steel cable attached to the pulley on the joint.
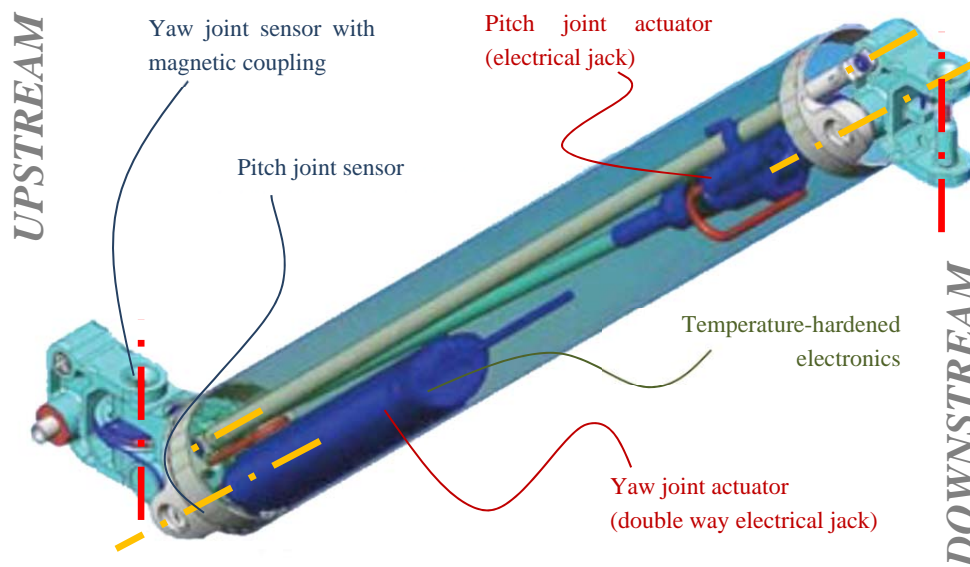
Fig. 2-4: Detailed design CAD view of an AIA segment.
Orange dotted lines show the joints materializing the parallelogram. Red dotted lines show the yaw axes. The yaw axis actuated by the segment yaw actuator is on the upstream side.

Elements shown in the kinematics scheme of Fig. 2-3 can be seen in Fig. 2-4, showing one of the segment: the top beam of the parallelogram, loaded in traction in normal cases, is the cylindrical small diameter beam running across the tube. The tube is actually the bottom beam of the parallelogram, loaded in compression. Segment own yaw joint is situated on the left of the picture, which is upstream. The downstream clevis of the previous segment is also shown. The vertical bars of the parallelogram are materialized by two clevis parts upstream and downstream.

The two blue boxes on Fig. 2-4 show the UHV leak-tight boxes made of stainless steel containing the actuators. The box on the diagonal houses the pitch actuator, and the box on the left houses the yaw actuator, a double-side electric jack pulling on a cable sneaking through the pitch joint to the yaw joint. This cable routing generates coupling between yaw and pitch axes of the segment, which is to be taken into account for control.

The leak-tight box containing the yaw actuator also contains the electronics of the segment (multiplexing system). Joint sensors on yaw and pitch joints are placed in individual leak-tight boxes close to the actual joint, using magnetic couplings for transmission of movement from the parts to the sensor.

This structure is interesting for long-reach robotic manipulators because the downstream torque is supported by the parallelogram and not by the actuator; the actuator must only withstand the torque developed by the downstream weight applied on the downstream pitch axis plus the weight of the module applied on its centre of gravity. Another advantage of the parallelogram mechanism is that the rotation axes are always in the horizontal plane. This configuration limits the torque required from the yaw actuator due to the absence of gravitational torques.

Additionally, the parallelogram structure allows the building of robots from modular segments, making it easy to develop robots with many degrees of freedom and high dexterity.

Sensor data information is transferred to the segments using signal multiplexing systems. Each segment is equipped with temperature-hardened NEUROBOT multiplexing electronics. The electronic systems also include an amplifier system for the DC-brushed motors. The NEUROBOT multiplexing system is a self-inspecting system, which ensures that errors in the data are not transferred from the base or other NEUROBOT cards of the chain.

DC motors and gearboxes are low power, (64 W) off-the-shelf motors and their standard attached gearboxes, both hardened to the required high temperature operation. With joint torques ranging from 0.1 to 1 kNm, the joint velocities are very low, a few tenths of a degree per second (0.1 deg/s). Satellite roller screws are off-the-shelf units with strengthened nuts and special lubrication. The electronic components are also selected from high temperature catalogues.

Due to the considerable length versus diameter ratio of the system, the static bending of the AIA is considerable. A mechanism setting the rod length allows to compensate the bending of the elements when the arm is fully extended; as a result, the

end-effector position error versus static model (taking into account the nominal length of the rods, not the corrected one) based on the position given by the sensors is 3 mm only at this position. However, in other positions, larger errors can be measured, up to 350 mm. The reason is the torsion of the tubes that cannot be compensated for, and the bending torque value on the parallelogram mechanisms that depends on the position of the end-effector. As a result, a flexible model of the AIA mechanism has been set up by CEA [4] in order to predict the bending of the structure in every position. The details of the flexible model are developed in Appendix A.

2.2.2. PAC

The PAC [33] shown in Fig. 2-5 is a 6 m long robotic manipulator capable of carrying a 1 kg payload at its end. The outer diameter of the PAC segment is 100 mm. It has been developed for the inspection of hot cells at AREVA-NC by CEA-LIST. These inspections are subject to normal atmospheric and temperature conditions, but the radiation level is high because the PAC has to withstand a total dose of 10 kGy.

Fig. 2-5: The PAC robot operating in an AREVA-NC hot cell for field testing.

Dexterity is a key feature for this robot, as the hot cell is featured with a very complex assembly of pipes. Therefore, PAC has the same multi-segment architecture with a vertical parallelogram mechanism as the AIA, which it actually inspired [34] with 5 segments and 10 degrees of freedom. PAC differs from the AIA in that its parallelogram mechanism is balanced with a glass fibre spring.

Considering the small size of the penetration hole into the hot cell, the robot carries a 10 kGy hardened NEUROBOT multiplexing system and amplifiers. Operational electronics appears to be the limiting element in this environment. In order to cope with the small penetration hole, small and thus low-power DC motors are used, just as in the AIA, leading to the same low joint velocities.

The PAC shows the same flexible behaviour as the AIA. The flexible model developed in Appendix A can be used to predict its flexible behaviour as well.

2.2.3. MASCOT Boom

The boom carrying the MASCOT manipulator inside the JET's vacuum vessel, depicted in Fig. 2-6, is a 10 m long robotic manipulator with 18 degrees of freedom, entering the vessel through one of the equatorial openings. This robotic manipulator operates in normal atmospheric and temperature conditions and has been developed to withstand a dose rate of 4.5 mG/h [38]. It can carry a 440 kg payload – usually the force-feedback manipulator MASCOT [9], but also other large components such as heating antennas using specially designed end-effectors. It has become a key element of JET [26][27].
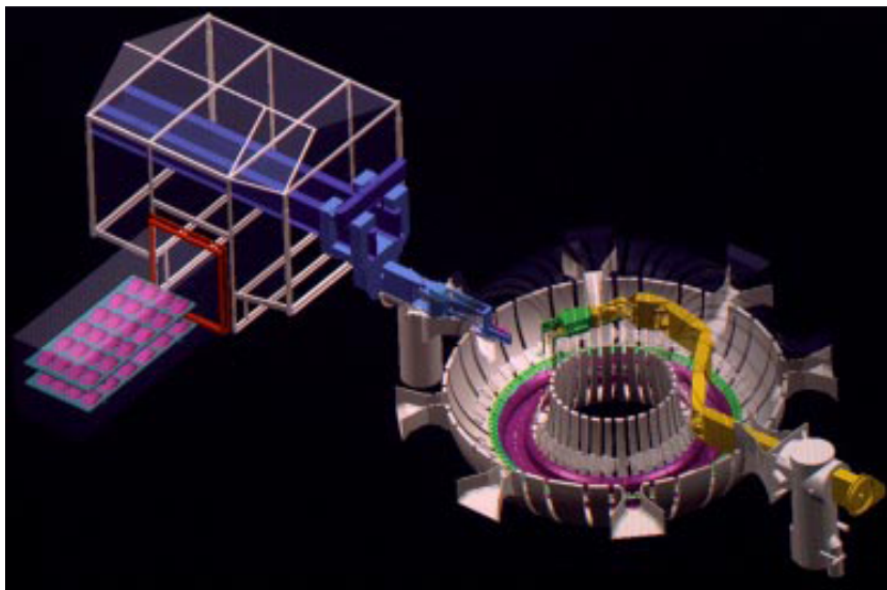
**Fig. 2-6: Remote operations scenario in JET vacuum vessel
with the MASCOT manipulator at the end of the boom.**

The device uses standard motors driven through Harmonic Drive gearboxes. No electronic processing occurs in-vessel; every sensor and actuator is directly connected to the cubicle 100 m away. Position feedback is conducted with resolvers and potentiometers.

The joint position feedback utilises a redundant sensor system composed of a resolver and potentiometer for each joint. Potentiometers are redundant sensors; they are not used for normal operation as they are too inaccurate, but they allow the withdrawal of the robotic manipulator in case the resolvers fail. Radiation levels forbid the use of off-the-shelf incremental encoders.

The MASCOT manipulator is actuated by standard asynchronous motors with tachometers and resolvers for velocity and position feedback. Transmission is done through cable and pulley mechanisms. Once again, the manipulator actuators and sensors are directly connected to the cubicle without any in-vessel electronic processing.

2.3. Robots and magnetic fields: MRI Compatible Robotics

Generally, a high magnetic field should be considered an uncommon design constraint for robots. In fact, only recently have high-sustained magnetic fields been possible, with the development of superconducting magnets; copper magnets can produce high fields of up to several tens of T, but only for a limited time. The robot will simply wait until the field dissipates to perform an inspection. Moreover, a large workspace robot is only needed if the inspection area or volume is sufficiently large, and in extent a dextrous robot as well. Therefore, only the most recent superconducting magnets are large enough to require inspection using dextrous robots.

On a much smaller scale, robots are used to place objects with precise positioning under a high field. This function proves to be of interest for some chirurgical and mini-invasive surgical interventions, in order to place a probe or a seed accurately using MRI.

Most of MRI assisted robots have been actuated far from the field in order to avoid perturbation of the device, but also perturbation of the field, which causes image distortion [5][29]. Fig. 2-7 shows two examples of MRI compatible positioning devices. In the robot developed by the Harvard Medical School [5], the first MRI compatible robot presented in a conference paper, only the long passive rods made of titanium alloy or composite material actually penetrate the high strength field (>0.5 T).

Another robot, designed to be placed inside the MRI borehole, has been developed by John Hopkins University [29], as shown in Fig. 2-7. This design was claimed to be the 'first fully MRI compatible robot' tested up to 7 T. The robot features a complete non-electrical device completely manufactured of paramagnetic materials in order to avoid disturbing the field. The design is based on special pneumatic stepper motors and optical encoders with a deported light source for accurate movements (fractions of a millimetre).
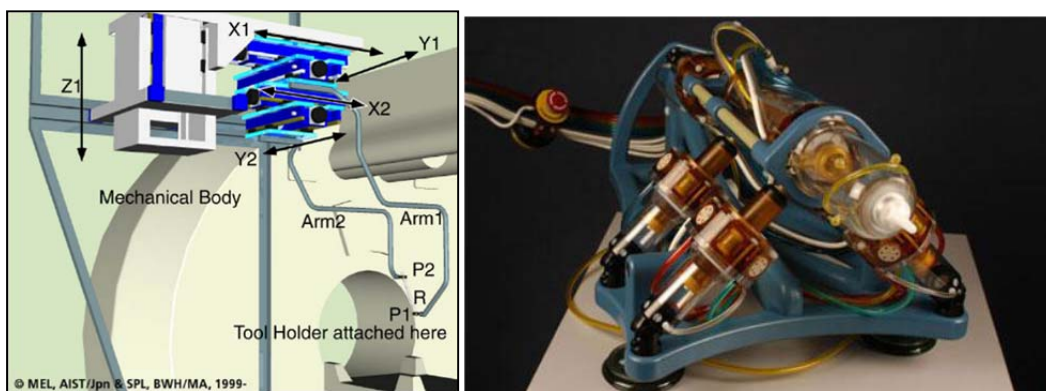
Fig. 2-7: MRI compatible positioning devices
(left at Harvard Medical School [5], right at Johns Hopkins Medical Institutions [29]).

Further developments based on these positioning devices have notably led to the design of a force-feedback mini-invasive neurosurgery robot called the NeuroArm [46]. This device, controlled by a surgeon in an immersive environment (Fig. 2-8, uses

piezoelectric actuators and optical sensors, as well as force sensors based on material photoelasticity. The arms in themselves, operating within the MRI active volume, are manufactured with PEEK plastic and titanium.

Fig. 2-8: The NeuroArm [46].
Down: the robot operating in MRI environment (left) and around a patient mock-up (right). Upper picture shows the surgeon's immersive environment with the haptic master devices.

MRI compatibility is a constraint on the capacity of the device to operate inside the magnetic field environment, but also to avoid perturbing the images of the MRI by emitting or disturbing the local magnetic field. Except for this constraint, the environment is considered normal (temperature, pressure), since an operating room actually features very stable conditions.

In order to prepare for the design of MRI compatible robots, an intensive work on the characterization of robotics components has been carried out. The goal of this work was to determine which robotic components are actually MRI compatible, and to design new concepts where no off-the-shelf design was available. Reference [52] explains the theory on which this perturbation is based, and then gives for instance a glance on a series of robotic components that are proved to be MRI compatible through in-field testing. Results show that non-magnetic materials should be preferred, typically ceramics, plastics and titanium alloys, key properties being magnetic susceptibility and conductivity. In terms of actuation, piezoelectric devices show to be one of the best choices; but despite its low current consumption, the requirements are such that they

should be placed far away from the MRI active volume. Shape memory alloys come second: they show good magnetic properties, but are difficult to model in environments showing unstable temperature. Sensing can be done using optical fibre or at least light based sensors – copper loops showing high induction because of the high frequency component of the magnetic field, making them impossible to use in an MRI.

2.4.   Summary of Hardening Technologies

2.4.1.   Managing the high temperature design constraint

Given the high temperature design constraint, all the material's structural properties, particularly tensile strength and elasticity modulus, must be considered at both 120°C and 200°C in baking conditions. As a result, for example, most aluminium alloys cannot be used for structural elements because their properties are greatly reduced at this temperature. The AIA experience from Tore Supra and, more generally, tokamak diagnostics experience indicate that part lubrication in mechanisms but also motors and gearboxes require careful design.

In a high temperature vacuum vessel the majority of energy is exchanged via infrared radiation. Two different strategies may be applied to keep the temperature of the components within an acceptable range, as noted below.

2.4.1.1   Temperature repartition

For components that may withstand temperature as high as 120°C, and 200°C in the case of baking, the best way is to ensure that all the parts in the robotic manipulator stay at 120°C. Indeed, if the different parts of the robot are at significantly different temperatures, thermal expansion may result in gaps or additional stresses in the mechanism. Some components, namely motors and electronics, may also dissipate power when operating and, consequently, heat up. They should be cooled down to 120°C.

Therefore, temperature repartition is a specific challenge. This problem can be avoided by ensuring that all of the robotic components are at the same temperature – 120°C. This approach requires careful design of the thermal links between parts, and of the outer parts which will have to exchange heat with the vacuum vessel, kept at 120°C. Particularly, the outer parts of the robotic manipulator should behave like black bodies with a high radiation emissivity coefficient. Indeed, with a high emissivity coefficient, the heat exchange due to radiation with the vacuum vessel's first wall is more efficient.

Structural materials may also be chosen with coefficients of thermal expansion near one another. If a material with a different dilatation constant is necessary, extra care must be taken when designing the robotic manipulator because all parts are machined, assembled and tested at room temperature (20°C).

2.4.1.2 Temperature containment

Every design might include some components that cannot be exposed to high temperatures. If this is the case, the temperature must be kept lower than 120°C. The most common solution is to design a liquid or gas cooling system with a heat exchanger outside the bioshield of the reactor, where temperature is kept reasonably low.

A passive solution would take advantage of thermal inertia and exchange rates to confine the sensible items into a 'thermal cage' included in the robotic manipulator but made of reflective material. Indeed, as the inspection robotic manipulator is in UHV, the main heat transfer mode is infrared radiation, and a cage made of material that reflects infrared would take more time to reach the nominal temperature. Careful dimensioning may allow the components inside the cage to be functional for a sufficient period of time to proceed with the inspection. The design should address the links between the cage and the robotic manipulator itself, as they should be designed with thermal insulation to slow down the conduction of heat.

In the case where the whole robotic manipulator would be kept at low temperatures, the outer parts that are directly exposed to radiation from the vessel should reflect infrared radiation. Conduction links between the inspection robotic manipulator and the vessel should be carefully designed as well to limit heat exchange.

The latter design solution is actually the exact opposite of the temperature repartition design strategy presented above. If these two solutions must be used for different components, then an accurate thermal design model should be provided for both, which is difficult for thermal repartition when assembly design gets complex. The purpose of baking is also to perform outgassing on the components by purposely applying a high temperature; if some parts do not reach the outgassing temperature for long enough, extra care must be taken against outgassing during operation in the UHV.

2.4.2. Managing the Ultra-High Vacuum design constraint

Since the UHV (10^{-5}Pa) in the vacuum vessel has to be kept clean at all costs, vacuum-facing components must be free of any outgassing materials. A list of vacuum-agreed components and materials can be found in the ITER Vacuum Handbook [56]; every vacuum-facing component has to be certified for this use. Outgassing materials are usually oils, greases and organic materials, but not exclusively because some metals, such as steel and most materials subject to oxidation, also have this feature.

As a result, every rolling component exposed to the UHV must be lubricated with non-standard processes, such as molybdenum disulphide MoS_2 deposit. This lubrication technique has been used extensively in fusion tokamak diagnostics.

The purpose of the baking process is essentially to free every part of the robotic manipulator from any little outgassing air pockets that can be found in the imperfections of the assembly, for example, and to remove any traces of hydrogen and oxygen that remain in the material porosities. If a robot subsystem is not baked in reasonable time, then solutions to avoid these porosities must be investigated.

Every component that cannot be certified to UHV use must be avoided or confined in an UHV-proof sealed space. Sealing solutions for this purpose exist, such as those used in the AIA with Helicoflex and metal seals that are also tolerant of radiation. In the current state of the art, the presence of the high magnetic field means that solutions for transmitting continuously rotating movement through an UHV-proof barrier are unable to operate. As a result, any movement to be transmitted through an UHV-proof box, from a vacuum-sensitive motor for example, has to be converted into linear movement and transmitted through flexible leak-tight bellows.

2.4.3. Managing the high radiation design constraint

ITER inspection robotic manipulators are under high restrictions in terms of radiation. As explained in Table 1-1, the expected gamma radiation doses are 1500 Gy/h in the case of a scheduled inspection, and 10 times more for unscheduled inspections, for a maximum total dose of 27 MGy. These values are 10 to 100 times higher than those achieved in nuclear fission applications, such as the PAC, which are rated for a total dose of 10 kGy. Structural materials should not be subject to degradation due to radiation. Radiation-sensitive components like seals and other parts made with plastics or rubber must be chosen with care. The only barrier against irradiation is mass; however, the dimensions of the robotic manipulator do not permit the design of an efficient barrier against radiation.

Every component in an inspection robotic manipulator should therefore be tested to ensure its functionality up to the specified radiation dose. ITER has started so-called RADTOL-programs for this purpose, the results of which are gathered in the ITER Radiation Hardness Manual [3].

During the preliminary years of the ITER experiments, little or no contamination or activation will occur in the vacuum vessel. The vacuum vessel will become radiation activated when the D-T test campaigns begin. Considering that these tests are progressive with an increasing level of tritium, the 10 kGy rated components, such as those used in the PAC, will presumably meet the ITER vacuum vessel radiation requirements during the first years of the ITER fusion experiments. After the D-T campaigns have begun, ITER inspection robotic manipulators will have to contain only 10 MGy-hardened components.

2.4.4. Conclusion of the state of art

The AIA robotic manipulator features a long reach and high dexterity, and it demonstrated possibilities of inspection in the Tore Supra experimental fusion reactor under UHV and 120°C. The PAC, another long-reach dextrous robotic manipulator based on the same mechanism as the AIA, is qualified for radiation doses up to 10 kGy, mainly due to the electronics. 10 kGy is far from the ITER requirement of 10 MGy, but the RADTOL programs active in ITER assess and test the radiation tolerance of fusion diagnostics and maintenance equipment components, including a series of simple

electronic components based on radiation-tolerant transistors. The research and development of radiation tolerant electronics for ITER inspection robotic manipulators is beyond the scope for this thesis. The analysis of the state of the art shows that the constraint of a highly dextrous robotic manipulator going through a tight opening has been solved before, as shown by the example of the PAC, the AIA and the MASCOT Boom. These robotic manipulators contain innovative mechanical design features for reducing the size and weight of the joint actuators in particular.

The remainder of this thesis uses the modular structure of the PAC and the AIA as the reference structure for the conceptual ITER inspection robotic manipulator design. The parallelogram kinematic structure used in these robots will be used in particular in chapter 4. The structure is depicted in Appendix A, along with useful kinematics and flexibility models developed for the PAC and the AIA. The scientific developments on this parallelogram structure (kinematic forward model, flexibility model, simulation program presented in Appendix B, current geometry of the structural parts of the AIA) will be used with only minor changes in the scope of this study, therefore they will be set out of the scope of the thesis.

The effects of the magnetic field on a robot have not been investigated until recently, and only in the field of medical robotics for manipulation inside an MRI machine. In medical applications, high temperatures, UHV and high gamma radiation are irrelevant – they are relevant for ITER inspection robotic manipulators. In addition, MRI robots have a particular constraint not to disturb the local field, called MRI compatibility, which does not apply to ITER inspection robotic manipulators. As a result, most technologies used for MRI compatible robot designs will be inoperative for ITER inspection if directly used. Therefore, all technical solutions required for ITER inspection robotic manipulators must be carefully reviewed and, in particular, the effects of a high magnetic field must be checked.

The only systems that exceed the ITER inspection environment are fusion diagnostics systems, as they cannot be removed and need to operate along with the plasma. However, these systems are rugged, not even close to a complete robotic manipulator design, in order to cope with the environmental conditions. The IVVS proposal from ENEA is one example among others of what may be done in the inspection conditions. Diagnostics in other large machines using high fields, such as the LHC, are also of interest, although no moving systems are provided there.

The temperature, UHV and radiation effects on robots have thus been addressed in different robot designs before, even though they were never all faced by the same design, except for tokamak diagnostics systems which are too rugged for the application sought. The techniques for each of those constraints were summed up in this chapter. Hardening studies demonstrate that their combined effects, as difficult as they may be to handle, can be addressed by choosing components wisely.

The activity in MRI compatibility has generated a considerable amount of work in designing MRI compatible devices for robots that can operate in a high magnetic field. Even though these technologies are not applicable directly, this work will be the starting

point of the study, both for the theory of the effects of magnetic field on devices and for the selection of the principles that can effectively work in a high magnetic field environment.

2.4.5. Thesis developments restrictions

Considering the novelty of the magnetic field design constraint on robots, this is the central topic of this thesis. Other environmental constraints will be dealt with using state-of-the-art techniques summed up in this section. Once the different effects of static magnetic fields are stated, this knowledge will be applied along with the state-of-the-art techniques for radiation, temperature and UHV in order to design robot components for actuation, structural design, sensing and data processing that can operate in the ITER inspection environment.

A conceptual design of a robotic manipulator carrying an IVVS probe will then be developed, based on the architecture of the AIA and the PAC, but using the components proofed to high magnetic fields. The purpose of this robotic manipulator will be to enhance the inspection capacity of the IVVS by setting more than 99% of the first wall in view of the probe. The design of the probe will be the one suggested by ENEA presented in section 2.1.3, therefore it is not considered in the scope of the thesis, even though recommendations on its design will be issued. The current detailed design of the structural parts of the AIA will be used as a base in order to evaluate the weight of the system. Tools already developed by CEA (kinematics models, flexible models, control scheme shown in Appendix A, simulation program in Appendix B) will be extensively used in this conceptual design phase, but their development is considered out of the scope of the thesis as they will be used with only minor modifications to take into account the effects of the magnetic field.

In order to be able to review the effects of a magnetic field on the different elements of a robotic manipulator, the following section will detail the theory of magnetostatics and the different phenomena that will result in perturbations or potential new applications for robots.

2.5. Magnetism concepts and effects

This section presents the theoretical background of static and quasi-static electromagnetism concepts and effects relevant to the design of inspection robotic manipulators for ITER vacuum vessel inspection without considering the propagation phenomenon of fields. Moreover, applications of these electromagnetic fundamentals to typical robotic structural, actuator and sensor materials are presented to show the effects of the magnetic field on them. In particular, theoretical developments illustrate how robot material selection affects the robot load carrying capacity and its performance under high magnetic fields. The phenomena responsible for induced voltages are also explained and their equations identified. The equations for the forces that a conductor with a flowing current undergoes are also detailed in this chapter, with the specific

application on a conducting part in which an induced voltage is generated by movement in a magnetic field.

2.5.1. Maxwell's equations

Maxwell's equations are the set of four basic equations that describe classical electromagnetism [11]:

$$Gauss'\,law : \oiint_V \vec{E} \cdot \vec{dA} = \frac{Q(V)}{\varepsilon_0} \quad \Leftrightarrow \quad div\,\vec{E} = \frac{\rho(V)}{\varepsilon_0} \tag{2-1}$$

$$Gauss'\,law\,for\,magnetism : \oiint_V \vec{B} \cdot \vec{dA} = 0 \quad \Leftrightarrow \quad div\,\vec{B} = 0 \tag{2-2}$$

$$Faraday's\,law\,of\,induction : \oint_S \vec{E}.\vec{dl} = -\frac{\partial}{\partial t}\iint_S \vec{B}.\vec{dS} \quad \Leftrightarrow \quad \overrightarrow{rot\,E} = -\frac{\partial \vec{B}}{\partial t} \tag{2-3}$$

$$Ampere's\,circuital\,law : \oint_S \vec{B} \cdot \vec{dl} = \mu_0 I_S + \mu_0 \varepsilon_0.\frac{\partial}{\partial t}\iint_S \vec{E}.\vec{dS} \quad \Leftrightarrow \quad \overrightarrow{rot\,B} = \mu_0\left(\vec{j} + \varepsilon_0 \frac{\partial \vec{E}}{\partial t}\right)$$

$$\tag{2-4}$$

Of interest for this study is the interaction between the magnetic field **B** and the local electric field **E** that will result in forces (**F**=q.**E**) and inducted voltages.

Equation (2-1), Gauss' law, the first in Maxwell's equations, gives a relation between the flux of the electric field through a closed surface depending on the repartition of charges in the volume V inside this closed surface, written Q(V). In the case of an electrically neutral environment, the flux of the electric field should be zero, which means that the electric field lines should loop back inside this volume when no charges are present in the volume. Gauss' law for magnetism in (2-2) gives the same statement for magnetic fields, except that the flux of a magnetic field through a surface is always zero. These two equations will not be used thereafter because they show the way that electric and magnetic fields are diffused through a volume, but do not show the way in which they interact in various mediums. Indeed, the key medium parameters for magnetic and electric fields are the magnetic permeability of vacuum μ_0 and electrical permittivity of vacuum ε_0, neither of which are present in these two first equations (2-1) and (2-2) (in the case of ε_0 the mean charge is always zero; so the parameter cannot apply).

The third of Maxwell's equations is called Faraday's law of induction (2-3). This equation will be used extensively. Faraday's law of induction states that a variation of a magnetic field for any reference results in the creation of an electric field, which in turn may cause a force on charges or a voltage drop and therefore an induced current in materials, referred to as eddy currents.

Ampere's circuital law, the fourth of Maxwell's equations (2-4), is used to calculate the magnetic field's flux density **B** given a repartition of current **j**. Coupling this equation to Faraday's law of induction (2-3) reveals that a magnetic field eventually fights any event that will result in its modification.

The expression of the magnetic force, named Laplace force (2-5), can be derived from Faraday's law of induction [11]. This force applies when there is no local electrical field (the first expression applies to a charge q moving at velocity **V**, the second to a strand of a conductor depicted by **dL** that is delivering the current i):

$$Laplace\,Force: \vec{F_L} = q.\vec{V} \times \vec{B} \quad \Leftrightarrow \quad \vec{F_L} = i.\vec{dL} \times \vec{B} \tag{2-5}$$

2.5.2. Materials magnetisation

When considering a material, many atomic phenomena result in macroscopic behaviour. These phenomena actually influence the way the material reacts to the presence of a magnetic field of strength H, namely how much the magnetic field flux density B is present in the material, which is described by the magnetisation equation, also called the B-H curve. The reference of these curves is the magnetisation of vacuum, for which the equation $B = \mu_0.H$ applies, where μ_0 is the magnetic permeability of vacuum [11].

Different types of material, regrouped according to their B-H relationship and explained in the following sections, are presented in Fig. 2-9. The magnetic permeability of the material is μ; B_{sat} is the saturation magnetic field of a ferromagnetic material; and H_{c1} and H_{c2} are the two critical magnetic field strengths of a type II superconductor. The different B-H relationships show that the magnetic permeability of a material is not always constant, but also depends on the value of the magnetic field strength H [11].

The most significant effect due to the B-H curve shape is the force a magnetic field can generate due to its distribution on a piece of material, even if it is not moving. In order to illustrate this effect, let us consider a large volume free of any particle affected by a magnetic field whose strength is H. The result is a magnetic field flux density **B**$_{vac}$ in this volume whose gradient **grad**(||**B**$_{vac}$||) may not be null depending on the spatial distribution of **H** according to the B-H curve of vacuum.

Now, with the presence of a small object of volume V_0 in this large volume of vacuum, the magnetic field flux density **B**$_{mat}$ inside the material will again be deducted from **H**, but this time according to the B-H relationship of the material. Locally, on outer surfaces of the volume V_0 of the object, that are parallel to the flux lines, this results in a step in B across the surface as illustrated in Fig. 2-10, which according to Ampere's law (2-4) is equivalent to the presence of current on the surface. This current in turn generates a force that is proportional to (**B**$_{mat}$-**B**$_{vac}$). The opposite surface of the material faces the same (**B**$_{mat}$-**B**$_{vac}$) proportional force, except that its value has changed according to **grad**(||**B**$_{vac}$||). Therefore, the resulting force is proportional to the difference (**B**$_{mat}$-**B**$_{vac}$) computed locally and to the local gradient **grad**(||**B**$_{vac}$||).
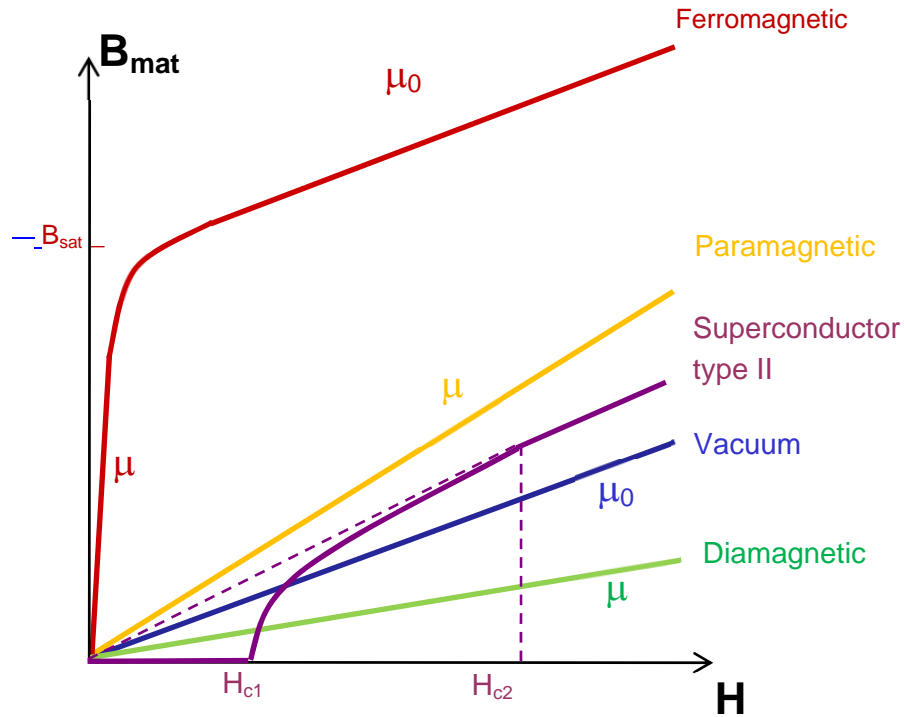
Fig. 2-9: Typical B-H curves.

Finally, the following equation (2-6), whose development is explained in [11], gives the expression of the volume magnetic force **F$_v$**, with the magnetisation **M** of the material being defined by the equation $\overrightarrow{B_{mat}} = \mu_0\left(\overrightarrow{H} + \overrightarrow{M}\right) = \overrightarrow{B_{vac}} + \mu_0.\overrightarrow{M}$:

$$Volume\,magnetic\,force: \overrightarrow{F_v} = \overrightarrow{grad}\left(\overrightarrow{M}.\overrightarrow{B_{vac}}\right) = \frac{\overrightarrow{grad}\left(\overrightarrow{B_{mat}}.\overrightarrow{B_{vac}}\right) - 2\left\|\overrightarrow{B_{vac}}\right\|.\overrightarrow{grad}\left(\left\|\overrightarrow{B_{vac}}\right\|\right)}{\mu_0} \quad \textbf{(2-6)}$$
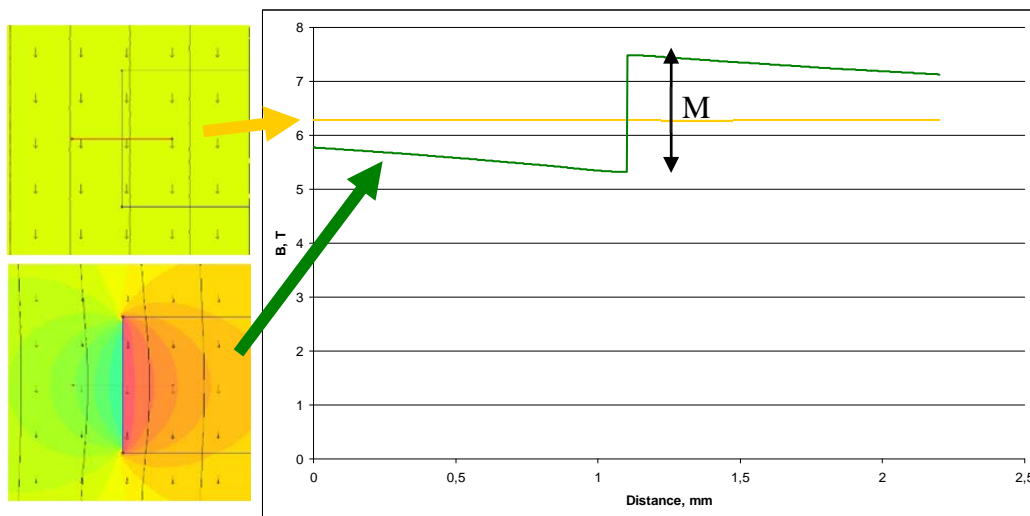
Fig. 2-10: B at the boundary of a piece of material.
The orange curve shows magnetisation in vacuum when the part is not present; the green curve shows magnetisation with the part. Part position is given on the left drawings by a blue circle. Right graph curves are plotted across the part surface (along the red line on the left drawing).

2.5.2.1 Paramagnetic materials

Paramagnetic material behaviour in a magnetic field is characterised by a B-H curve (pictured in yellow in Fig. 2-9) that is linear and going through the point (B=0, H=0). Interestingly, a vacuum, taken as the reference medium, shows a paramagnetic behaviour (blue line in Fig. 2-9) with a slope factor of μ_0, its magnetic permeability. In a paramagnetic material in general, the proportionality factor is the permeability of the material μ, equal to $\mu_r.\mu_0$ and $\mu_0.(1+\chi_m)$, where μ_r and χ_m are also material characteristics, the relative permittivity and the magnetic susceptibility respectively. For the material to be paramagnetic, χ_m must be positive, which means $\mu>\mu_0$. The B-H curve equation for paramagnetic materials is [11]:

$$\overrightarrow{B_{mat}} = \mu_0\left(1+\chi_m\right).\overrightarrow{H} \quad \Leftrightarrow \quad \overrightarrow{M} = \frac{\chi_m.\overrightarrow{B_{vac}}}{\mu_0} \qquad \text{(2-7)}$$

Developing from equation (2-6), this leads to the volume force on a paramagnetic material:

$$\overrightarrow{F_v^{para}} = \frac{2\chi_m.\left\|\overrightarrow{B_{vac}}\right\|.\overrightarrow{grad}\left(\left\|\overrightarrow{B_{vac}}\right\|\right)}{\mu_0} \qquad \text{(2-8)}$$

There are two different groups of material with a positive χ_m: a group in which the magnetic susceptibility is much smaller than 1 (such as aluminium at 2.1×10^{-5}, but also magnesium, lithium, titanium, etc.), which is *strico sensu*, the group of paramagnetic materials, and another group with a magnetic susceptibility far greater than 1, like Permalloy nickel alloy with a susceptibility of 10^8. This last group is the group of ferromagnetic materials described in detail in section 2.5.2.3. Ferromagnetic materials have the same behaviour as paramagnetic materials until $B_{vac}=B_{sat}/\mu_r$, but show a saturation phenomenon thereafter.

In a magnetic field, a paramagnetic material will have to withstand a magnetisation force towards higher fields. This attraction increases with the value of the local field and local gradient. A lower susceptibility leads to lower forces.

2.5.2.2 Diamagnetic materials

Materials categorised as diamagnetics show the same linear B-H curve as paramagnetics (green curve in Fig. 2-9), except that their magnetic susceptibility χ_m is negative, leading to $\mu<\mu_0$ [11]. Equations (2-7) and (2-8) apply for diamagnetic materials as well, with $\chi_m<0$.

Magnetic susceptibilities for these materials range from -9.7×10^{-6} for copper or brass to -1.6×10^{-4} for bismuth, which is the pure elemental material with the 'highest' negative χ_m value.

In a magnetic field, a diamagnetic material must withstand a magnetisation force towards lower fields, with the same observations as for paramagnetic materials; the

repulsion gets higher with the value of the local field, and a lower susceptibility (in absolute value) leads to lower forces.

2.5.2.3 Ferromagnetic materials

A ferromagnetic material (red curve in Fig. 2-9) shows a B-H curve that, for high fields, may be described by the following equations (when $\mathbf{B_{mat}}$ and $\mathbf{B_{vac}}$ are aligned) with B_{sat} being the saturation magnetic field flux density, which is a material parameter [11]:

$$\overrightarrow{B_{mat}^{ferro}} = \mu_r.\mu_0.\overrightarrow{H} \quad for \left\|\overrightarrow{B_{vac}}\right\| < \frac{B_{sat}}{\mu_r}$$

$$\left\|\overrightarrow{B_{mat}^{ferro}}\right\| = B_{sat} + \mu_0.\left\|\overrightarrow{H}\right\| = B_{sat} + \left\|\overrightarrow{B_{vac}}\right\| \quad for \left\|\overrightarrow{B_{vac}}\right\| > \frac{B_{sat}}{\mu_r} \tag{2-9}$$

Considering the common values for ferromagnetic materials of the permeability $\mu = \mu_r.\mu_0$ (several orders of magnitude higher than μ_0) and of the saturation field B_{sat} (no more than 2.5 T), the case $\|\mathbf{B_{vac}}\| < B_{sat}/\mu_r$ is definitely not applicable in high magnetic fields addressed in ITER (5 to 8 T – ref Table 1-1). For $\|\mathbf{B_{vac}}\| < B_{sat}/\mu_r$, the vector $\mathbf{B_{mat}}$ is aligned with $\mathbf{B_{vac}}$, which leads to $\mu_0.\|\mathbf{M}\| = B_{sat}$ and, developing from equation (2-6):

$$\overrightarrow{F_v^{ferro}} = \frac{B_{sat}.\overrightarrow{grad}\left(\left\|\overrightarrow{B_{vac}}\right\|\right)}{\mu_0} \quad for \left\|\overrightarrow{B_{vac}}\right\| > \frac{B_{sat}}{\mu_r} \tag{2-10}$$

Iron, nickel and cobalt alloys are typical examples of ferromagnetic materials. However, the presence of these elements in a specific alloy does not imply that the material is ferromagnetic. For example, there are some paramagnetic stainless steels, even though iron is their first component.

In a high magnetic field ($B_{vac} > 1$ T), a ferromagnetic material undergoes a high force towards higher fields, with once again the force being higher when the local gradient is higher.

2.5.2.4 Permanent magnets
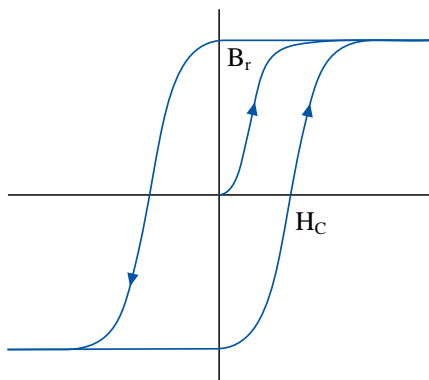
Fig. 2-11: Hysteresis loop of a permanent magnet. ver. axis: B, hor. axis: H

Permanent magnets are special combinations of elements characterised by high hysteresis loop on the B-H curve, as illustrated in Fig. 2-11 [11]. However, the saturation phenomenon is the same as for the ferromagnetic materials. The slope of the upper line is μ_0, but the slope from the (B=0, H=H_c) point is at least 10^3 times μ_0, up to 10^8 for Permalloy nickel alloy; practically, for $\|\mathbf{B_{vac}}\| > H_C/\mu_0$ plus epsilon, the magnet is on the μ_0 slope. When driven back at H=0, there is a remnant field B_r in the magnet, which is the remnant magnetisation of the magnet. This magnetisation remains until an opposed magnetic field is applied, with a strength equal to at least H_C, which is called the coercive field strength of the magnet. At this point, the magnet is demagnetised.

The magnetic power enclosed by the magnet is the product of B_r and H_C. It is the reference parameter, expressed commonly in the state of the art in G.Oe (CSG units for magnetic field flux density, G, and for magnetic field strength, Oe; the equivalent SI unit is J/m^3, with 1 MG.Oe = 7.95 kJ/m^3). Neodymium magnets are the most powerful state-of-the-art magnets, with a power density of 48 MG.Oe. Samarium-cobalt magnets are also of interest, with a power density of up to 28 MG.Oe.

The main point of using magnets is therefore to provide the presence of a magnetic field for actuation or sensing. This property is actually lost when dealing with high fields (above 1.5 T) as the H_C is no higher than 1 MA/m for current state-of-the-art technology, matching 1.25 T in free air. For higher values of H, the magnetisation of the magnet is lost, the magnet is remagnetised according to the local field $\mathbf{B_{vac}}$ and it acts like a ferromagnetic material with $B_{sat}=B_r$. Therefore, the magnetisation force is similar to that developed in ferromagnetic materials in high fields, given by equation (2-10).

Magnets are also affected by temperature [11]; they lose all their specific magnetic properties at a temperature called the Curie temperature, which is a property of the material: 320°C for Neodymium magnets [62] and 800°C for Samarium Cobalt magnets [63]. However, H_C reduces as the temperature of the magnet gets closer to the Curie temperature and does not rise back until a high strength remagnetisation field is applied; Neodymium magnets should not be brought to temperatures higher than 180°C [62], while Samarium Cobalt magnets may be used at temperatures as high as 320°C [63]. As a result, samarium cobalt magnets are the most powerful magnets that may be used in the ITER inspection environment. Neodymium magnets should be used with much greater precaution.

2.5.2.5   Superconductive materials

A superconducting material is a two-state material, whose resistivity switches to zero when temperature and magnetic field conditions are met. Whether the material is in a superconducting state or not is a function of the temperature and the value of the local magnetic field. The temperature and magnetic field must be kept below a material's specific limit to show zero electrical resistivity, and thus to be in a superconducting state. When the material is not in a superconducting state, it behaves like a paramagnetic material and has a non-zero electrical resistivity.

There are two kinds of superconductive materials [54].

Type I superconductors are pure elements; most elements apply to this definition. In these materials, for magnetic field strength lower than the critical value H_C ($H<H_c$), B_{mat} stays at 0 T. Once the critical value H_c is passed, superconductivity disappears, and the B-H curve suddenly switches to the B=μ.H line. The highest value among type I superconductors of $\mu_0.H_c$ is 198 mT for Niobium (Nb). However, the critical temperature T_C for type I superconductors is extremely low – 9.5 K at most.

Type II superconductors (purple curve in Fig. 2-9) are typically alloys, even though a few pure elements are categorised as type II superconductors as well. Their magnetic behaviour is different from type I; B_{mat} stays at 0 T until $H<H_{c1}$, called the lower critical

field. Once the lower critical field is reached ($H=H_{c1}$), the material is still superconducting with its resistivity at zero, until the upper critical field is reached ($H=H_{c2}$) when the B-H curve is tangent to the $B=\mu.H$ line. Finally, superconductivity vanishes after the upper critical value H_{c2}. This field point H_{c2} may get quite high for alloys; at superfluid He temperatures (4.2 k), it measures 17.3 T for Nb_3Sn with T_C=18 K, 22 T for MgB_2 with T_C=39 K [47] and up to 140 T for YBCO with T_C=75 K [45]. Lower critical field value H_{c1} is much lower: 52 mT for Nb_3Sn, 31 mT for MgB_2 [47] and 110 mT for YBCO [24].

Therefore, if superconductor materials are the only possible 'magnetic insulators', this capability is highly dependent on the value of the external magnetic field. For the applications relevant to this thesis, the field values are too high for the insulation effect to be realistic enough for consideration. On the other hand, for the generation of a magnetisation force, the effect is much lower than what can be expected, for example, with ferromagnetic materials – even though it is the only way to generate even moderate forces towards lower fields. The force value for a given magnetic field strength H is given by the following equation (2-13), derived from (2-6), with B(H) being the expression of the B-H curve of the material – a function on H_c or H_{c1} and H_{c2} for a type I or type II superconducting material:

$$\overrightarrow{F_v^{SC}} = \frac{(B(H) - \mu_0 \cdot H).\overrightarrow{grad}\left(\left\|\overrightarrow{B_{vac}}\right\|\right)}{\mu_0}$$

(2-11)

2.5.3. Magnetic field effects on conducting materials

Even though conducting materials may not have high magnetic parameters (for example, for copper the magnetic susceptibility χ_m is -9.7×10^{-6}), they suffer magnetic field effects due to their electrical conductivity [11]. As is well known, an induced voltage generates high currents in conductive material bulk parts, which in turn generates an electric field and then a force. A conductor may also be used to carry a current, and in that case the carried current may be disturbed by the induced electric field between its ends.
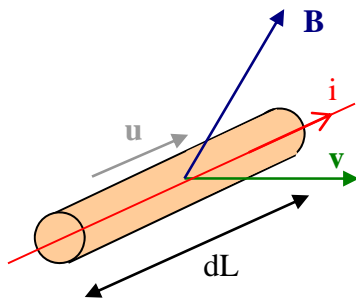
Fig. 2-12: Conductor wire.

2.5.3.1   Current carrier conductors

Let us consider a piece of conducting wire of length dL, along a unitary vector **u**, moving at a velocity **v** in a constant magnetic field **B**. The wire carries a current i along **u**.

According to Faraday's law of induction (2-3), the combination of movement and magnetic field generates a local induced electric field:

$$\overrightarrow{E} = \frac{i}{q}.dL.\overrightarrow{u} \times \overrightarrow{B} + \overrightarrow{v} \times \overrightarrow{B} = \overrightarrow{E_I} + \overrightarrow{E_V}$$

(2-12)

$\mathbf{E_I}$ is orthogonal to **u**, so it does not generate any induced voltage in the wire; however it does generate a force on the wire. On the other hand, $\mathbf{E_V}$ generates an induced voltage, but cannot generate any force as the total charge of the piece of conductor is zero and because the force from an electric field on a charge is $\mathbf{F}=q.\mathbf{E}$, with q being the total charge of the piece of conductor.

The force on the conductor is:

$$\overrightarrow{F_I} = i.dL.\vec{u} \times \vec{B} \qquad \text{(2-13)}$$

The induced voltage between the two ends of the conductor is:

$$dV = dL.\left(\vec{v} \times \vec{B}\right) \cdot \vec{u}. \qquad \text{(2-14)}$$

These equations may be used in order to evaluate the force and induced voltage that show in a wire conducting a current i in a magnetic field. These forces may be used to generate force or torque out of a piece of conductor where current is flowed, while the induced voltages may become problematic with network voltages.

An example of a multi-port planar conductor is shown in Fig. 2-13. In this planar conductor, the local field is normal to the plane. A current i flowing along **u** from port 1 to port 2 induces an electrical field in vector **n**, according to the previous expression of $\mathbf{E_I}$ in (2-15):

$$\overrightarrow{E_I} = -\frac{i.B.dL}{n_{e^-}.e.V}\vec{n} \qquad \text{(2-15)}$$

Fig. 2-13: 4-port conductor

With n_{e^-} being the charge carrier volume density, e the elementary charge of an electron, B the local magnetic field flux density value, dL the length of conductor along the current direction and V the total volume of the conductor carrying the current i.

In the example depicted in Fig. 2-13, the values of the voltage drops are as shown in (2-16), with V_{jk} being the voltage drop between port j and port k, and c the thickness of the element:

$$V_{43} = \frac{iB}{en_{e^-}.c} \quad V_{13} = V_{43}\Big/2 \quad V_{41} = V_{43}\Big/2 \qquad \text{(2-16)}$$

Therefore, it seems that conductive wires as well as multiport electronic components, such as transistors, can be affected by a magnetic field through Hall-effect induced voltages.

2.5.3.2 Conductive parts

According to Faraday's law of induction, Ohm's law ($\mathbf{E}=\mathbf{J}.\sigma$) and the Laplace force on a conductor (2-5), an elementary conductive part (volume $d\tau$, conductivity σ) moving at a velocity **v** in a constant field **B** undergoes a force against its movement that is expressed by the following equation, B_T being the value of the field projected on the plane normal to **v**:
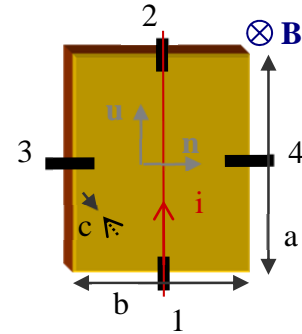
$$\vec{dF} = d\tau.\left(\sigma.\vec{v} \times \vec{B}\right) \times \vec{B} \implies \vec{dF}.\vec{v}/_v = -\sigma.v.d\tau.B_T^2 \tag{2-17}$$

However, this local expression of the current density $\mathbf{j} = \sigma.\mathbf{v} \times \mathbf{B}$ is not entirely valid for finite parts, as Gauss' law on a non-charged material states that div$\mathbf{j}$=0. This means that the current must flow back. Voltages generated by this effect are low, typically a mere few µV, which is enough to generate several A of current considering the conductivity of the material. However, these voltages are too low to cause current to flow across the gap between two parts. Therefore, the current must flow back through a circuit inside the geometrical boundaries of the part.

The eddy current drag force or torque can be calculated by estimating the shape of the current lines considering the shape of the part. This estimation allows computing the induced voltage along one current line, which is necessary to calculate the elementary force or torque undergone by a section of material around this current line. Finally, the total force or torque undergone by the part can be obtained by integrating this result along the current lines and adding the result of all the current lines.

For each current line, the force experienced by the material around this current line in a constant magnetic field, expressed by equation (2-17), due to movement is mathematically proportional to the magnetic field flux Φ through the surface swept by the current line during a time dt, divided by this value dt. In order to obtain the total force on the material around the current line in the case where $\mathbf{B}$ is constant and normal to the local velocity $\mathbf{v}$, the total force may be obtained by simply multiplying Φ/dt by the volume of material $d\tau$, the conductivity of the material σ and the value of B. Therefore, the resulting force differ between translational and rotational movement of the current line.

Fig. 2-14 shows the shape of this surface swept by a current line (in red) during time span dt, named S_{tran} and S_{rot} in the case respectively of a translation and a rotation. With B constant throughout space, the total magnetic flux Φ through S_{tran} is zero; however, in the flux through S_{rot} is not zero, causing an electromagnetic force to appear in the conductor, leading to a current and a drag force against the movement.
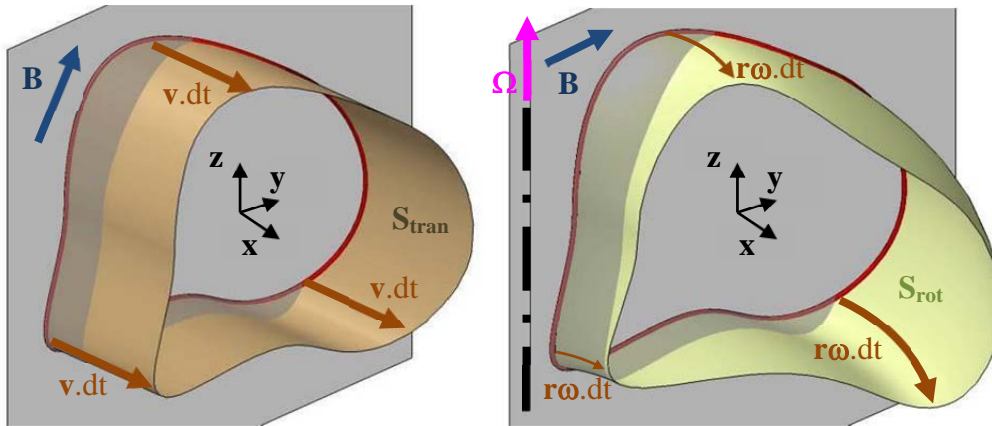
Fig. 2-14: Closed conducting strand moving in a constant field.
Left: pure translation. Right: rotation around an instant rotation axis.

As a result, translational velocities do not cause any drag force in a constant field environment. The instant radius of rotation does not have any effect either; only the angular velocity causes eddy currents to flow in a part. Of course, this analysis is not valid when the field is not constant, but its effect may be ignored if the field gradient is sufficiently low and the moving parts dimensions are considered sufficiently small, in which case the difference on B from one end of the part to the other is low enough to consider the magnetic flux Φ negligible.

Because electromotive force generation and mechanical force are linked together, it appears that a low gradient will require a very high current (resulting in heavy Joule losses) to generate high pure forces from a current flowed through a piece of conductor (a solenoid for example) when this piece of conductor is small in size. On the other hand, torques generated by rotating conductors with movement-generated current may reach high values in large fields even with small components.
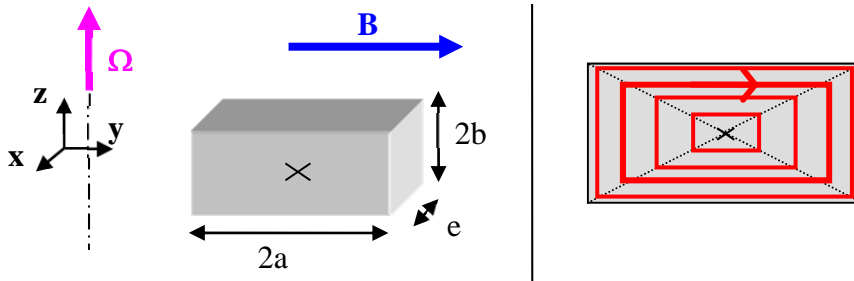
Fig. 2-15: Eddy currents drag problem.
Right figure shows a cut of the grey part normal to the velocity vector and the eddy current circuit estimated.

For example, the value of the drag torque undergone by the grey part in Fig. 2-15 that is fighting the rotational movement is given by equation (2-18). Current lines have been estimated to be normal to the velocity vector and drawn according to Fig. 2-15 to calculate the torque.

$$\overrightarrow{m}.\overrightarrow{\Omega}\big/\omega = -\omega.B^2.\sigma.\frac{a^3.b^3.e}{a^2+b^2} \tag{2-18}$$

where **m** is the torque generated by the effect of the magnetic field on the eddy currents, ω the value of the rotational velocity, **Ω** the rotation vector, **B** the local magnetic field density, σ the conductivity of the material and a, b and e parts dimensions according to the above figure (values given in the figure are set).

Induced currents may also generate heating by the Joule effect, which can also cause failure in the part due to excessive temperature.

2.6. Literature review conclusions

The goal of this chapter was to review the current state-of-the-art technologies applicable to long-reach inspection robotic manipulators used in extreme environmental conditions. This thesis is mainly concerned with robotics systems featuring many

degrees of freedom operating in high temperature ranging from 120°C to 200°C (when baking), under UHV, facing high gamma radiation levels (required accumulated dose is greater than 10 MGy at a dose rate of 1500 Gy/h) and in a high magnetic field (up to 8 T). The result of the analysis carried out in this state of art chapter showed that even though the temperature, UHV and radiation constraints are difficult to handle all at the same time, there are concepts that have been proven to work efficiently for dextrous robots in these conditions. However, the high magnetic field up to 8 T has been shown to be a very uncommon design constraint for robots. The focus of the present thesis has therefore been set on developing new design solutions for long-reach dexterous inspection robotic manipulators that are tolerant to high magnetic field.

The lack of existing robotic manipulator designs that are able to operate with high dexterity in a large workspace in ITER environment also provides motivation to this work. This is indeed a particularly critical issue presently being discussed in the ITER organisation. The main question is whether the constraint of the high magnetic field on the inspection robotic manipulators task operation should be removed and how much this would affect the availability of the tokamak.

This chapter also presents the theoretical basics that are necessary to understand and estimate the effects of a high magnetic field on different types of structural, actuation and sensing robot components. This chapter acts as a reference to well-known basic quasi-static magnetic theory, based on Maxwell equations, discussed extensively in the literature as the starting point of electromagnetism theory. In this chapter three basic phenomena have been identified, presented and discussed:

- The eddy current drag force due to the induced eddy currents in parts and assemblies. The critical parameter here is the conductivity of the material σ. A simplified approach would state that the effect of a magnetic field change on conductive materials is a force that tends to follow that change and nullify it.

- The induced voltages in conductors, due to the movement of a closed loop in a magnetic field. The generated voltage may be an issue in an electronic network if it gets too high. The surface of the loop and its velocity are the critical parameters.

- Due to the gradient of the field, the magnetisation force behaves in a similar way as the Archimedes' thrust. In free air (or water) compressed by gravity, volumes with higher density than the reference medium go down towards higher pressure fields and volumes with lower density go up towards a lower pressure field. Magnetisation of the materials (characterised by their B-H curves at a given H value) act the same way as density, with vacuum magnetisation as the reference instead of the air density; the force gets more intense with magnetisation difference, field gradient and field value.

3. DEVELOPMENTS: ELIGIBLE TECHNOLOGIES FOR MAGNETIC HARDENING

The theoretical background on static and quasi-static electromagnetism concepts and effects relevant to the design of inspection robotic manipulators has been presented. Based on these developments, this chapter presents the magnetic field effects on a selection of typical robotic structural, actuation and sensing materials. This chapter shows the main developments of the thesis, which aim to study how magnetic field effects on inspection robotic manipulator performance can be minimised or used as a design advantage.

The previous chapter showed that the magnetic field is a particular design constraint that can cause robot performance degradation due to the large external magnetic forces, induced currents and heating, and demagnetisation of magnets. However, in everyday life, whenever a contactless device requires an operation, it uses a magnetic field – for actuation in motors, for navigation using compasses, etc. ITER has high magnetic fields between 5 and 8 T, which is quite strong compared to any standard. For comparison, a permanent magnet-produced field is not usually higher than 1.2 T, and the magnetic field produced by the Earth is a about 10^{-5} T. High magnetic field of ITER therefore opens a wide range of enhanced operational possibilities for the robot actuators.

Generally, the components in the robotic manipulators can be divided into four groups:

- Structural components, namely the parts that are supporting the forces.
- Actuation components responsible for the movement of the robotic manipulator such as motors but also their transmissions and passive actuators like springs.
- Sensing components, for information feedback to the robot control and the supervision system.
- Information processing units and information transfer components.

For these components, this chapter reviews the available materials and actuators, sensing components and information processing technologies for finding the suitable ones to be used in the extremely high 5 to 8 T magnetic field in ITER. Some of these components can be characterised as 'magnetic tolerant', meaning that their operation is affected by high magnetic fields, but not sufficiently to impair their operation. An important finding of this thesis is that active actuator and sensor components can actually be designed to take advantage of the ITER magnetic field for improved performance, such as higher torque from motors or ways to measure the absolute position of the robotic manipulator. As a result, as far as actuators and sensors are

concerned, both an amagnetic solution and a solution that is using the magnetic field are suggested.

In order to evaluate the order of magnitude of the aforementioned effects, and characterise the operability of the studied components in ITER, this chapter begins by introducing the cartography of the ITER magnetic field, featuring values for magnetic field flux density and its gradient. A review of the available materials and actuators, sensing components and information processing technologies for ITER's extremely high 4 to 8 T magnetic fields is provided later on in the chapter.

In order to validate the technologies that have been developed, a magnetic field generator has been designed, for a field value of 1T across a 80x40x40 mm3 volume. The last section of this chapter details the design of the generator.

3.1.   ITER toroidal magnetic field configuration

The ITER toroidal magnetic field is generated by eighteen superconducting coils (n_C=18) each featuring n_T=134 turns, with a nominal current I_{nom} of 68 kA. Considering the torus shape of the ITER machine, shown in Fig. 3-1 and assuming that the turns and the coils are uniformly spread inside of the vacuum vessel, the magnetic field's only component is the toroidal component B_θ.

Applying Ampere's circuital law (2-4) on a horizontal circle centred at the torus axis gives the following expression for the toroidal component of the magnetic field B_θ as a function of the radial position of the considered point:

$$2\pi.r.B_\theta(r) = \mu 0.n_T n_C.I_{nom} \quad \Rightarrow \quad B_\theta = \frac{\mu 0.n_T n_C.I_{nom}}{2\pi.r} \tag{3-1}$$

Therefore, the gradient of the field **gradB** is consistent on the radial axis only:

$$\left\|\overrightarrow{gradB}\right\| = \frac{\partial B}{\partial r} = -\frac{\mu 0.n_T n_C.I_{nom}}{2\pi.r^2} \tag{3-2}$$
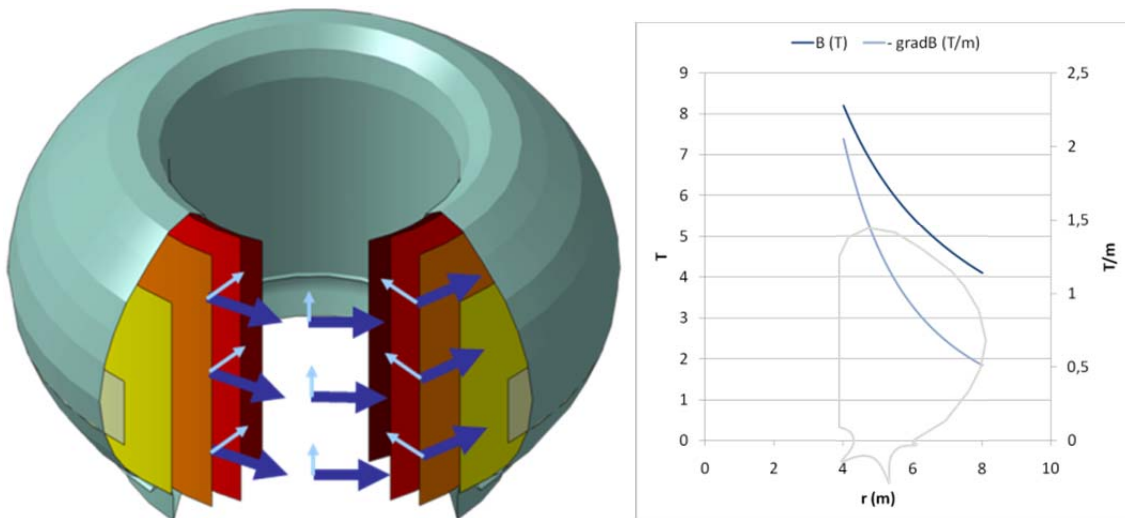

Fig. 3-1: ITER magnetic field configuration and values.
Dark blue: B(T), light blue: gradB(T/m). The profile in grey is given as a scale for the radius.

According to Fig. 3-1, the magnetic field flux density is high (4 to 8 T) over the full radius range. The field gradient proves also to be relatively low (0.5 to 2 T.m^{-1}) because it leads to magnetic field flux density drops of a few mT when considering distances of a few mm.

In the following analysis, robotic inspection is assumed to be carried out under constant magnetic field condition. The special superconducting coil failure case called quench causing a fast decrease of coil current and thus magnetic field that can occur while the inspection robotic manipulator is inside the torus is left out of the scope of this study. However, an important design constraint considered is that the inspection robot must withstand a magnetic field shutting off while parked because the transfer casks cannot operate while the magnetic field is on. The IVVS specification gives a 0.3 T field in the parked configuration; the toroidal magnet Design Description Document gives 11 s for the electrical time constant [57], which in turn gives the maximum magnetic field variation of 27 mT/s.
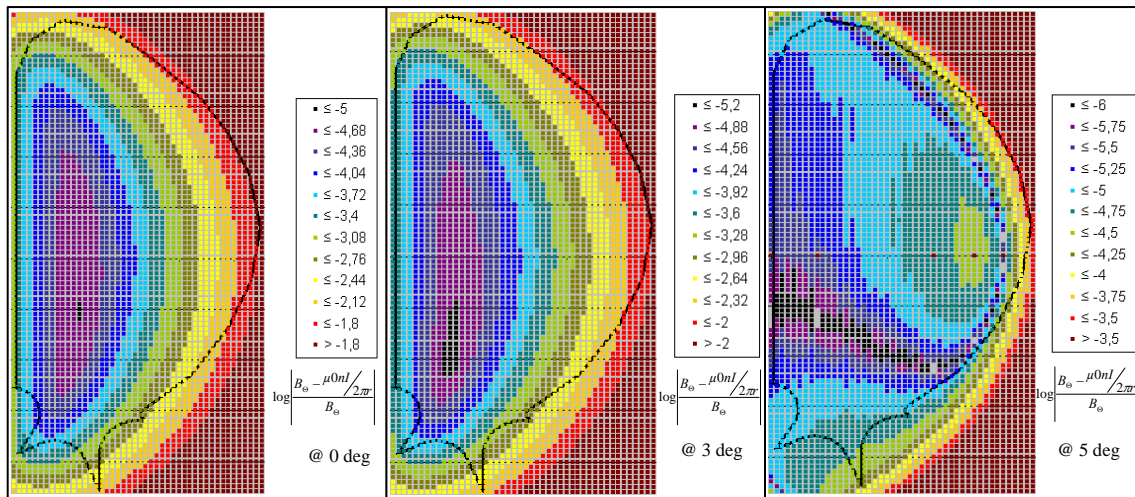
Fig. 3-2: Ampere's Law error versus finite element calculation of magnetic field.
Each picture shows the result at different angles from the coil plane – there is a coil every 20 deg. Pictured value, plotted in the section plane of the torus (black contour shows the section of the first wall) is the error made on the value of the toroidal component of magnetic field when computing it with Ampere's law, in logarithmic scale. Values indicated are powers of 10.

The configuration of the ITER toroidal field computed by the finite element method that takes into account torque ripple due to the use of discrete coils is given in Appendix C. Fig. 3-2, taken from Appendix C, indicates that the approximation from Ampere's law shows good results, with a maximum error at the median plane between two toroidal coils of 1.5%. Other graphs in annex give the values of the different components of the field and its gradient and their proportion in the total norm. They show that as long as the considered position is inside the vessel and more than 1 m away from the first wall, the calculations above for B and gradB are accurate given a 0.3% error for B and 3% for gradB. However, when positions at distances closer than 1 m from the first wall are considered, the corresponding errors are 1.5% for B and up to

30% for gradB. As a result, the reference magnetic field configuration for this thesis will be the configuration given by equations (3-1) and (3-2), except when notified to the reader.

3.2. Structural design headlines

The main issue for the designer of structural parts for ITER inspection robotic manipulators is the choice of correct materials that avoid high magnetic forces. The fundamental expressions for these magnetic field generated forces were explained in chapter 2, sections 2.5.2 and 2.5.3.2.

3.2.1. Magnetisation force

The magnetisation force is due to the magnetisation of the material. It is directly proportional to the magnetic field gradient vector **gradB** oriented on the radial axis and to the material magnetic susceptibility. Fig. 3-3 shows the absolute value of this force for a selection of materials. The force vector is oriented towards the inner first wall, except for brass and beryllium alloy S-200 because of a negative susceptibility.

Even for paramagnetic materials such as stainless steel AISI 316L or aluminium nickel bronze alloy (Al-Ni bronze), referred to as 'amagnetic' materials, the force may be quite large in function of their actual magnetic susceptibility. Indeed, with $\chi_m=8 \times 10^{-3}$ [64], 316L stainless steel undergoes up to 2.8 kgf/kg, but with $\chi_m=3 \times 10^{-5}$ [64], titanium alloy Ti-6-4 faces no higher than 15.7×10^{-3} kgf/kg. Aluminium bronze alloy (Al bronze), commonly found in bushings for ITER diagnostics, shows a χ_m as high as 0.05 [55], leading to high magnetisation forces; Al-Ni bronze shows a good alternative solution with $\chi_m=3 \times 10^{-3}$ [55].
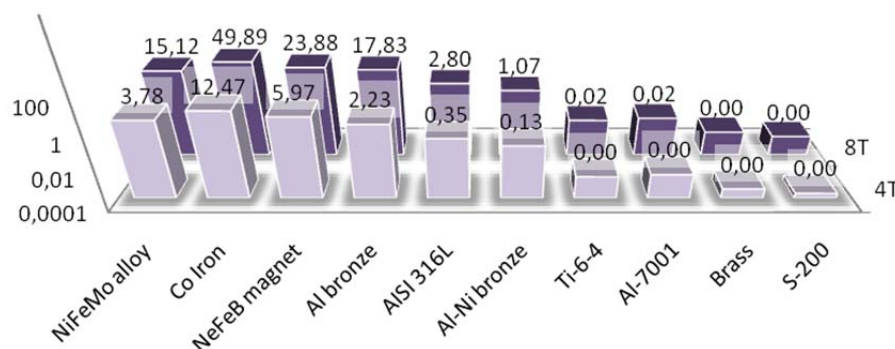
Fig. 3-3: Magnetisation force on materials per volume.
Forces are expressed in kgf/kg (force undergone by a 1 kg part, proportional to mass).

Ferromagnetic materials (NiFeMo supermalloy, cobalt iron) with their high magnetisation level lead to high magnetisation forces – up to 51.7 kgf/kg for cobalt iron, with $B_{sat}=2.34$ T [64]. Therefore, not surprisingly, the use of ferromagnetic materials for robot structural elements should be avoided. Materials used for magnets are subject to high magnetic forces in addition to undergoing remagnetisation.

Based on these results, titanium alloy Ti-6-4 seems to be a prime candidate for main structural parts of the robotic manipulator. Small parts requiring higher stiffness or strength may be manufactured in AISI 316L stainless steel, as magnetization force is proportional to the volume of material in the robot. The prime material for bushings is Al-Ni bronze.

3.2.2. Eddy current drag

The second force that structural parts encounter is the eddy currents drag due to movement as indicated in equation (2-17). Long-reach robotic manipulators with high length to diameter ratio are usually operated with slow velocities and in order to avoid structural vibrations; for example, in AIA and PAC, the individual joint velocities are no higher than a few 10^{-2} rad.s^{-1}. Even if they reach several metres in section length, the development in section 2.5.3.2 states that the radius of rotation has no significant effect on the eddy current drag torque. In order to compute the eddy current drag torque, an estimate of robot structural element velocity is needed. Experience reported from previous long-reach robotic manipulators, the AIA and the PAC, state that joint velocities should be set around 10^{-2} rad.s^{-1} in order to avoid exciting the structure's fundamental modes. This also leads to a lower torque needed from the motors due to the high gear ratio, which leads to smaller motors that can fit in the small feed through diameter.

Equation (2-18) in section 2.5.3.2 provides the joint torque necessary to move at 15 x 10^{-3} rad.s^{-1} around a vertical axis for a typical clevis part for a long-reach robotic manipulator described in Appendix A for carrying a 22 kg probe at 5 m. The part material is taken out of a selection of materials in an assumed constant field at different levels. The result is given in Fig. 3-4.
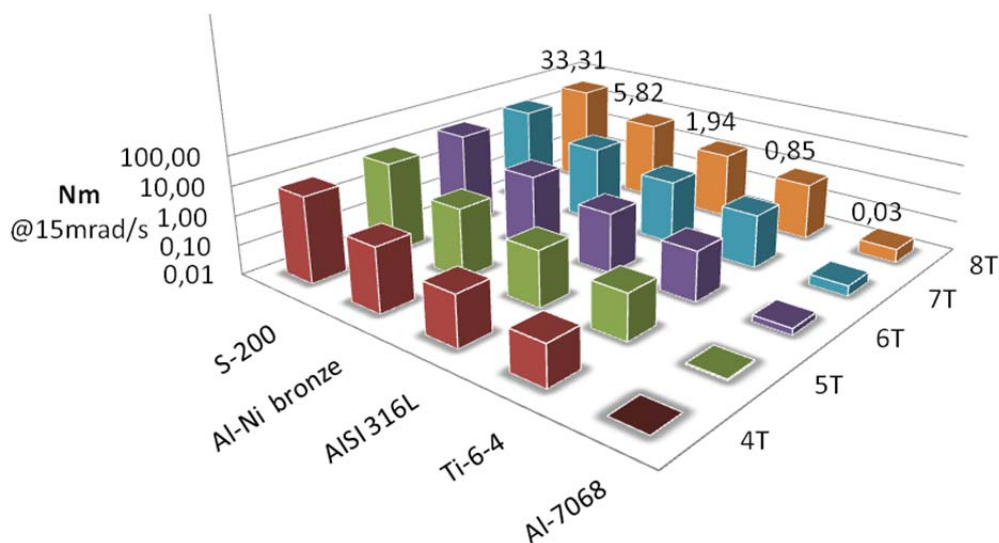
Fig. 3-4: Eddy current drag torque on a clevis part.
Computed for a part rotating at 15 mrad/s, for a set of materials and at different field values.

A second scenario considers a tube of the long-reach robotic manipulator architecture, which is considered to be a Ø160 mm, 2 mm thick and 1 m long tube. In this case, the angular velocity is also 15 mrad.s^{-1}. The results depicted in Fig. 3-5 do not take into account the gradient of the field.
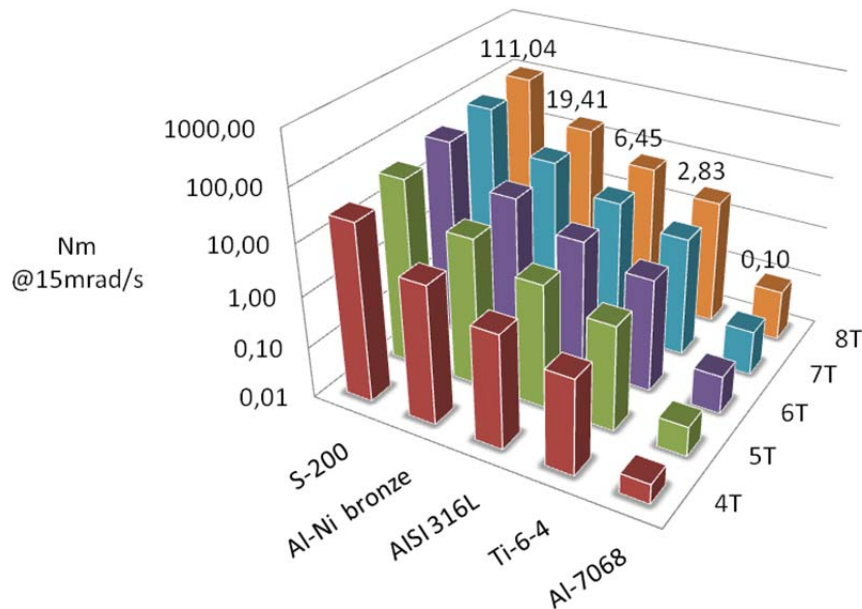
Fig. 3-5: Eddy current drag torque on a tube part.
Computed for a tube rotating at 15 mrad/s, for a set of materials and at different field values.

The critical parameter for this drag is the conductivity of the material. The problem is that considering the temperature, UHV and radiation constraints of the ITER inspection environment, metals cannot be avoided in the structural design. Therefore, eddy current will remain an issue, as conductivity of metals is no less than 1 MS/m.

According to Fig. 3-4 and Fig. 3-5, low-conductivity metals such as stainless steel 316L (σ=1.35 MS/m [64]) or titanium alloy Ti-6-4 (σ=0.56 MS/m [64]) actually generate minimal drag from eddy currents at the velocities considered. As a reminder, equation (2-18) shows that eddy current drag torque is proportional to angular velocity. Aluminium-zinc alloy Al-7068 performance is given as an indication for how low conductivity may get for metals (σ=10.24 kS/m [64]), but its operability in the ITER inspection environment is not certified. On the other hand, S-200 beryllium alloy, although interesting for the tubes because of its high stiffness to weight ratio (Young's modulus 303 GPa, density 1.84, against 138 GPa and 5.3 for Ti-6-4 and 210 GPa and 7.8 for AISI 316L, respectively [64]) is out of the question for parts set in rotation motion due to its high conductivity (σ=23 MS/m [64]) leading to high drag torques. For each joint, the eddy current drag torque should be computed for all of the parts set in rotation by the joint.

These analyses allow for choosing the best materials for the largest parts of the robotic manipulator that are set in motion by a rotation joint. There again, titanium alloy

proves to be the best choice for large structural parts such as clevises and tubes (Al-7068 aluminium alloy is not certified for use in ITER). For parts that are not set in motion by a rotation joint in which stiffness to weight ratio is critical, beryllium alloy S-200 can be used as well.

These scenarios show that eddy currents due to movements in structural parts should not be critical in terms of power, provided the parts are made with prime materials such as titanium alloy. Additionally, in the case where a quench occurs when the robotic manipulator is parked, eddy current forces should be low due to the configuration of the field, but the Joule heating may become critical. An analysis of this particular problem, which is a regular problem in diagnostics engineering at much higher local field values, will have to be provided at some point.

The eddy current drag may have another effect on long-reach robotic manipulators. Indeed, these robots are characterised by a low damping factor in fundamental modes of vibration, which may be additionally excited by the end effector tool motion. For example, the ENEA viewing prototype for the IVVS features a prism that is motioned at 1Hz, which is close to the expected fundamental mode of the robotic manipulator. These vibrations are difficult to be compensated by the robot actuators, as they are quite slow. An interesting feature is that the robot damping is in fact increased in the magnetic field due to the eddy current drag on the conductive parts in the same way as viscous friction, with eddy current drag being proportional to angular velocity. Therefore, it could be interesting to deliberately use highly conductive materials at strategic robot structure locations to increase the damping of the mechanism, and therefore increase the operational accuracy of the design.

These conductive parts must be carefully designed in order to keep the drag at an acceptable level during operation while affecting the damping factor. However, this investigation is beyond the scope of the thesis.

3.2.3. Recommendations on structural part design

The designer should pay close attention to the magnetic susceptibility χ_m and the conductivity σ of the materials chosen for structural purposes. Joint velocity may also have to be limited due to the eddy current drag at high velocity joints, such as end effector positioning joints, considering the limited space available that forbids using high power and therefore heavy actuators.

Among the materials selected, titanium alloy Ti-6-4 is the best choice for structural parts, as it shows practically no magnetisation force (15.7×10^{-3} kgf/kg) and low eddy current drag, with conductivity at 0.56 MS/m. AISI 316L is not recommended for larger parts principally because of its magnetic susceptibility, leading to magnetisation forces up to 2.8 kgf/kg. It may still be used for smaller parts requiring high strength, such as bearing spindles or gears. Beryllium alloy S-200 may be chosen only for parts that are not set in motion by a rotation joint, such as base parts or linear guide parts. Its high stiffness and low weight will lead to little flexibility, while its high conductivity will

severely dampen the vibrations at this level, which is a good thing for the accuracy of the robotic manipulator.

3.3. Actuation components

Because the considered robot is designed as a long-reach robotic manipulator in the same size range as the AIA (2.2.1), the torque to be developed by the actuators at the joint should be fairly similar, ranging from a few hundred Nm up to 1 kNm. With the actuation velocities around 10^{-2} rad.s^{-1} (5 mn for a full 180 deg stroke), based on experience from the AIA and PAC, the needed actuators are therefore in the 50–100 W range. These values include the losses in transmissions.

The present section surveys different amagnetic solutions for actuating a long reach inspection robotic manipulator, and then provides a solution that uses the field for actuation. Bearings and gears are also considered in this section.

3.3.1. Amagnetic designs

3.3.1.1 Ultrasonic motors

Some of these motors are compliant with the magnetic field, radiation and UHV directly off the shelf, which means they are definitely worth considering. Their maximum velocities range from a few dozen rpm to a few hundred rpm, but considering the non-conductive properties of the materials used (mostly ceramics) eddy currents should not be an issue – although the necessary reduction mechanism behind it will generate eddy current drag. The drawback of ultrasonic motors is the low power rating. For example, 80 mm diameter motors have a power rating of less than 25 W [65], which makes them unsuitable for actuation of the base links of a long-reach robotic manipulator. Another drawback is that ultrasonic motors need quite complex control electronics, which in ITER must be designed to be radiation tolerant.

As a result, ultrasonic motors may only be used in AIA-like architecture (Appendix A) in the light weight segments near the end-effector. In ITER diagnostics systems, the local field is commonly measured by turning a coil at known velocity. For such low power requirement application, ultrasonic motors can be quite ideal.

3.3.1.2 Water Hydraulics

Hydraulic actuators are commonly used in specific fields of robotics. Hydraulics are known to have high power to weight ratio and wide component selection, particularly for linear cylinder actuators, which makes hydraulics quite versatile. Such a variety allows the designer to avoid using reduction gears and other complex mechanisms that can cause undesirable weight increase and non-linearities, like backlash and friction, and eddy current drag in the specific case of an inspection robotic manipulator for ITER, as will be developed in section 3.3.3.

In ITER, however, use of oil hydraulics is prohibited because of the difficulty entailed in de-polluting the vacuum vessel in the case of an oil leak. For this reason, the only fluid power media accepted in the vacuum vessel are air, gaseous helium and water [56]. Pneumatics are difficult to use in flexible structures, as the pneumatic actuator itself has high compressibility. Therefore, the following paragraphs focus on the water hydraulic solutions.

Standard water hydraulics use stainless-steel cylinder actuators, motors and valves, mostly in stainless steel and chromate bronze [49]. For the application on a long-reach robotic manipulator with small outer diameter, water hydraulic motors cannot be used because of the limited availability of off-the-shelf motors of a few hundred Watt of rated power, their bulky size and their low performance at low velocities [49]. Linear cylinder actuators should be actuated by high pressure and low flow for high torque and slow velocities. Umbilical transmission line arrangement is known to be difficult design challenge for hydraulics, which is in particular critical for long-reach robotic manipulators as the small penetration hole diameter allows a limited number of cable and power feed-throughs.

Additionally, the operation of hydraulic valves can be a design challenge under high magnetic fields. Electro-hydraulic valve spools move due to the forces generated by proportional magnets or solenoids integrated into the valves. An external high field will prevent them from operating. Hydraulically or pneumatically actuated valves are also available [49]. However, this type of actuation increases the complexity and diameter of the umbilical. On the other hand, because the valves are made of stainless steel, which is subject to relatively high magnetisation forces (up to 2.4 kgf/kg according to section 3.2.1), there is a serious threat that standard valves will not operate properly. Of course, using re-designed valves made of more magnetic-tolerant materials is possible, but is probably an expensive solution. For these reasons, the valves should be kept away from the vacuum vessel and outside the cryostat.

Placing valves far away from a hydraulic jack induces additional flexibility in the structure. This design issue is briefly considered in the coming paragraph. For example, at 20 MPa pressure and with the water hydraulic bulk modulus E_{water}=2.2 GPa [49], the strain is 0.9% of the whole volume of medium between the actuator and the valve. This strain causes a displacement at the level of the hydraulic linear actuator.

$$Jack\ flexibility\ stroke = P/E_{water} \left(\frac{S_{pipe}}{S_{jack}}.L_{pipe} + L_{jack} \right) \qquad \textbf{(3-3)}$$

The above equation (3-3), derived from Hooke's law, states that at a given service pressure, the flexible stroke reduces with the length of the jack L_{jack}, the length of the pipe L_{pipe} and with the section ratio between the pipe and the jack S_{pipe}/S_{jack}. As an illustrative example, a 600 mm stroke jack developing 10 kN at 20 MPa pressure with a 5 m long ¼" pipe shows a rigidity of 1.2 kN/mm, equivalent to that of a Ø2 mm, 600 mm long steel rod. A jack similar in all terms except the service pressure, down at

20 bar, shows a rigidity of 17.4 kN/mm, equivalent to that of a 600 mm long steel rod measuring 8 mm in diameter.

More design conditions must be satisfied for the water hydraulic system to be amagnetic. The most important is the pressure medium. Deionised water or any other hydraulic medium featuring low conductivity must be used. Another important issue is the material used for the actuators and the power lines. In standard water hydraulic components, AISI 316L stainless steel is the rule. However, this would cause limitations because of the magnetic forces, both magnetisation and eddy current forces, as developed in section 3.2. Use of specially designed components made of titanium alloy should be investigated, as they divide the magnetisation force by 100 and the eddy current drag force in almost a half. Should stainless steel hydraulic jacks be used in the robotic manipulator, particularly near the end-effector, they would severely limit the reach and payload capability.

In order to satisfy the other constraints of the environment, achievements in the radiation hardening of the water hydraulics system of the Divertor Remote Handling equipment, which is 1 MGy rad-hard, should be investigated. Testing at higher doses up to 10 MGy has been carried out by TUT-IHA laboratories [48].
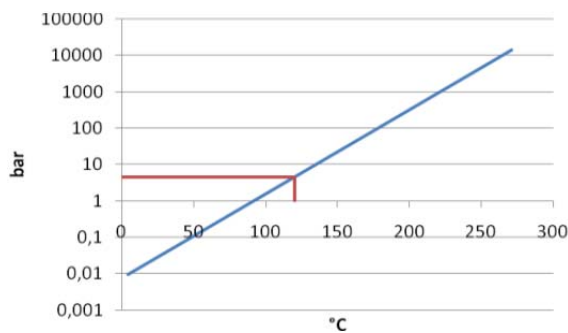
Fig. 3-6: Water vapour pressure vs. temp.
Vp (120°C) = 4.5 bar.

Temperature hardening is a known issue in water hydraulics, as standard systems should not operate higher than 50°C to avoid cavitation issues [49] due to the high value of the vapour pressure at these temperatures (see Fig. 3-6). The use of an over-pressurised secondary system apart from the pump and the valves should help improve operation and avoid cavitation in most critical components. As shown in Fig. 3-6, nowhere in this secondary system should the pressure go below 4.5 bar.

Leakage is a serious design challenge as well with respect to the ITER Ultra-high Vacuum requirements. Therefore, every single sealing point subject to leakage should be covered by a seal-tight box or by a set of vacuum-certified bellows for moving parts.

Double acting actuators require two power lines per actuator, while a single acting actuator, with spring return for instance, only requires one power line. Considering the small size of the feed through, single acting actuators are preferred.

3.3.2. Using the field with a DC motor

Electric actuation provides many advantages when dealing with long-reach robotic manipulators, particularly in terms of structural flexibility and compactness. Indeed, when using irreversible mechanisms – an electric motor driving a low pitch screw through a gearbox for instance – the global flexibility of the actuator is the actual

flexibility of the structural parts of the mechanism – the screw in the latter example. Electric motors use electric power, making the umbilical cable very compact. If electronic processing is allowed, several actuators may share a common wire for command that may also be common with the sensors as well, which are generally electronic. The main design issue is the reduction mechanism to be developed for each joint actuation, as the motor's operation point should be adapted to the force and velocity it must provide.

Brushless DC motors and synchronous motors rely on the field of a magnet. As stated in section 2.5.2.4, the magnetic field of a magnet is modified by the ITER field if it is not always aligned with it. As a result, brushless DC motors and synchronous motors cannot be used in ITER, as the magnet is turning with the shaft in these devices.

Induction or asynchronous motors use eddy currents to generate a current in the rotor coil by induction using the primary coil, generating in turn a torque. The rotor is therefore conductive and is subject to even higher forces from an external high field.

Stepper motors use another feature to generate torque and movement, the reluctance of an iron yoke-based magnetic circuit, which is actually saturated by the ITER external field: a stepper motor cannot work in ITER conditions.

In electromagnetic devices, torque and movement are actually generated out of the interaction of two magnetic fields, a stator field and a rotor field. One of these fields is set in motion by commutation, should it be by mechanical means as in brushed motors, or electronically as is in brushless, synchronous and asynchronous motors. The 'orientation' of this commutation must be in tune with the non-commuted magnetic field, which is why a brushless DC motors requires sensing the position of the magnet for switching between the coils in tune with it.
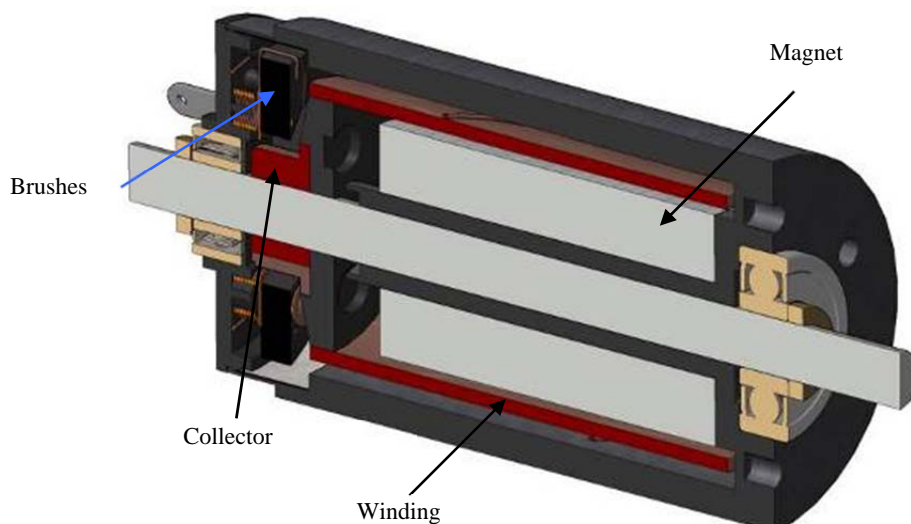

Fig. 3-7: Coreless brushed DC motor.

In the ITER inspection environment, there is already a stator field that is almost constant or slowly varying. The only motor design that features a constant stator field is

the brushed DC motor (Fig. 3-7) in which the field is provided by a stator magnet. The stator field is concentrated inside the hull of the motor by the ferromagnetic stator. The rotor and brushes have a specific orientation with respect to the magnet's magnetic field direction to make the whole system work. The magnetic field is perpendicular to the axis of the motor, and the brushes then control the orientation of the rotor's equivalent magnetic dipole, which is set at a 90 deg angle with the field. The orientation of the equivalent dipole is not dependant on the position of the rotor, thanks to the brushes and collector commutation.

Two possibilities have been investigated for using the principle of a brushed DC motor in the high magnetic field of ITER. These possibilities are presented in the following sections. A third section will then present the equations behind the operation, which are the same in both principles developed here.

3.3.2.1   Standard DC brushed motor in a magnetic field

In a strong external magnetic field, the magnetisation of materials is such that any magnet will be remagnetised in the local direction of the external magnetic field. But when the motor magnet magnetisation direction is the same as the external field whatever the position of the motor (which would happen in ITER if the motor is moving on the radial plane of the torus or if it is not moving at all) a brushed DC motor keeps functional – both with and without the magnetic field, with different performance in both cases. With the magnetic field shut off, the magnetic field value in the air-gap is the standard value from the motor stator magnet. With the magnetic field on, the field in the air-gap is slightly lower than the external field due to the presence of the yoke, leading to a different torque constant value as a function of the local value of the external field. The precise value of the torque constant should be assessed using a high magnetic field generator that matches the ITER's magnetic field – both in strength and local shape. Unfortunately, no such machine was available at the time of this study.

The motor ferromagnetic stator, which is necessary for the operation of the motor without a field, will undergo high forces with the magnetic field because it must be made in high field saturation material such as Hiperco cobalt iron (B_{sat}=2.34 T). According to the equation (2-10) from section 2.5.2.3, the resulting force ranges between 120 and 500 N per kilogram of yoke pulling towards the torus axis. The magnet will undergo a magnetisation force as well, between 60 and 240 N per kilogram of magnet for NeFeB and SmCo according to [62] and [63] (B_r~1.1 T).

In order to reduce the force on the bearings due to the magnetisation of the shaft, the standard shaft should be replaced by a paramagnetic one. Bearings should also be replaced by paramagnetic bearings.

As a result, in these specific conditions – namely the positioning of the device and the way it is moved around – a brushed DC motor can remain operational in the ITER inspection environment. Therefore, such a device would have many applications as a fixed actuator or for radial deployment.

3.3.2.2 Magnet-less brushed DC motor

However, the limitations of the above design are not compatible with a dextrous robotic manipulator, as the movements of the robot imply movements that are not compatible with a simple radial movement. Moreover, the strong forces on the design due to the magnetisation of the materials do not comply with long-reach robotic manipulators, as this would generate high torques at the base.

Therefore, a second option is necessary. The previous design proves that the magnet utility is only to provide the magnetic field. Therefore, in the case of a motor without magnet, a 'magnet-less' motor, where the magnetic field is not generated by a magnet but is simply the external magnetic field, the motor is operational provided that positioning conditions of the rotor shaft and the brush holder versus the direction of the magnetic field are met. In ITER, the external field is horizontal everywhere; if the motor is kept vertical in every configuration, then the magnetic field will always be perpendicular to the motor axis. This is the case in the PAC configuration with the vertical parallelogram; the motor is placed in the vertical joint region or in a tube that is not moved on its pitch axis.

The brush holder must still be placed correctly in relation to the local field orientation. For this purpose, the brush holding part is modified to allow movement around the motor axis. Then the brush holder must be actuated towards the correct orientation by a set of coils, for example, commanded from the base, which requires knowledge of the actual orientation of the field.

A passive option would consist of taking advantage of the magnetic field perpendicular orientation in relation to its gradient; the brush holder may be lined up with the field gradient by placing a small piece of ferromagnetic material out of axis. As the magnetisation force is collinear with the field gradient, the small ferromagnetic part acts as a compass to place the brush holder in the right direction.
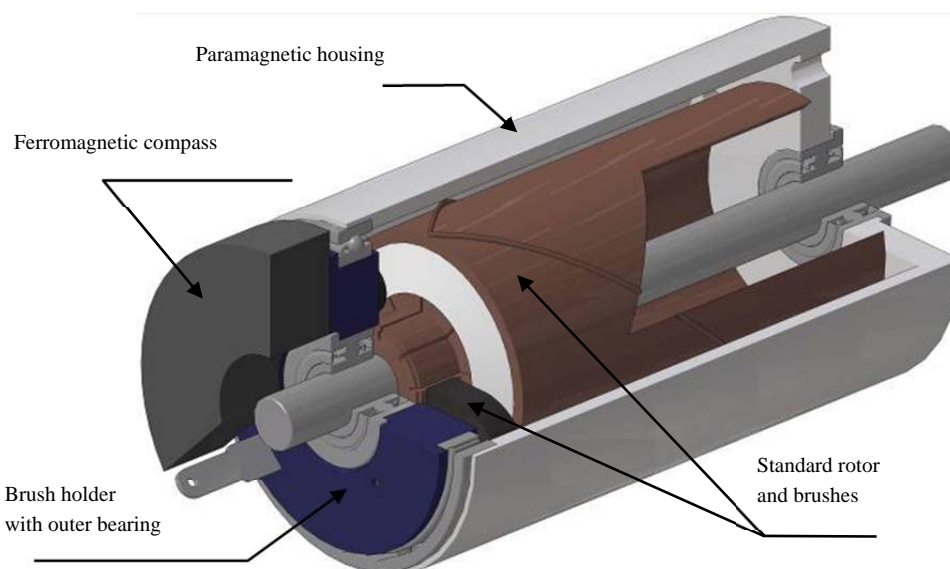

Fig. 3-8: Construction of the redesigned 'magnet-less' brushed DC motor with a standard rotor and brushes and a ferromagnetic compass.

Fig. 3-8 presents a credible construction for a magnet-less motor around a rotor and brushes that have been taken from a standard brushed DC motor. The magnet and the ferromagnetic housing account for 75% of the weight of a motor. Therefore removing the magnet and using lighter paramagnetic materials for the housing reduces the weight of the modified motor to much lower than the standard motor using the same rotor.

For the design to be completely magnetic tolerant, the ferromagnetic stator must be replaced by a paramagnetic housing. The shaft, made of high strength ferromagnetic steel, should also be replaced by a paramagnetic one with a low conductivity, such as stainless steel 316L or titanium alloy Ti-6-4. Additionally, UHV constraints do not apply here as the motor must be sealed in a leak-tight box, so other materials may also be used.

3.3.2.3 Motor parameters of a DC motor against a magnetic field

The following equations are valid for both a standard DC motor with magnet placed in a high magnetic field parallel to the magnet's magnetic field and for a DC motor without a magnet, using the external magnetic field.

A brushed DC motor has a simple proportional behaviour characterised by its torque constant K_T in Nm/A or V/(rad/s). According to theory [12], K_T is proportional to B. With nS the surface of the loop equivalent to the rotor construction, the following equations apply (with U being the electromotive force, ω the angular velocity, Cm the motor torque and I the motor current):

$$U = nS.B.\omega \quad Cm = nS.B.I \tag{3-4}$$

The magnetic field B_{mot} in the air-gap of a standard coreless brushed motor with a magnet has been measured at 0.7 T in the motor studied [68], which features a SmCo magnet. The previous equations mean that in ITER magnetic field, with a local value B_{loc}, a motor made of the same rotor will rotate more slowly than the original but will deliver more torque, just as with a reduction ratio of B_{loc}/B_{mot} – between 5.7 and 11.4 in the present case. Considering the low velocity and high torque required at the level of the joints, this proves to be a major asset for the design of a long-reach robotic manipulator.

On the other hand, in an environment where B varies with position, K_T shifts when this position is modified, for instance where the robot is moving. With a constant given supply voltage, the running velocity and torque of the motor next to the inner wall will be 4 times lower and higher than next to the outer wall respectively. This may prove to be a serious issue for the stability of the control of the design. However, because the system is a LVP (linear varying parameter) and the velocity of change of the position and therefore of the parameters is slow, simple robust command strategies, like gain scheduling, may be used. These have been used extensively in the state of the art [39][43].

However, the collector is a particular problem because it is supposed to carry electricity and therefore has a high conductivity; as developed in section 2.5.3.2, it may suffer from eddy current drag torque. In the studied motor (rated at 84 W), it is a 2r=Ø9 mm extruded ring, e=1 mm thick and l=6 mm long, and split into 9 independent sectors for commutation. Deriving from equation (2-18) given in section 2.5.3.2, written for a parallelepiped volume, considering that the collector is made of 9 individual parts of the same dimensions (2πr/9, l and e) and stating that the current goes on a close path, the equation of drag m due to eddy currents in the collector is given by the following equation, with ω being the shaft velocity, r and l the radius and length of the collector, σ the conductivity of the collector material and e the material thickness at the collector:

$$m = 9\omega B^2 \sigma . \frac{e^3 . \left(2\pi/9\, r\right)^3 . l}{e^2 + \left(2\pi/9\, r\right)^2} = \omega B^2 \sigma . \frac{8\left(\pi e l r\right)^3}{81e^2 + 4\pi^2 r^2} \tag{3-5}$$

The shaft velocity being inversely proportional to the field of the motor, as demonstrated by equation (3-4), the drag is *in fine* proportional to the field. Because the torque constant is also proportional to the field according to the same equation (3-4), the current needed to counter this drag is the same for any field value; for σ=60 MS/m (Cu), at a maximum velocity at 24 V of 1500 rpm for 4 T, this current is evaluated as being 150 mA. For comparison, the nominal current of the studied motor is 2.3 A.

The shaft replacement is less of an issue as a 316L Ø5 mm x 70 mm rod generates another eddy current drag still proportional to B² and ω, and then consumes the same current at all fields but at much lower values due to its size and the conductivity of the material. A 316L stainless steel will require 35 mA to turn at maximum velocity, 15 mA for a titanium alloy Ti-6-4 shaft and 0.5 mA for an aluminium-zinc alloy Al-7068 shaft.

It appears that off-the-shelf technology offers brushed coreless DC motors up to 250 W for motors measuring less than 80 mm in diameter [66]. Such technology is therefore able to develop even more than the 100 W required, provided the rotor fits into the maximum dimensions.

Due to the level of criticality of the component for the operation of the robotic manipulator, a prototype should be built out of a rotor and brushes from a standard motor and be tested in-field. Only the magnet-less motor may be tested. Indeed, testing a complete DC motor requires a machine generating high fields up to the level of ITER that is 4 to 8 T because of the presence of the iron core; no machine fitting these requirements was available for testing at the time. However, testing on the magnet-less motor is enough because the both designs should be run by the same equations.

3.3.3. Gears and transmissions

In gearings, the velocities of the gears, particularly in the first stage, will generate eddy current drag that may become critical for actuation. There again, as for all the components of the robotic manipulator, titanium alloy Ti-6-4 or stainless steel AISI 316L are the reference materials.

Therefore, an important point is the amount of drag a mechanism applies for a given gear ratio. Each mechanism requires a different kind of gear arrangement, and therefore will create a different drag force. For the same transmitted torque and primary radius, each gear (radius r, length L) may be modelled as a thick disc or a long fine cylinder, with respectively high and low module – low module gears can transmit less force per length and therefore, for transmitting the same torque than a higher module gear at the same radius, the length of the gear must be higher. For each of these two cases, with σ being the conductivity and ω the angular velocity, the drag torque is derived from the developments in section 2.5.3.2:

$$r \gg L \quad \left|m_{drag}\right| = \frac{\pi.\omega.\sigma.B^2}{4} L^3 r^2 + o\left(L^5\right)$$

$$r \ll L \quad \left|m_{drag}\right| = \frac{\pi.\omega.\sigma.B^2}{4} L r^4 + o\left(r^6/L\right)$$

(3-6)

These equations (3-6) are developed from equation (2-17), considering the return path of current in a cylinder and a disc.

In the following paragraphs, the performance parameter to consider is the total drag torque seen from the primary shaft minus the drag torque of the primary gear; the reference torque is the drag torque of the primary gear. This allows a comparison of different assemblies of gearings with different types of gearings (high and low modules, spur and planetary) for a given gear ratio and transmitted torque.

The simplest mechanism for reduction is spur gearing. The gears here are modelled as cylinders or discs of the same length. Because the gear ratio η is roughly the ratio of the two outer diameters, the different equations summed up in Table 3-1 may be applied. The gear is a velocity-reducing gear; therefore, if the primary gear may be a shaft or a disc, the secondary gear may only be a shaft if the primary gear is also a shaft, which explains why this case is greyed in the table.

Prim / Sec	r << L (shaft)	r >> L (disc)
r << L (shaft)	η^2	
r >> L (disc)	$\left(L/r_p\right)^2 \gg 1$	1

Table 3-1: Spur gearing drag performance.

When the system is primary-shaft/secondary-disc, the gear ratio is high ($r_p \ll L \ll r_s$). The equation mentioned in Table 3-1 for this case shows how drag behaves against shaft length and radius in the shaft/shaft case when the reduction ratio is increasing.

The case of conic gears is considered similar to two-disc spur gear.

A planetary gearing is a different concept; therefore, the equations are quite different. Two reduction ratios are evident: the nominal ratio η from the sun gear (primary) to the planet support, equal to $2(r_p+r_s)/r_s$ (r_p is the planetary gear radius, r_s the sun gear radius), and from the sun gear to the planetary gear equal to $(1+η)/η$. However, the planet support is less stressed than the gears; so it is thereafter assumed that it is made out of a non-conductive weaker material, like Al-7068. Table 3-2 presents the different formulas depending on whether gears with low module (shaft) or high module (disc) are used; k is the number of planets. Here, any combination of shaft and disc gear for the sun and the planets may be used.

Sun \ Plan	r << L (shaft)	r >> L (disc)
r << L (shaft)	$k\dfrac{(1+\eta)(\eta-2)^2}{4\eta}$	$\left(r_s\big/L\right)^2 k\dfrac{(1+\eta)(\eta-2)^4}{16\eta}$
r >> L (disc)	$\left(L\big/r_s\right)^2 k\dfrac{(1+\eta)(\eta-2)^2}{4\eta}$	$k\dfrac{(1+\eta)(\eta-2)^4}{16\eta}$

Table 3-2: Planetary gearing drag performance.

The sun-shaft/planet-disc implies that $r_S<<L<<r_P$, which expects a large gear ratio. On the other hand, a sun-disc planet-shaft system expects $r_P<<L<<r_S$: the gear ratio is 2, which is the smallest gear ratio considered with this mechanism. Equations in Table 3-2 present how drag torque depends on gear ratio, shaft length and radius at these limits.
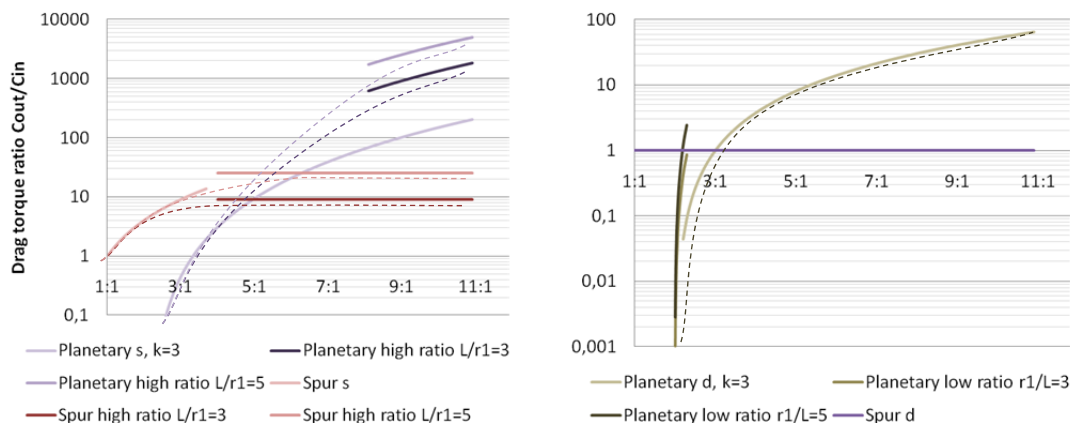
Fig. 3-9: Drag torque of the output gear in reduction gearings for a given input gear.
Drag torque is expressed as a multiple of the input gear drag torque, against the reduction ratio, as a function of the output gear shape. Left: input gear is a shaft. Right: input gear is a disc. There are 3 satellites in planetary gearings. Dotted lines are the expected curves based on trends.

The left graph in Fig. 3-9 permits choosing between a spur and a planetary gearing when the input gear is chosen with r<<L. For reduction ratios per stage lower than 4 or

5, using planetary gearing is preferred, while spur gearing will be better at high reduction ratios as the total drag is limited to $(L/r)^2$.

On the other hand, the right-hand figure, which presents the case when the input gear is a disc, reinforces once again that planetary gearings should be preferred for low stage reduction ratios no higher than 3. The case when the planetary gear is a shaft does not appear to be consistent, as it applies when the reduction ratio is close to 2, meaning that the planetary radius is small. When the reduction ratios are above 3, using spur gears is preferred as their drag ratio keeps to 1; the drag in the secondary gear (seen from the input shaft) is equal to the drag in the primary gear.

Another issue is the choice between shaft or disc input gear, based mainly on the strength of the material and the shape of the teeth. For a given transmitted torque, shaft gears will probably generate less drag torque than disc gears; however the curves in Fig. 3-9 show that a high reduction ratio mechanism generates a larger drag ratio for the shaft input gear (up to $(L/r)^2$) than for the disc input gear (up to 1).

3.3.4. Bearings

Rolling bearings such as ball or roller bearings present the same behaviour as the planetary gearing presented in 3.3.3. In these bearings, common sizing keeps the size of the balls or rollers lower than the size of the shaft; the equivalent reduction ratio of a planetary gearing is 3:1. The drag due to the rolling of the balls or rollers is thus less than 1 time the drag due to the section of the rolling shaft on the length of the bearing, which makes the bearing drag small compared to the drag of the axle. Of course, materials should be non-magnetic to avoid forces due to the magnetic field, which may be an issue for rolling materials if using metals.

Bushings, self-lubricating or dry, in the case they are made of conductive material like copper, are not a problem provided they do not move with the running parts (as they would when mounted on a drum running around a shaft for example). Of course, they should comply with the other environmental constraints, namely radiation and temperature. Vacuum-sensitive bearings and mechanisms should be kept enclosed in tightly sealed boxes.

3.4. Sensing

3.4.1. Amagnetic components

As potentiometers are not radiation resistant to the level of the MGy [3], the only remaining option for effectively measuring the position of a shaft by non-magnetic means is the rotary encoder slotted wheel with deported light source. The light source, sensitive to radiation, is kept on the safe side of the vacuum vessel and carried to the encoder wheel with radiation-hardened optical fibres.

The slotted wheel design should be carried out carefully. Indeed, of all sensors available on the market, this design is considered to be the most fragile component. On

the other hand, its angular velocity may lead to large structural stresses due to eddy currents, possibly leading to the destruction of the wheel. A limitation in velocity may be needed for this kind of sensor, entirely depending on its construction.

This is the solution that has been selected by ENEA for its IVVS proposal. It has also been suggested for MRI compatible designs [52][53] along with a series of designs allowing absolute positioning, with stacked slotted paths that give a grey code of the position. No publications address velocity limits to avoid damaging the wheel through eddy drag torque for this specific design.

3.4.2. From field cartography to positioning

ITER is, above all, a plasma confining machine; thus, its magnetic field is known with a high accuracy, as much as 1ppm accuracy according to [6]. The field in the vacuum vessel roughly being proportional to 1/r (r distance to torus vertical axis), a 10 ppm measurement of the magnetic field may give the radial distance with the same accuracy – that is a maximum of 0.8 mm. This technique has been successfully used in the Tore Supra tokamak to measure the real position of the torus' magnetic axis [6], and it is planned to be carried out in ITER as well [20].

Measuring the local field in several places on the robotic manipulator allows for computing of its absolute radial position in a global reference frame. A 3D measurement of the field would give the orientation of the part as well, which combined with part lengths finally allows the computation of the 6D absolute position of any part in the robotic manipulator with high precision using a single 3D Hall sensor per segment. This is an important asset for a robot with a flexible structure, even more so when this robot is carrying a metrology device such as the IVVS, which is supposed to carry out metrology measurements to ±0.5 mm accuracy.

3.4.3. Local absolute velocity sensors

Coils can be used to measure the velocity of a specific part measured in the global reference frame by measuring the back-EMF generated by the robot movement in the local magnetic field. A coil with surface S with n turns rotating at a velocity ω in a magnetic field $\mathbf{B_T}$ that is perpendicular to $\mathbf{\Omega}$ experiences the following electromagnetic force through its length: $U_{EMF} = nSB_T\omega$

For coils of moderate dimensions (maximum 10 mm) and at the considered velocities (ω=15 mrad/s), the voltages obtained are quite low, a few mV. For proper processing, this sensor requires amplification.

3.4.4. Resolver operation

A resolver is a variable ratio voltage transformer, with its ratio a function of the angular position of the rotor. The transformer is fed with a sinusoidal voltage, transmitted to the rotor by induction or by brushes, and transmitted to the secondary coils with the

variable ratio. With the presence of a magnetic field, there is a voltage that adds to the transmitted voltage in the rotor and therefore the current flowing in it.

The most common design of resolvers is the brushless induced voltage resolver. The rotor is composed of two distinct coils: the inducing coil, a coil whose axis is parallel to the shaft, and the transformer coil, a single coil which axis is perpendicular to the shaft. The stator is equipped with three coils, one for the induction of the rotor and two for the transformer at 90 deg phase, the cosine and sine coils. This phase is lower in multi-pole resolvers, as there are 2*p sets of coils for each of the sine and cosine output, p being the number of poles of the resolver.
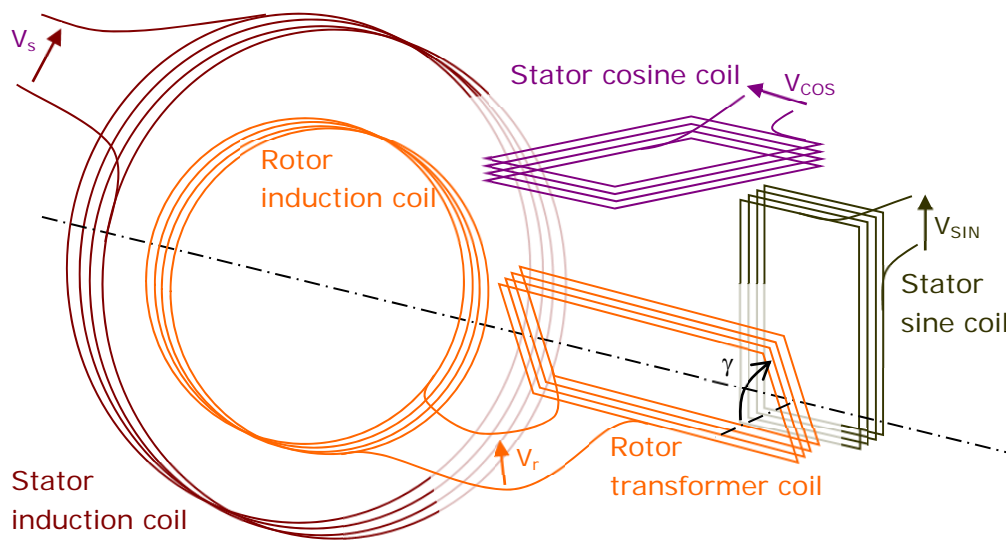

Fig. 3-10: Brushless resolver coil arrangement.

Therefore, V_{COS} and V_{SIN} are two 90 deg-phased electronic signals, V_{COS} being proportional to $\cos(\gamma_e)$ and V_{SIN} to $\sin(\gamma_e)$. The device is excited with a high frequency sinusoidal signal (a few kHz to 100 kHz – depending on the maximum shaft velocity) on V_S, transmitted to the rotor by induction. Electronic processing allows computation of the electrical angle γ_e linked to the mechanical angle γ, by using a fast loop that includes multipliers, a synchronous rectifier, an integrator, a voltage-controlled oscillator and an up-down counter in its simplest form. These operations may be achieved by simple designs with discrete transistors, as most of these circuits have been used in early analogue radio transmission and reception systems for a long time.

A standard resolver makes extensive use of iron yokes to transfer magnetic flux from one coil to another, which makes them non-usable as in the torus. A magnetic-tolerant resolver must be a specially designed item. The electromagnetic force on the rotor transformer coil might block the processing of the position with a classical operating scheme.
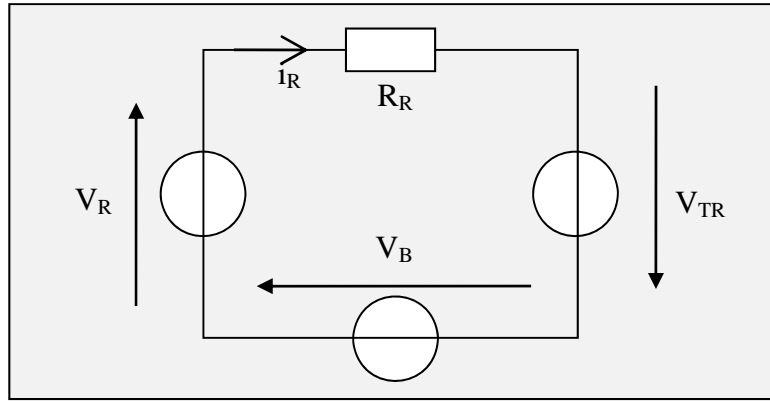
Fig. 3-11: Equivalent circuit of the resolver's rotor.

Using Fig. 3-11 notation, V_R is proportional to V_S, and V_{COS} and V_{SIN} are proportional to $V_{TR}.\cos\gamma$ and $V_{TR}.\sin\gamma$ respectively. V_B is proportional to $\gamma'.B_T.\cos(\beta-\gamma)$ where β is the angle between the reference orientation of the rotor and the local magnetic field and γ' the velocity of the shaft. The common assumption in resolvers is that the $R_R.i_R$ voltage is too low to be considered. However, in a design without yoke, a weak current design may be perturbed by external excitation, like wires carrying high-frequency signals; therefore this assumption may no longer be valid.

A resolver on a slow shaft will have no problem with the magnetic field, as V_B is proportional to γ': $V_{TR}=V_R$; again, V_{COS} and V_{SIN} are directly proportional to V_R and, therefore, to V_S. Usual processing still allows the computation of γ in that case.

If γ' is too high, then $V_{TR} = V_R+V_B$; it will then be necessary to compute the value of V_B. V_{TR} is equal in absolute value to $(V_{COS}{}^2+V_{SIN}{}^2)^{1/2}$; its sign may be determined thanks to $V_R-|V_{TR}|$ in order to compute the actual value of V_{TR}. The further part of the processing is standard, and again allows the computation of γ. Such a calculation also makes it possible to obtain the value of V_B, which may be used to get the value of the local transverse field and the value of the angle of the field with the resolver's reference plane. That makes the resolver a position, velocity and magnetic field sensor, which is perfect for the gain scheduling control strategy of a motor such as the one presented in 3.3.2.

Because there is no yoke, a multi-pole configuration cannot be used. The other problem linked with the brushless design is that the flux generated by the induction coils will also affect the voltage in the stator transformer coils. Using a brushed resolver design is preferred in order to avoid this mutual induction. Interference between the resolver and other devices may be attenuated by using a thin-earthed conductive housing, but its size should be carefully designed to reduce eddy current drag.

Therefore, a magnetic-compatible resolver with position, velocity and magnetic field sensing properties should be a two-pole resolver, which is well known in the state of the art, with minor modifications to the driver. The main difference is the absence of a yoke, which should result in different coil configuration and higher power

consumption. Its processing and construction may be achieved using state-of-the-art solutions, and as a result, it will not be tested in this study.

3.5. Logic and Wiring

3.5.1. Fighting induction

The effects of the magnetic field on the wires, particularly induction, will be a problem when dealing with small voltage components and sensors. The first tool to fight this induction is to use higher voltage because power consumption is not considered to be a major issue. A logic system of more than 10 V and even higher should present better behaviour than a 5 V- or 3.3 V-based one, provided the components that experience this voltage can withstand it. However, this solution only works for digital systems.

In order to fight induction, the system can be designed so that the total current through the cable feed through is zero. This is achieved by twisting together input and return lines, including ground, and putting them in a small dimension tube. In this condition, the induced voltage is actually the same on all the cables. Because the total current through the section of the umbilical cable is zero, it does not experience force from the magnetic field either.

Because the magnetic shielding of motors, resolvers, etc. does not operate in the environment, a high risk of mutual induction between the wires and these components persists. The cables in the umbilical cable will suffer as well. Sensitive lines should be shielded with grounded sheathed cables. The ground should be arranged in star configuration to avoid loops.

Induction through circuit loops should not be a problem considering the velocity of the device. While parked, the maximal field shift during shut down is 27 mT/s, as stated in section 3.1, or 27 mV/m², to be multiplied by the surface of the loop to get a rough value of the induced voltage. If a loop in the electronic circuit cannot stand this induced voltage, it should be placed horizontally in the parking position. This way, the flux variation through the surface offered by the printed circuit boards will be minimised as well as the risk of damaging the system. However, such low voltages should not have a critical influence on the operation of electronic circuits themselves. The question of the electronic components remains.

3.5.2. Environment effects on transistors

Previous studies in the state of the art have shown that few high-level electronic integrated circuits can sustain high radiation doses. Temperature is also an important parameter for electronics and an aggrieving factor for radiation effects. However, tests have shown transistor references that withstand doses as high as 10 MGy at high temperatures [3][51]. Si-Ge transistor developments offer good expectations in radiation hardening with temperature. But even if they are operating, their critical parameters,

such as current gain for bipolar transistors or threshold voltage for field-effect transistors, may suffer from great change.

Now, it is possible to redesign circuits by only using these transistors, as was done by SCK-CEN in [23][51]. This leads to pretty bulky systems; a simple operational amplifier made with small SMD transistors and components may be no smaller than 10 x 10 mm² in plan. Therefore, the designer should be careful to select circuits that use the smallest number of components possible, particularly transistors.

What is achievable and what is not in this environment is thus highly dependent on the place available for electronics in the robotic manipulator and on the effect a shift in the parameters of the transistor may have on the whole system. Additionally, any electronic circuit must be enclosed in leak-tight boxes.

However, a severe lack of information on the effect of high magnetic fields on transistors persists. Because it is a multi-port component, the Hall effect is an expected issue, particularly when dealing with large components. In the Large Hadron Collider's experiment chambers with high magnetic fields, particularly ATLAS and CMS, there are circuits that get close to the beam and thus must withstand a 1 or 2 T magnetic field. However, no analysis has been conducted on the effect of the field on the circuits, except on the components that are magnetic such as inductors and power transformers (replaced respectively by air-core coils and ceramic transformers) [7][15][28]. Therefore, the effect on transistors is expected to be minor at the stated values of field, if any, since the LHC experiments have begun successfully. However, even if the radiation there is considerable, integrated circuits can be used in the LHC, and, as stated before, the size of the components is a critical parameter when dealing with the Hall effect.

The lack of information on the subject leads to the consideration of in-field testing of an array of transistor references.

3.5.3. Available logic system designs

Considering the constraints stated previously in section 3.5.2, the circuits to be used are those that require the smallest number of components. This actually suggests solutions developed during the early times of transistors and electronics, when there were few integrated circuits. The concepts for designing internal circuits of present day chips will also help in designing the systems. Of course, the circuits should cope with transistors whose parameters may change with the total dose received.

For this reason, digital processing of data should be chosen over direct analogue processing. Logic gates are relatively simple to achieve using only transistors that operate in switching mode only. Digital data may also be reasonably easily transferred to the base in multiplexed form. Reference [8] provides an example of a simple multiplexing system made with a limited number of transistors. Analogue to digital conversion generates a space consuming circuit, as the circuit complexity gets higher with the number of bits; from the series of circuits given by [25], the servoconverter circuit looks the most promising in terms of space consumption and performance, as it

requires three gates: a comparator, a counter and a digital to analogue converter. Digital to analogue conversion may be carried out by resistor arrays.

When needed, there are actually a few analogue operations that may be achieved. For example, because a MOSFET may be considered in linear mode as a commanded resistor whose resistance is proportional to the gate voltage, it is possible to multiply two analogue signals using this feature. A full array of operations may be achieved on analogue signals, such as squaring, square rooting, summing, etc. The main issue with analogue operations is that the most common designs make extensive use of operational amplifiers and each of these components must be replaced with complete printed circuit boards that consume a significant amount of space. However, numerous circuits carry out the operations stated above without using any operational amplifier. Transistors that must operate in their linear range will also be quickly affected by radiation.

3.5.4.   Optical networks

Being amagnetic, optical networks seem to be a good alternative to standard electronic systems. They do not have to face any induction or force from the magnetic field. However, there is an effect on the polarization of light that goes through an optical fibre. If polarised light is used, the same method as for an electric cable must be used, namely twisting input and return lines to ensure that the total effect is negligible.

On the other hand, optical networks are unsuitable for power transmission. Radiation is also a hard constraint on these systems, on both the light-based sensors and the optical fibres. Reference [2] gives an array of possible use of light systems in a radiation environment. A large parameter shift occurs in light-based sensors such as fibre Bragg grating due to radiation. Even if this shift is not critical for operation, it is difficult to characterise as the parameter shift has a large variance. However, optical fibres hardened up to 10 MGy are available if chosen wisely.

3.6.   Magnetic field generator design

It has been established that a set of technologies needs further investigation to demonstrate experimentally their operability in a magnetic field. Indeed, the suggested modified DC motor's parameter change with the magnetic field is to be assessed. Furthermore, the transistor's operability in high magnetic fields should be assessed. In order to carry out these experiments, a magnetic field generator with adapted field configuration has been built.

The following sections are based on calculations made with Finite Elements Method Magnetics (FEMM), an open-source program that combines finite elements with Maxwell equations ((2-1), (2-2), (2-3), (2-4)) for computing the local magnetic field, given the configurations of coils, magnets and the material and dimensions of static parts. It is only suited to simulations in 2D.

3.6.1. Requirements

The final requirements for the generator are set by the testing requirements for the magnet-less DC motors. Indeed, for this experiment, the generated field is to be perpendicular to the shaft of the motor; the rotor to be used is Ø26 mm x 57 mm. Due to the problems with reduction gearings, the device should be therefore inserted in the active volume in a direction that is perpendicular to the local field, which allows in-line transmission of the tested rotor. The station will comply with the following requirements:

- Active volume with magnetic field: 40 x 80 x 100 mm^3 (Magnetic field should be along the smallest dimension, penetration along the largest dimension).
- The field may present spatial differences provided they are contained at the scale of mm. Typically, the field diffused by an iron yoke of cross-section 80 mm x 100 mm is acceptable.
- Tested device should be placed on positioning tables, with positioning accuracy less than 1 mm.
- The generator should withstand 3 consecutive minutes of use.
- Compliance with security requirements of the building hosting the experiment.

Considering the security issues that the use of a superconductive device station creates and the price of such a station, the generator coils will be made of copper. The power that will be lost in heating should be kept in the range of the available electric circuit – no more than what can be supplied by a 380 V / 64 A plug, which is 33.7 kW at most. Water cooling will not be used in order to avoid shorting the coil circuit in case of the failure of the wire insulator.

The best way to generate the magnetic field in the active volume is to have a high permeability magnetic circuit with the active volume being an air-gap in the circuit. However, high permeability materials – ferromagnetic materials – show saturation after a magnetic field flux density is reached; its relative permeability then reduces to 1. Because the field saturation value of a typical available ferromagnetic material such as low carbon steel 1038 is nearly 2 T, and because diffusion of the magnetic field in free air is important, generating more than 1.3 T in the active volume with this material is difficult – 1.3 T is the field measured between two parts of 1038 steel, 80 x 100 mm² in section, 40 mm away, magnetised at 2 T, according to simulations with FEMM. It already requires 1 MA/m across the 40 mm of the air-gap, achievable with 40 kA.turn. Generating another 1.3 T in the active volume requires generating 1.3 T in the entire air volume around the coils, requiring about 4 times this amount of magnetic field strength.

3.6.2. General layout of the magnetic field generator

The configuration of the field – a roughly constant field in a given direction – suggests a Helmholtz coil-like design with an iron yoke to concentrate the magnetic field strength across the air-gap. This leaves an acceptable space for the introduction of the device in a

direction perpendicular to the local field. In order to avoid perturbation due to gravity, the vertical direction is chosen as the penetration direction.
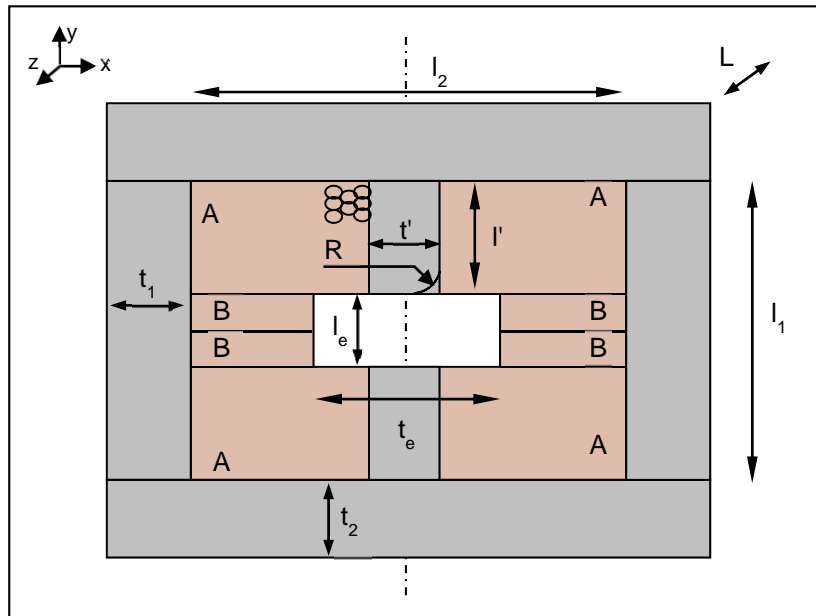

Fig. 3-12: General layout of the generator.
A are the main coils; B are optional coils. Signs show the direction of current flow.

A general layout of the generator is thus chosen. The layout will feature two coils, each mounted on an E-shaped ferromagnetic yoke made out of carbon steel 1038, with the active volume on the middle branch as pictured in Fig. 3-12. The two yokes are mounted on rails in order to split the generator in two. Fig. 3-13 and Fig. 3-14 show two possible ways of placing the coils while leaving the required space for penetration.

Some of the above values are linked to the dimensions of the active volume (the air-gap in the middle of the layout). As a result, t'=80 mm, L=100 mm and l_e=40 mm.

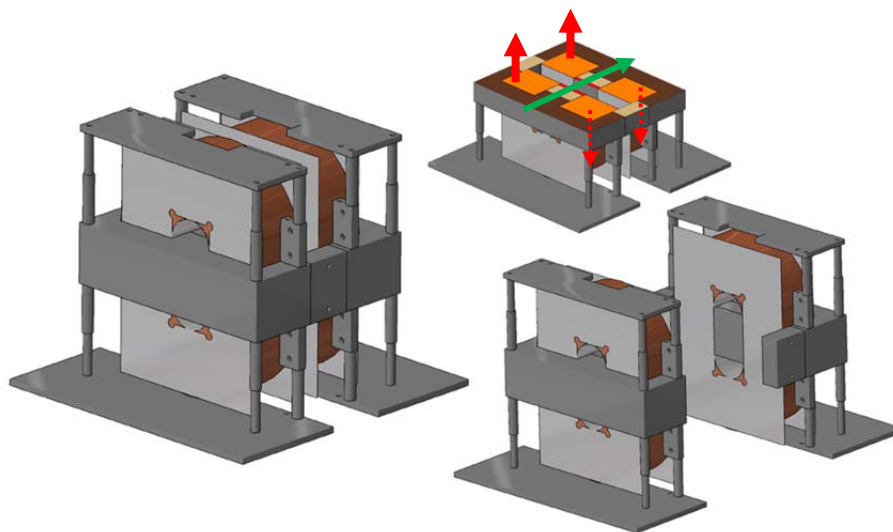**Fig. 3-13: Views of the generator with vertical A coils.**
On the cut view (top), red arrows show the circulation of current; the green arrow shows the direction of the magnetic field.
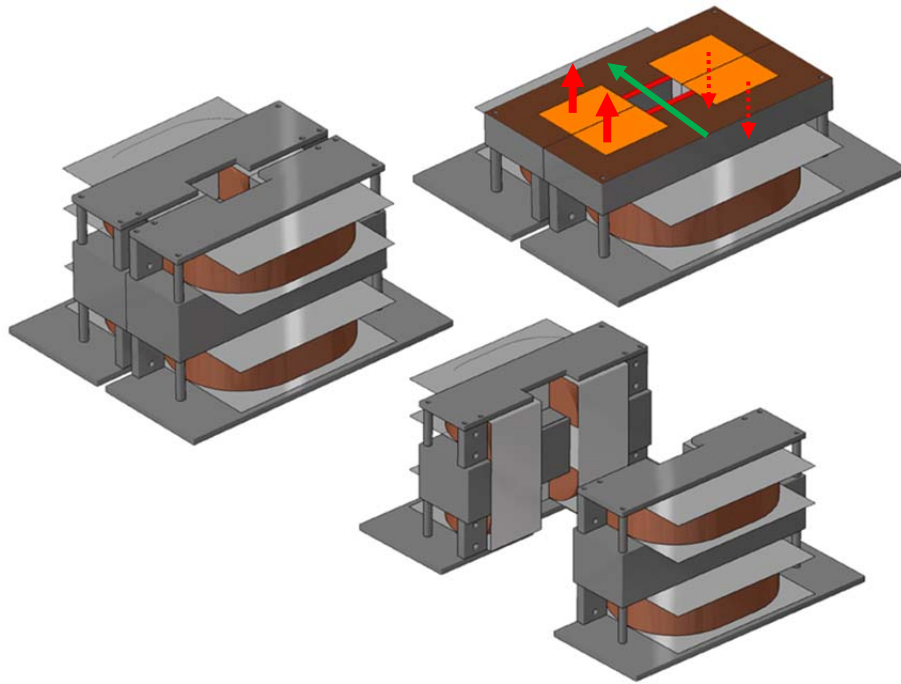
Fig. 3-14: Views of the generator with merged A and B coils.
On the cut view (top), red arrows show the circulation of current; the green arrow shows the direction of the magnetic field.

3.6.3. Power requirement

In order to choose the power source, it is necessary to evaluate the current consumed by the generator, which with the resistance of the cable will in turn suggest the power consumed by the generator.

Ampere's circuital law (2-4) allows evaluation of the number of Ampere-turns required from the coil to generate 1.3 T in the active volume, measuring 40 mm in length. In the first step, because the dimensions of the yoke are unknown, it will be considered with an infinite permeability. The symbols used below are according to the notations presented in Fig. 3-12; nI represents the amount of ampere-turns in the coil. The numerical value is given for the length of the air-gap l_e equal to 40 mm.

$$l_e \cdot (1.3\,T) = \mu_0 \cdot nI \;\rightarrow\; nI = 41400\,A.turn$$

The dimensions of the coil are determined by the type of cable that is wound to make the coil and the amount of current that can flow safely through it. These dimensions are necessary to determine the inner dimensions of the yoke.

The dimension of the cable is an important choice, as filling the space with cable will be less effective with a large diameter cable than with a smaller diameter cable. However, small cables allow less current to flow, which means more turns and therefore a longer wire length and higher resistance. Using a small cable will thus require a high voltage and low current, while larger cables will use a low voltage source supplying large currents. The specifications of two different high temperature cables are summarised below:

Supplier	Tyco Elec	Eland
Max temp (°C)	200	180
Copper section (mm²)	2.5	35
Wire diameter (mm)	2.83	10.8
Ω/km	8.2	0.565
Kg/km	30	420.8

Table 3-3: Specifications of two different cables for the coil.

The maximal intensity that the cable may support is given by the following calculation. Considering the generator has to be used for no more than 3 min, the heat generated in the cable by the current does not take less than 3 min to heat up the wire to the maximum temperature from 20°C, knowing the mass of copper involved and its heat capacity (385 $J.Kg^{-1}.K^{-1}$). Numerical application gives 34.0 A for the Tyco cable (16.3 A/mm²) and 505 A for the Eland cable (14.4 A/mm²). With the 41400 A.turn mentioned above, the required number of turns is 609 for the Tyco cable and 41 for the Eland cable. Considering that each cable fits into a hexagon that includes its diameter, the surface covered by the section of the coil may be estimated at 3845 mm² for the Tyco cable and 3770 mm² for the Eland cable.

The required length of cable is set by the number of turns to be wound in the coil, the way it is coiled and the dimensions of the core on which it sits. In this case, the core is a square 80 x 100 mm². The Tyco cable may be wound in an AB coil (Fig. 3-14) while the Eland cable, due to its stiffness, should be wound in a single A coil. In order to estimate the required length of cable, the coil volume will be computed. For the volume to be calculated, the dimension l' is necessary; it is set at 90 mm. This results in l_2 = 150 mm for the Tyco cable and 164 mm for the Eland cable.

$$V_{coilA} = l' \left(\pi \left(\frac{{l_2}^2 - t'^2}{4} \right) + (L + t')(l_2 - t') \right)$$

$$V_{coilAB} = \left(l' + \frac{l_e}{2} \right) \left(\pi \left(\frac{{l_2}^2 - t'^2}{4} \right) + (L + t')(l_2 - t') \right) + \frac{\pi}{2} (l_2 - t') \left(l' + \frac{l_e}{2} \right)^2 \quad \text{(3-7)}$$

In order to determine the length of wire, the coil's volume (4.10 dm^3 for the Tyco cable and 2.80 dm^3 for the Eland cable) is divided by the coil section and multiplied by the number of turns. This gives 649 m per coil using the Tyco cable and 57.4 m per coil with the Eland cable.

At this point in the design, the yoke's dimensions are set, and simulations using FEMM may be done to estimate how much Ampere-turns are consumed to magnetise it at 2 T. This value, around 22 kA.turn in both cases, is not negligible. Therefore, the method above must be reiterated, adding the Ampere-turns required for the yoke to the 41.4 kA.turn required for the air-gap. The computation converges with few iterations; at this point 28 kA.turns are consumed for the magnetisation of the yoke, and the dimensions of the coils are as follows:

Cable Coil type	Tyco Elec Type AB	Eland Type A
Coil turns	1025	69
Coil section (mm²)	6470	6340
l_2 (mm)	198	221
Total wire length (m)	2450	130
Voltage (V)	656	37.0
Heating power (kW)	22.3	18.70

Table 3-4: Coil data for the two cables considered.

The data given in Table 3-4 shows clearly the practical difference between using a small or a large cable for the generator. Using a small cable, the power source should be a 'low voltage' DC power source (120 VDC < U < 1000 VDC) while a large cable requires an 'extra-low voltage' DC power source (U < 50 VDC). They should be at the same level of power (around 20 kW). However, whilst low-voltage DC power sources in this range are scarce and expensive, extra-low voltage DC power sources in the 20 kW are fairly common because high power welding stations fit in this description. The level of voltage in the small cable also exceeds its limit, stated at 500 V. Additionally, considering the length of cable and the price, it appears that the large cable solution is more economical. As a result, the chosen solution uses the Eland cable.

### 3.6.4. Description of the generator built

The coil is powered by a 400 A MIG-MAG welding station that has been used previously at CEA-LIST and can generate 400 A at 30 V. The station is therefore slightly under-powered with regard to the specification given in the previous section.

The selected strand is the Eland cable described in the previous section, a high-temperature silicon-insulated wire of 35 mm² cross-section, with a thin insulation layer (insulation thickness 1.4 mm, outer diameter 10.8 mm) for compactness. It is rated up to 180°C. The cable should be 130 m long. The 54 kg of copper in the wire shall take about 4 min to heat up to 180°C with Joule heating of 30 V x 400 A = 12 kW when considering perfect thermal conduction in the wire and no external heat transfer.

The iron yoke is made of low-carbon steel. There is no lamination as the issued field should be constant. Two E-shaped parts 100 mm thick, 320 mm long and 320 mm wide have been machined and assembled to build the core. The coils are wound around the 80 mm wide central bar, and the active volume is situated in front of the middle of this central bar. This structure allows minimal spreading of the magnetic field outside the yoke. Magnetic field closure plates and an iron cage are set all around the coils.

The generator is built in two parts, each of which features an E-shape yoke and a 70-turns coil. This makes a total of 140 turns with 400 A – 56 kA.turn. Each individual coil is carried by a self-sustaining structure made with stainless steel sheets to make its manipulation and winding easier. The yoke is featured with different end-effectors; the

standard one is the flat one providing a 40 mm gap, but it can be replaced with other shapes that will result in different field shapes and values. For example, the prism-shaped end effector should allow a field at 1.5 T, with a higher lateral gradient.
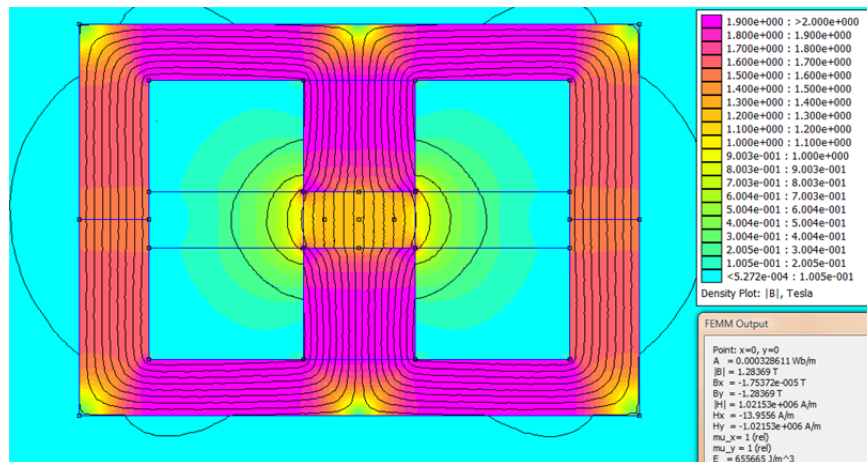
Fig. 3-15: Double E magnetic field generator with 56 kA.turn.
Centre point field is estimated at 1.28 T.

FEMM has been used to compute the field configuration depending on which yoke end effector is installed. Fig. 3-15 gives the field configuration for the flat end effector. Other field configurations with different end-effectors are given in Appendix D.

Fig. 3-16: Views of the constructed magnetic field generator.

The final layout of the generator is pictured in Fig. 3-16, with the power station on the left and the yoke and coils on the right and in the bottom pictures.

The positioning tables that carry the tested element are introduced in the active volume through the bottom of the generator. The position on the horizontal plane is set by two positioning tables with a precision of 20 µm; its vertical position is set by a stop end placed according to the test rig to be introduced. Fig. 3-17 shows the construction of the test rig for the magnet-less DC motor, featuring the tested rotor (in the square aluminium housing) and a standard motor used as a generator (refer to section 4.1 for more information).

Fig. 3-17: Views of the magnet-less DC motor test carrier.
The right figure shows it attached to the bottom of the generator; the rotor is in the active volume.

3.6.5. Characterisation

The field inside the active volume has been measured using a BELL gaussmeter 5180 equipped with a STD18-0404 transverse probe capable of measuring a field of up to 3 T with a 0.1% accuracy [67]. This thin probe (1 mm thick) features an effective area that measures Ø0.1 mm placed at the tip of the probe. The probe is placed in the field using the test rig carrier (Fig. 3-18), using the millimetre tables for positioning. It is inserted the same way as another test bench, pictured in Fig. 3-17. An Agilent 34910A data acquisition unit gathers the measurements from the probe and a 2000:1 current transformer on the generator coil wire simultaneously.
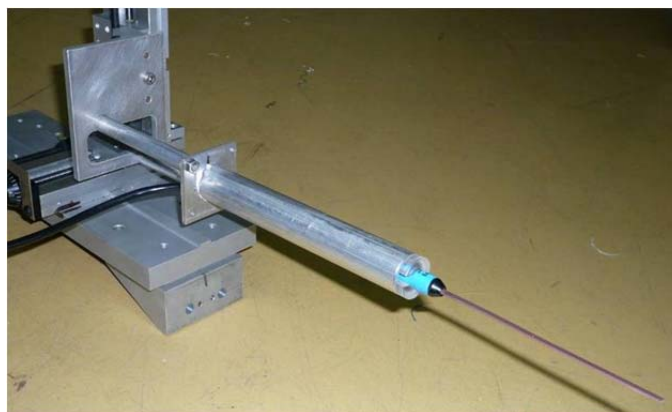

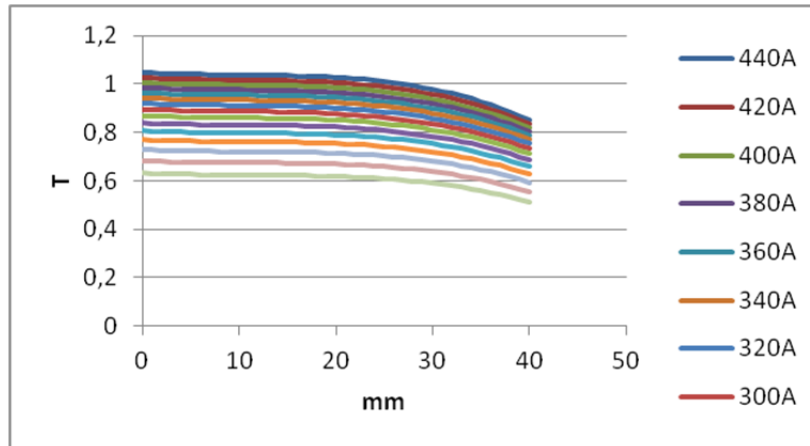**Fig. 3-18: Transverse probe mounted on carrier.**

Fig. 3-19: Measured magnetic field vs. position.
Probe position is X=0, Z=0. Y is expressed by the horizontal axis.

The first measurements at high current demonstrated a severe lack of field compared to simulations at high intensities; the field proved to be 1.00 T at 400 A using the flat end-effector, instead of 1.28 T as stated by finite elements analysis. Further testing showed that the yoke material magnetisation curve was different than the expected one from theory. Magnetic relative permeability at 0 T is fair (1000) but decreases fast with field strength. Saturation field in the material has been estimated from measurements at 1.50 T instead of 2 T. Using a magnetic-purposed material, like Hyperco cobalt iron, and avoiding severe machining like for the E-shaped yoke probably would have yielded better results, in addition to a much higher saturation field (2.34 T), but no such material was available in quantity at the time of the building of the generator. The field range obtained with the current yoke (0.61 to 1.05 T) is satisfactory to estimate the trends, which according to theory will be proportional up to high field values.

3.7. Contributions of the chapter

A set of magnetic-hardened technologies for structural design, actuation, sensing, and data transfer and processing have been described in this chapter. For active components – namely the actuators and the sensors – not only insensitive technologies were considered but also concepts that actively use the magnetic field to generate work or compute the position of the robotic manipulator. The developments related to this strategy may be considered as a major contribution of this study to the state of the art, as they show the possibility of using a high local magnetic field for actuation of a continuous rotation device, for 6D positioning of a complex system with many degrees of freedom and for adding to a resolver the possibility of measuring the local magnetic field in addition to the angular position and velocity of the shaft.

The devices discussed in this chapter that are not using the field for operation are state-of-the-art components. The present study checked the operability of these

technologies in the inspection environment of ITER and, if necessary, presented solutions that allowed them to operate properly or presented their expected limitations.

Design guidelines have been drawn for an electric motor relying on the local field that operates with standard parts from a DC brushed motor but at lower velocity and higher torque than the original. Specifically, a magnet-less motor with neither magnet nor ferromagnetic housing is 50% lighter than the original. This motor design proves to be interesting for long-reach robotic manipulator joints operated at low velocity and high torque and critical in terms of mass. It also appears from current experience in fusion diagnostics as the only way to generate continuous rotary movement in the given conditions.

An alternative where an electric motor is not only relying on the local magnetic field – and thus continues working when the field is off – has also been demonstrated to work both with and without the magnetic field and at different velocities and torques under two conditions: the motor's position should keep on the same torus radial plane whatever the position of the degrees of freedom of the robotic manipulator, and the structure should cope with the strong magnetisation force generated by the presence of the yoke and the magnet.

The possibility of using a local field measurement to compute the 6D absolute position of the robotic manipulator has also been investigated. This is an important asset for long-reach robotic manipulators, as their dimensions and payload cause important flexural deflection in the structure.

It has also been proved that featuring a tamed eddy current drag by using conductive parts that are carefully designed and placed in the robot will raise the damping factor of the structure's dynamics, which is a known issue of long-reach robotic manipulators.

These are the technological developments forming the core concepts and main contributions of this thesis. Such concepts may be used for robotics as well as other fields such as fusion diagnostics, where it is currently difficult to generate continuous rotation or have accurate positioning using sensors, or high field particle accelerators diagnostics should the need for a moving system arise.

Technologies that rely on the local field would of course be inoperative when the field is off, except for the solution using the standard DC motor. Experimental demonstration has been considered necessary for the magnet-less brushed DC motor and the operation of transistors with regard to the magnetic field's actual strength, which is the subject of the next chapter. In order to carry out these experimentation, a magnetic field generator was specifically built for this study. This field generator was described in this chapter. Powered by a 12 kW MIG-MAG welding station, it is able of generating up to 1 T in an active volume of 40 x 80 x 100 mm^3 for 4 consecutive minutes.

4. RESULTS: CONCEPTUAL EVALUATION OF A DEMONSTRATION ROBOTIC MANIPULATOR

The current chapter presents how the technologies developed in chapter 3 can be used in a long-reach inspection robotic manipulator carrying a metrology probe for ITER within the specifications for the IVVS. The objective is to have a direct view of at least 99% of the first wall while offering a correct positioning precision for metrology via measurement or a model. The target precision is the precision required from the IVVS, which is 0.5 mm. Both CAD model based kinematic 3D simulation and dynamic model simulations are carried out in order to estimate the capabilities of the proposed design for a long-reach inspection robotic manipulator for inspection task of the ITER first wall.

The first section gives the results of the experiments of the magnet-less DC motor and the transistors in the magnetic field of the generator. A second section then presents the design requirements on the inspection robotic manipulator carrying the probe. The dimensions of the robot have been set in order to comply with toroidal trajectories that allow complete viewing of an 80 degrees section of the ITER first wall centred on the deployment point of the robot. These robot link lengths and other dimensions had to be determined by analysing reachability and mobility with respect to the first wall geometry. Then a selection among the different technologies developed in chapter 3 is made for choosing actuators and sensors of the robotic manipulator and the way its structure is built. A weight draft is estimated from these choices in order to evaluate the actuation forces, required for dimensioning the motors, along with the operation scheme proposal.

In last section the suggested inspection robotic manipulator design is verified with a dynamic simulation program in order to present its performance and potential. All the inspection tasks carried out using this inspection robotic manipulator will occur when the toroidal magnetic field is on so that technologies that require the local field to be operative can be used.

4.1. Magnetic field tests

4.1.1. Magnet-less DC motor

A device (Fig. 4-2) was built according to the recommendations given in section 3.3.2. The rotor and brushes have been taken from a Faulhaber 3257 coreless brushed DC motor [68]. All the motors from this manufacturer are coreless motors, as is necessary

to build a magnet-less motor. This means that the rotor is a self-sustaining coil and contains no iron. The 3257 motor has been chosen as it is used in the AIA [18], and therefore complies with temperature constraints.

Fig. 4-1: Views of the original Faulhaber 3257 brushed DC motor.
Top to bottom, left to right: original assembly viewed from the side of the shaft, the rotor with the self-sustaining coil, the brush holder and the stator with the magnet.
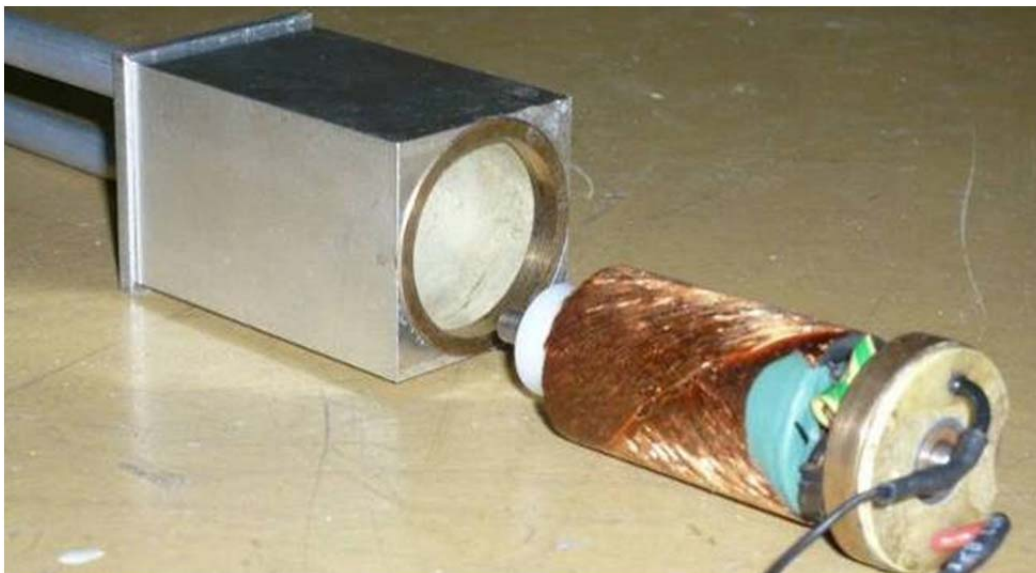

Fig. 4-2: Magnet-less DC motor construction.

In order to transform the motor into a magnet-less motor, a different brush holder has been built by retro-engineering the existing brush holder and adding a copper bushing to it for free rotation around the axis of the shaft. The standard steel ball bearings have been replaced by plastic and glass ball bearings and impregnated bronze

bushings for this test rig. The stator has been made from standard-grade aluminium alloy and, of course, does not house any magnet.

The ferromagnetic compass has not been implemented. Indeed, a large ferromagnetic part in such a small volume with a 1 T field would bypass a large portion of the magnetic flux, resulting in a large decrease of field at the rotor. However, this phenomenon will not occur in ITER as the ferromagnetic part will be saturated; its effect on the field value will be localised in its close vicinity. The effect on the magnetic field value at the rotor, if any, will be limited.

The rotor's shaft is connected to a load by a set of couplings and long plastic shafts. The load itself is a standard 3257 motor, placed outside the field underneath the generator, whose torque constant has been measured at stall using a torque sensor. Voltages across the load pins, the rotor pins and across the charge resistors in the load and rotor circuit are measured using the data acquisition unit. Generator coil current is also measured.

As a reminder, a brushed DC motor is, according to theory, characterised by a simple proportionality ratio that links voltage and velocity on the one hand and current and torque on the other hand. This ratio is named the torque constant in the literature, K_T, although it is not *stricto sensu* a constant when operating in a non-uniform magnetic field, as shown in section 3.3.2. The equation (3-4) should apply (with U being the electromotive force, ω the angular velocity, Cm the motor torque, I the motor current and nS the surface of the loop equivalent to the rotor construction).

Fig. 4-3: Views of the magnet-less DC motor test carrier.

The test rig (Fig. 4-3) is placed so that the rotor's axis is at the centre point of the air-gap and centred in the active volume with respect to the z direction. The torque constant of the device is then measured in-field in two ways. First, the load is powered at different voltages, resulting in different velocities, with the rotor circuit open. At each of these velocities, the voltage across the rotor is measured, giving a first estimation of the torque constant. The friction of the bench at the supplied field is given by the load circuit current, then the rotor is connected to the power supply at a constant voltage and the load to a variable resistor with high power rating. Each load resistance value

matches a different torque value. The total torque to rotor current ratio gives another estimation of the torque constant. These measurements are carried out at different field values, given by the generator coil current.
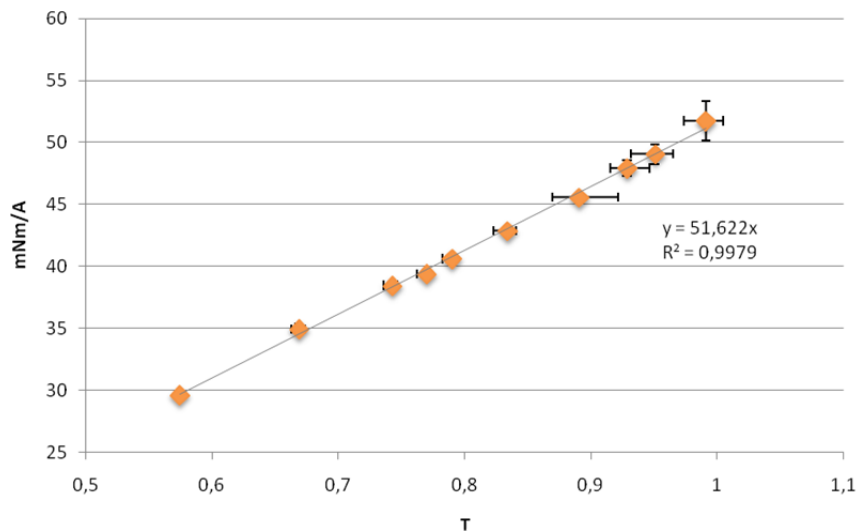

Fig. 4-4: Measured torque constant against magnetic field.

The torque constant to magnetic field ratio has been measured at 51.62 mNm/A/T or 51620 mm² (Fig. 4-4). The correlation factor of the measurements to pure proportionality has been calculated at 0.9979. The torque constant of the 3257 is specified at 37.7 mNm/A, which corresponds to 0.73 T according to the measured ratio. This value matches the estimation of the peak field inside the motor's air-gap by finite element analysis using FEMM (Fig. 4-5).
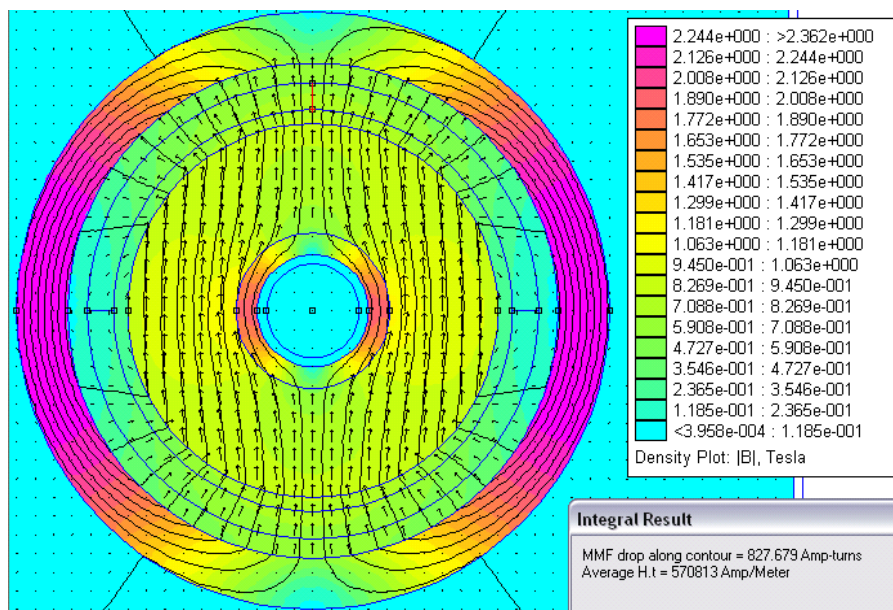

Fig. 4-5: Finite elements analysis of a 3257.
Mean field along red line (top vertical in the air-gap) is 571 kA/m, that is, 0.72 T.

Table 4-1 summarises the principal characteristics of a standard 3257 and of the modified motor.

Motor	**3257** [68]	3257 rotor + B	3257 rotor + B Same velocity
Rated voltage (V)	24	24	33.3*(B/1 T)
Power rating (W)	83	83	115*(B/1 T)
Rated current (A)	2.3	2.3	2.3
Torque constant (mNm/A)	37.7	51.62*(B/1 T)	51.62*(B/1 T)
Max. cont. torque (mNm)	70	95.9*(B/1 T)	95.9*(B/1 T)
No-load velocity (rpm)	5900	4300/(B/1 T)	5900

Table 4-1: Motor characteristics: standard and in-field.

From the compiled data, it is possible to confirm the expectations stated in section 3.3.2. Indeed, because the torque constant increases proportionally to the local field at the same voltage of 24 V, the motor operates at an increased torque for a reduced velocity, with a 'magnetic reduction ratio'. If the motor is supplied with a higher voltage to match its original no-load velocity (266 V here when the motor is in an 8 T field) then the motor may be rated at a higher power, 909 W in the specified case. However, this state of operation is effective if, and only if, the insulation of the coil's wire withstands this voltage; in addition, it has not been tested in the frame of this study. Considering the interest in a device with such a high power to volume and weight ratio, further study on this topic is advised.

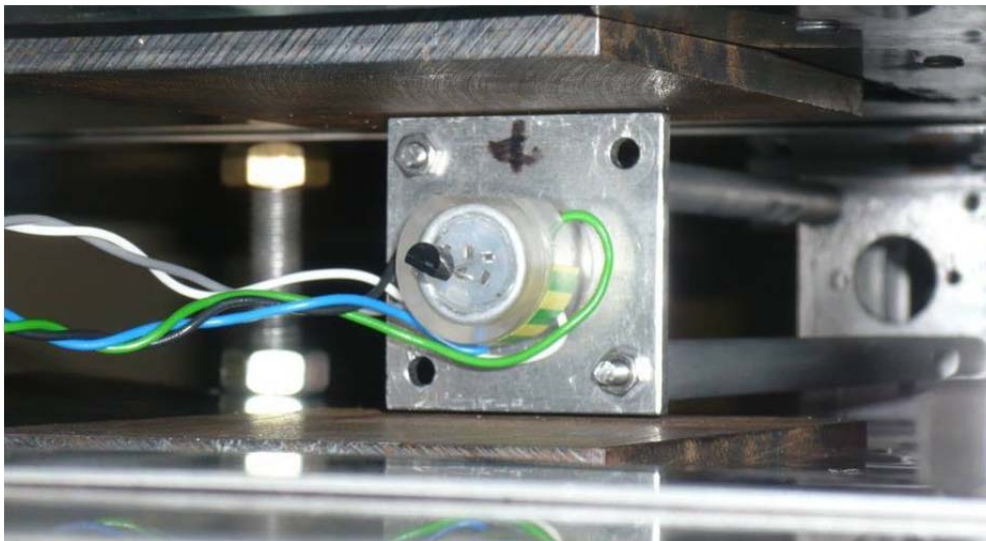### 4.1.2. In-field transistor operation

Fig. 4-6: Test rig with a sample transistor in the active volume.

A test rig was used to place the tested transistors in the magnetic field; it features the same carrier as the previous experiments (Fig. 4-6). Tested transistors are then

monitored as a function of their properties in a simple circuit at different field values, and at different orientations, as it appeared the effects of the magnetic field might be influenced by the orientation of the chip.

The first observation was that transistors with casing referenced TO-18 were not compatible with a magnetic field, as their hull, which is made to attenuate the electromagnetic perturbations, actually features a ferromagnetic behaviour that would result in high forces from the field gradient. Therefore, the use of such transistors is not recommended.

An array of transistors has been tested on the test rig. They feature different types of casings, properties and rated currents (summarised in Table 4-2) in order to check whether those parameters have a role in the influence of the magnetic field on the transistor operation.

Reference	Technology	Casing	Rated current	Remarks
BC547	NPN	TO-92	200 mA	
BC557	PNP	TO-92	200 mA	
BD908	PNP	TO-220	5 A	
IRF540	MOSFET	TO-220	5 A	
BFP640	NPN	SOT-343 (SMD)	100 mA	Used in a 10 MGy VSCEL driver [22]
J177	JFET P	TO-92	200 mA	Rated at 10 MGy in [3]

Table 4-2: Tested transistors' properties.

The transistors have all been tested in a common-drain (or common-emitter for bipolar transistors) amplifier circuit. The resistors in the circuit are adapted to each transistor in order not to exceed the maximum current ratings. The following parameters are then monitored through an oscilloscope or computed for different values of magnetic field and different positions inside this field: drain-to-source (collector-emitter) and gate-to-source (base-emitter) voltage at saturation, bandwidth, gate-to-source threshold voltage and gate current for field-effect transistors and current gain for bipolar transistors.

Every device at all the available fields and in all orientations yielded a similar result; the magnetic field has no visible effect on the operation of transistors. The given example illustrates the voltage drops on a BC547B transistor in common emitter circuit (Fig. 4-7). It appears to be due to the small size of the actual chips, as the casings are designed for heat dissipation and are therefore much larger than the chip they actually house. The expected behaviour, if any, should be proportional to the magnetic field. The transistors are therefore expected to operate at fields as high as 8 T and probably even higher.
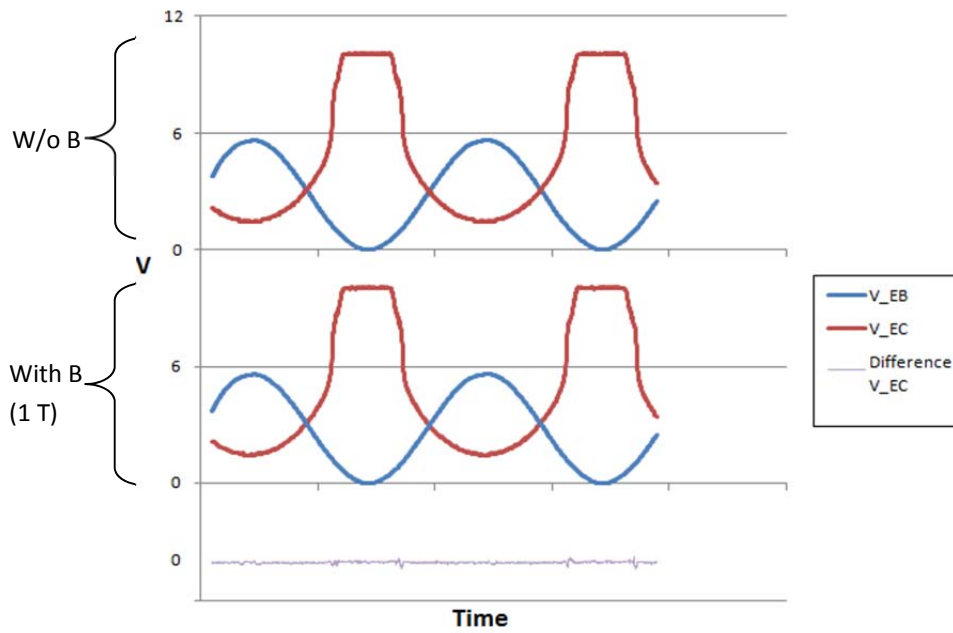
**Fig. 4-7: Collector to Emitter voltages of BC547B transistor with and without B
in a common emitter circuit, with a sinusoidal voltage drop between Base and Emitter.
Lower curve shows the difference between the two red curves at the same scale.**

4.2. Demonstrator design dimensions

The robotic manipulator design constraint is to be able to deploy tits payload, an IVVS probe designed as per ENEA design, so that it can view a wide portion of the first wall of the vacuum vessel. The kinematical layout of the robotic manipulator is chosen from previous experience from AIA and PAC, presented in sections 2.2.1 and 2.2.2 : the details of the kinematics, the associated kinematical model, flexibility model (due to its large range to outer diameter ratio) and control scheme (Fig. 4-8) are detailed in Appendix A.

A set of trajectories based on the limitations of the ENEA probe design will be determined in order for the probe to be able to view almost all of the first wall. The number of segments, the link dimensions inside the segment (coined L_{us}, L_{ds}, L_{tube}) and the stroke of the degrees of freedom of each segment (q_p and q_y) will be set in order for the robotic manipulator to be able to follow these trajectories. These dimensions do not take into account actuation or sensing methods, as they will be set in place in section 4.3 in function of evaluations of the weight of the system and the forces from the magnetic field.
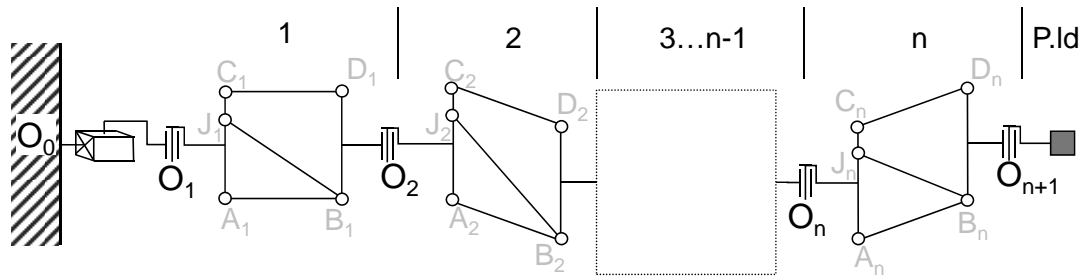
Fig. 4-8: AIA and PAC kinematics architecture.
This is the architecture chosen for the robotic manipulator demonstrator design.

4.2.1. Payload constraints

The technology that ENEA chose for the IVVS probe leads to limitations on the incidence angle between the line of sight and the local normal line, and on the distance between the probe reference point and the scanned area. Section 2.1.3 did provide more detailed specifications of the ENEA IVVS prototype. As a reminder, the actual maximum incidence angle between the laser beam issued by the prism and the viewed surface is 70 deg [30], with performance on metrology lower than the ITER requirements (0.5 mm [58]) for higher incidence angles; the lowest viewing distance is 1 m on the current design [30], but ENEA suggested improvements on the design for two focus areas, between 0.5 m and 2 m and between 2 m and 10 m [59]. These limitations shall condition the path that the probe must follow for a complete view of the wall. In addition, the probe prism pans at 360 deg/s, and should make measurements every millimetre of the first wall.
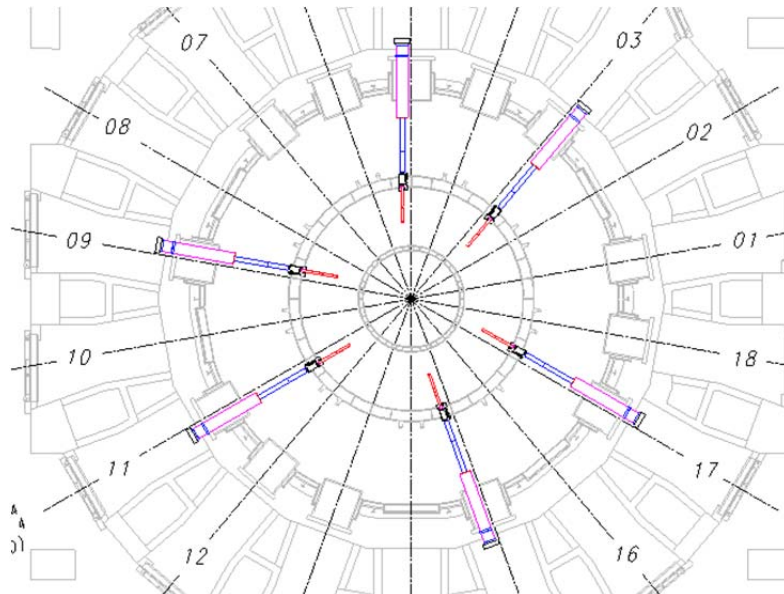

Fig. 4-9: Ports allocated for the deployment of the IVVS.

The available ports for deployment are the ones for the IVVS (ports number 03, 05, 09, 11, 15, and 17, which means a port every 40 deg, then 80 deg, then 40 deg, etc. as per Fig. 4-9). The entrance point of the robotic manipulator is where the divertor and the

blanket regions meet, on the outer wall, with a 6 deg slope. The actual ENEA IVVS design has a rectangular section 150 mm wide by 160 mm high. The robotic manipulator should fit within this section.

The payload has been fitted to the weight of the actual IVVS design at 22 kg. The drawing point where the laser beams exits from the probe is taken from the actual design of the IVVS as well, 700 mm away from the probe vertical joint.

4.2.2. Desired IVVS probe path

For initial analyses of desired IVVS probe path, the first wall is considered to be a perfect revolved shape. The best way to define the trajectory of the probe is therefore by choosing the best points of the torus section for the probe to be placed. As a result, the desired trajectory should be the circles going through these points constructed by their revolution around the torus axis.

When considering the baseline design of the section of the ITER first wall, there are 3 points of interest on the radial plane. A sweeping at each of these 3 points allows computation of an image of almost the full section. When covering these points, there is actually a small section of wall that cannot be viewed at the junction between the divertor and the blanket regions, both on the outer wall and the inner wall. 99.1% of the section is geometrically covered by the view from these points, which includes 100% of the plasma facing components surface.

In Fig. 4-10, point 1 is the intersection of two tangents of the divertor surfaces. Point 2 is the intersection of the insertion axis and the outer divertor tangent. Point 3 is placed 6.5 m away from the top blankets so that the incidence angle on the top blankets of the inner vertical wall is less than 22 deg. At these positions, the remaining 0.89% of the section that cannot be seen is the inside of the joining sections between the blankets and the divertor. These sections cannot actually be seen because they are shadowed by other portions of the first wall or at too high incidence angles.

The deployment port configuration is given by the IVVS Design Description Document [58]. The deployment axis is 6 deg from the vertical towards the central axis.

The image of the same 99.1% of the first wall can therefore be obtained by moving the probe along three horizontal circles centred on the torus axis crossing these 3 points of interest (Fig. 4-10). These will be the preferred paths of the probe for the design of the robotic manipulator. This 99.1% is a maximal reachable area; the probe should be placed exactly at the points considered to achieve this performance.

The probe should travel by 1 mm for every tilt turn on the prism. In the ENEA design for the IVVS, the probe prism is turning at a tilt velocity of 1 turn/s, the trajectory velocity should therefore be 1 mm/s.
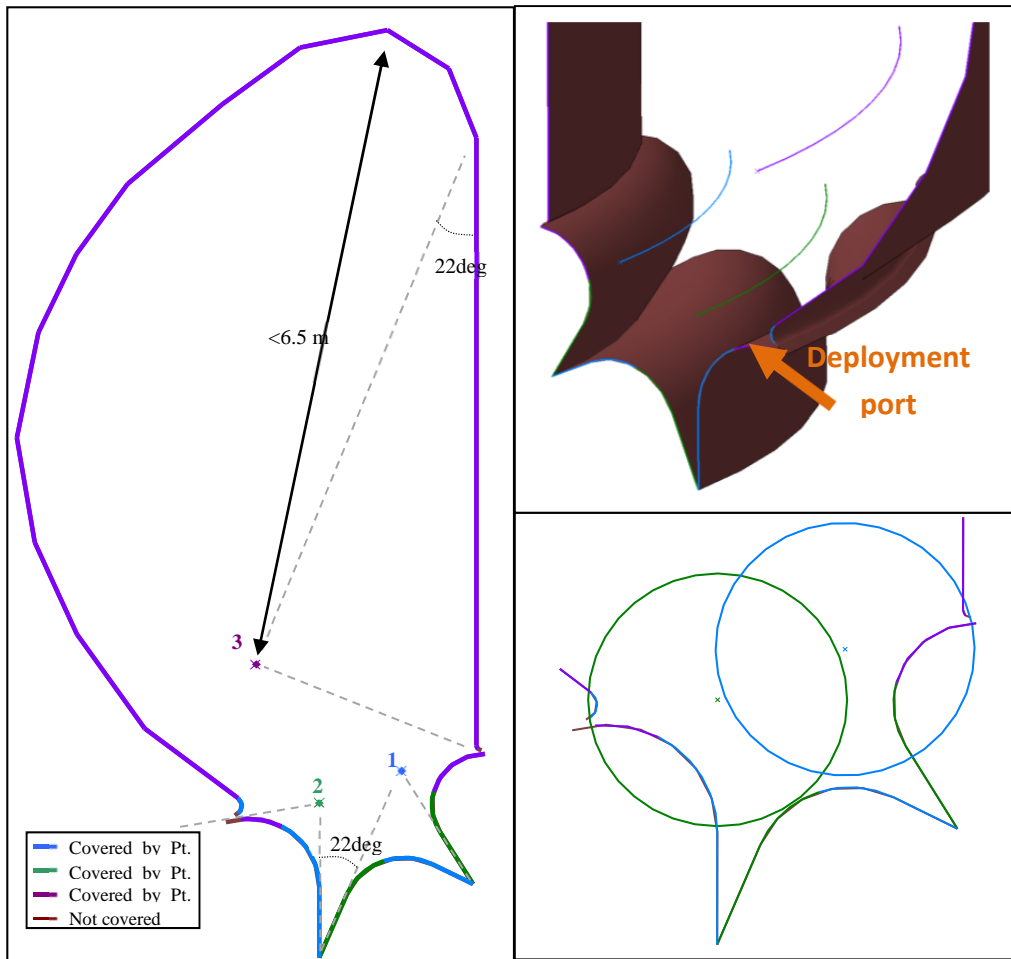
Fig. 4-10: Vacuum vessel inspection points and their construction lines.
Left: The full first wall section; colour codes identify which point is used to see the section.
Top right: The three circles issued from the three points of interest in the vacuum vessel.
Bottom right: Close-up on the divertor region, with circles giving the minimum distance of 0.5 m.

4.2.3. Kinematics

The architecture of the robotic manipulator is chosen from the layout of the AIA ([18], section 2.2.1) for the high mobility and compactness it allows. Appendix A provides details on this architecture. The number of segments, their lengths and their strokes have been determined in order to comply with the requirements of the inspection scheme previously presented. The actuators will be linear actuators, placed in the same configurations as in AIA and PAC, using cables for force transmission.

Fig. 4-11 provides the reference frame of the base, $(x_{dep}, y_{dep}, z_{dep})$, along with the main frame of each segment and the probe. This is the starting point for designing the robotic manipulator as it is presented in Appendix A. x_{dep} is set along the deployment direction as required by the IVVS Design Description Document [58], z_{dep} is the vector in the toroidal plane that is perpendicular to x_{dep} pointing upwards, and y_{dep} the resulting orthogonal vector to complete the frame. The segments of the robot are numbered from 3 down to 1, from the base to the payload.
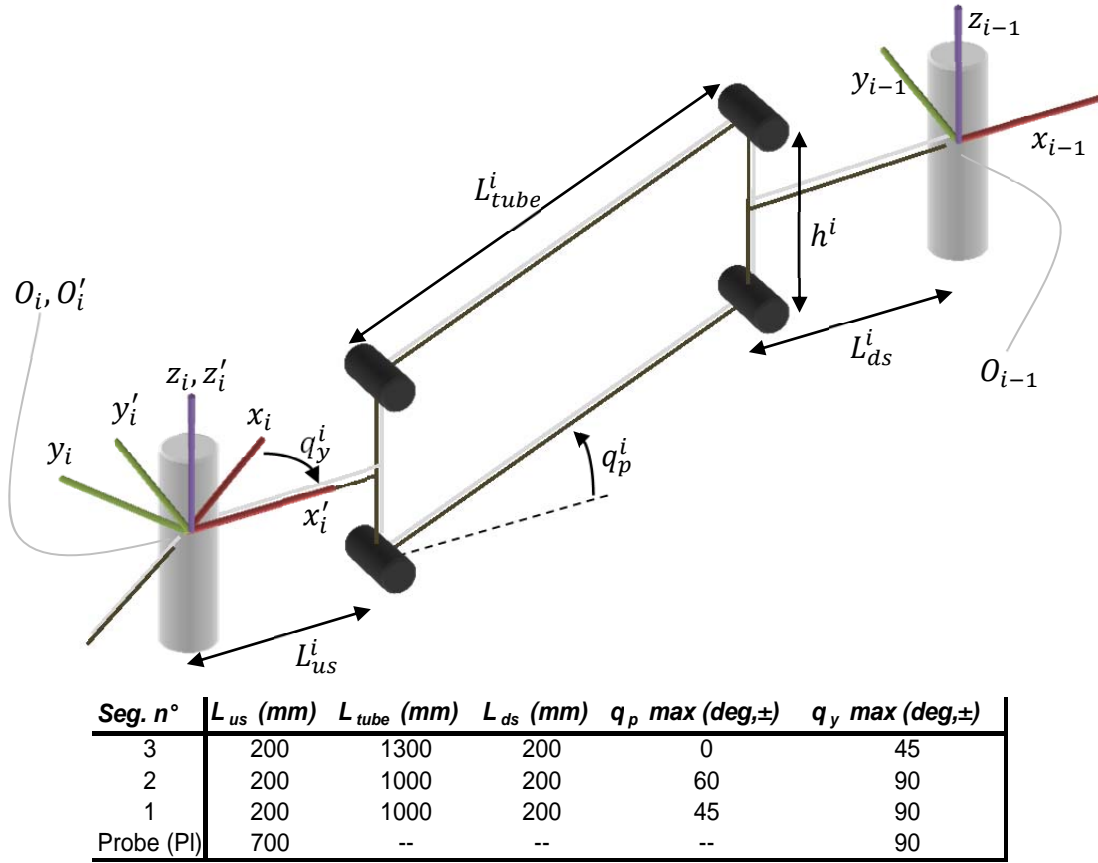
Seg. n°	L_us (mm)	L_tube (mm)	L_ds (mm)	q_p max (deg,±)	q_y max (deg,±)
3	200	1300	200	0	45
2	200	1000	200	60	90
1	200	1000	200	45	90
Probe (Pl)	700	--	--	--	90

Table 4-3: Suggested lengths and strokes.
Probe length is given between the yaw axis and the probe drawing point.

Table 4-3 gives the lengths and strokes for the above design. q_y and q_p are actuated parameters for each segment, except for segment 3 in which pitch is fixed. Adding the rack and pinion deploying mechanism to the robotic manipulator base, the resulting design has 7 degrees of freedom. In addition, the IVVS probe has pan and tilt degrees of freedom. With a total reach of 4 m and specified strokes for the actuated joints, the reference trajectories detailed in Fig. 4-10 can be followed. The goal was to keep the number of segments to minimum to avoid accumulating positioning errors and limit the actuation torques.

Considering the values chosen for the robot segment parameters, the following equations (4-1) taken from Appendix A give the transition matrix T_i^{i-1} that can be used in order to get the $(x_{i-1}, y_{i\_1}, z_{i-1})$ coordinate system in function of the (x_i, y_i, z_i) system, starting from i=3 with (x_3, y_3, z_3) system until i=0 with the (x_{Pl}, y_{Pl}, z_{Pl}) system, describing the position of the probe.

$$T_i^{i-1} = \begin{bmatrix} cy^i & -sy^i & 0 & cy^i(L_{us}^i + L_{ds}^i + L_{tube}^i \cdot cp^i) \\ sy^i & cy^i & 0 & sy^i(L_{us}^i + L_{ds}^i + L_{tube}^i \cdot cp^i) \\ 0 & 0 & 1 & L_{tube}^i \cdot sp^i \\ 0 & 0 & 0 & 1 \end{bmatrix}, \begin{cases} cy^i = \cos(q_y^i) \\ sy^i = \sin(q_y^i) \\ cp^i = \cos(q_p^i) \\ sp^i = \sin(q_p^i) \end{cases} \quad (4\text{-}1)$$

The (x_3, y_3, z_3) coordinate system is obtained as a translation of the $(x_{dep}, y_{dep}, z_{dep})$ coordinate system along x_{dep} as per the prismatic degree of freedom for deployment, which value is given by q$_{rack}$. The q$_{rack}$ origin corresponds to when the yaw joint of segment 3 is free of moving on the full stroke inside the vacuum vessel, free of any collision.
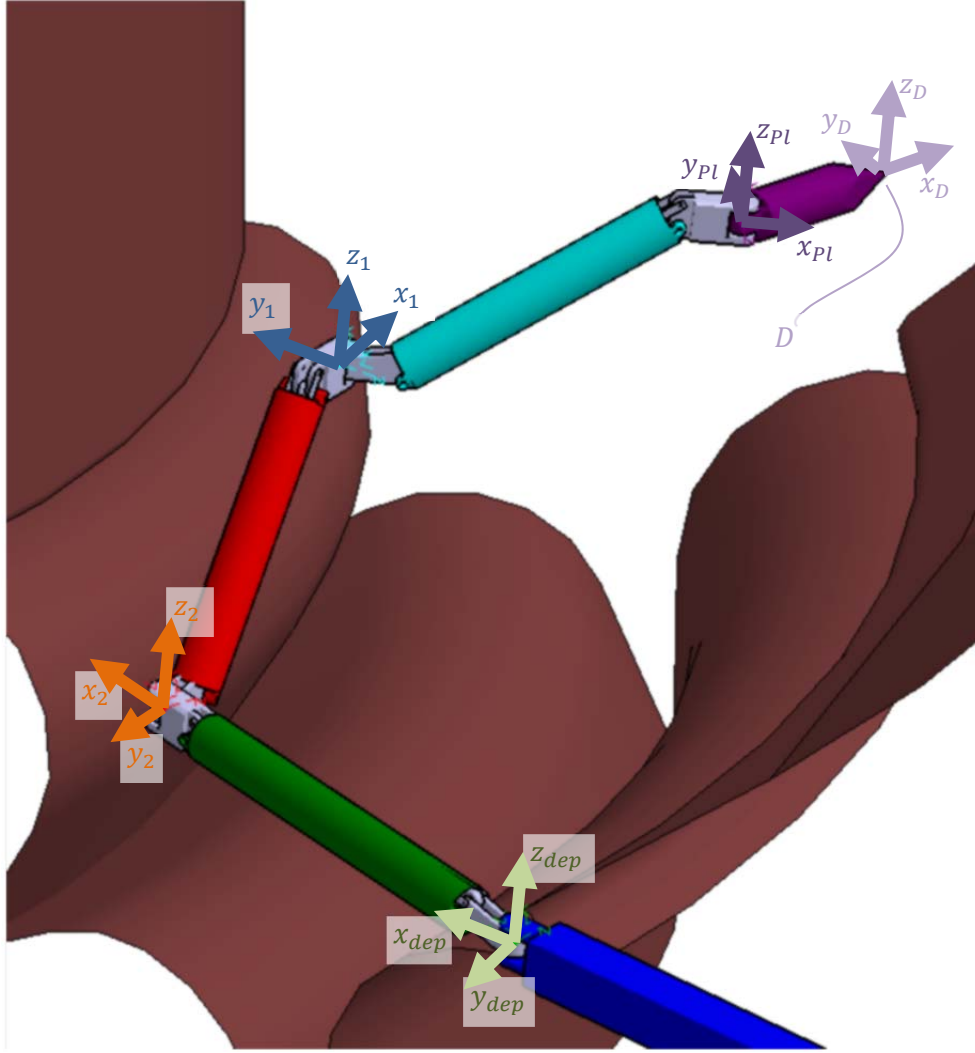

Fig. 4-11: Reference frames of the demonstrator with the probe at its end.
(x_3, y_3, z_3) frame is coincident with (x_{dep}, y_{dep}, z_{dep}): the robot is in fully deployed configuration.

The deployer degree of freedom can be defined with the following transfer matrix between the base frame (x_D, y_D, z_D) and the segment 3 frame:

$$\mathrm{T}^3_{dep} = \begin{bmatrix} 1 & 0 & 0 & q_{rack} \\ 0 & 1 & 0 & 0 \\ 0 & 0 & 1 & 0 \\ 0 & 0 & 0 & 1 \end{bmatrix} \tag{4-2}$$

Finally, the position of the drawing point D and the attached coordinate system (x_D, y_D, z_D) can be found using the last transfer matrix T^D_{Pl} from the reference frame of segment 1 to the reference frame of the payload:

$$T_{Pl}^D = \begin{bmatrix} cy^{Pl} & -sy^{Pl} & 0 & L_{us}^{Pl} \\ sy^{Pl} & cy^{Pl} & 0 & 0 \\ 0 & 0 & 1 & 0 \\ 0 & 0 & 0 & 1 \end{bmatrix}, \begin{cases} cy^{Pl} = \cos(q_y^{Pl}) \\ sy^{Pl} = \sin(q_y^{Pl}) \end{cases} \tag{4-3}$$

Given these equations (4-2) and (4-3), it is possible to get the position of any O_n point of the robotic manipulator or D through the multiplication of T_i^{i-1}:

$$O_n = (T_{dep}^3 \cdot \prod_{i=3}^n T_i^{i-1}) \cdot \begin{bmatrix} 0 \\ 0 \\ 0 \\ 1 \end{bmatrix} \quad ; \quad D = (T_{dep}^3 \cdot \prod_{i=3}^0 T_i^{i-1} \cdot T_{Pl}^D) \cdot \begin{bmatrix} 0 \\ 0 \\ 0 \\ 1 \end{bmatrix} \tag{4-4}$$

Point D, at the drawing point of the probe, is the point of interest which position must be set by the robotic manipulator. It will be referred to as the end-effector point from now on, its position is described by equation (4-4). The mathematical analysis may however be brought further in order to describe the drawing of the laser by the probe. This will allow to bring forward the limitations of the design, which will constraint the trajectories of the end-effector point, and therefore of the robotic manipulator.

The IVVS prototype by ENEA is a prism fixed on a tilt / pan mechanism in order to direct the incoming laser beam on the desired direction. The reflection of the laser beam on the surface of the first wall is used to make metrology and give an image of the inside of the vacuum vessel. In the latter (D, x_D, y_D, z_D) reference frame, the laser beam drawn by the probe can be pictured by a vector $\overrightarrow{Beam}$ which coordinates are given by equation (4-5), where q_{tilt} and q_{pan} represent the tilt and pan angles:

$$\overrightarrow{Beam} = \begin{bmatrix} \cos(q_{tilt}) \\ \sin(q_{pan}) \cdot \sin(q_{tilt}) \\ -\cos(q_{pan}) \cdot \sin(q_{tilt}) \\ 1 \end{bmatrix} \tag{4-5}$$

The ENEA prototype is made so that q_{pan} is not limited in angle, but q_{tilt} is limited to [-80 deg; +80 deg]. This limitation leads to a dead angle, materialized by a cone measuring 20 deg in aperture, which apex is situated at the end-effector point D, revolving around $-x_D$. In this dead angle, no measurement can be made by the probe.

4.2.4. Probe path description

The following figures (Fig. 4-12, Fig. 4-13, Fig. 4-14) show the extreme points that can be reached on the 3 circles matching the 3 points of interest with the lengths and strokes given in Table 4-3. The probe is not drawn strictly accordingly to the ENEA design in the figures; its drawing point is situated at the apex of the pictured cone. The yellow cone shows the 20 deg blind cone of the device described in the previous section. The first wall section shown on the pictures is 45 deg wide, starting at the deployment point.
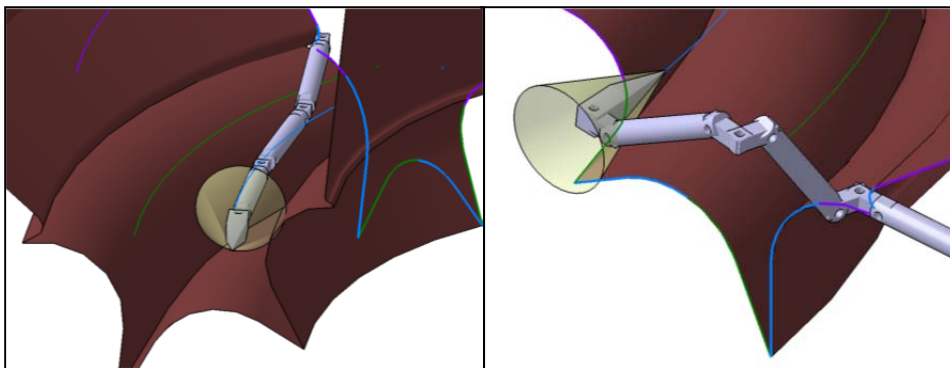
Fig. 4-12: Circle 1 extreme positions.
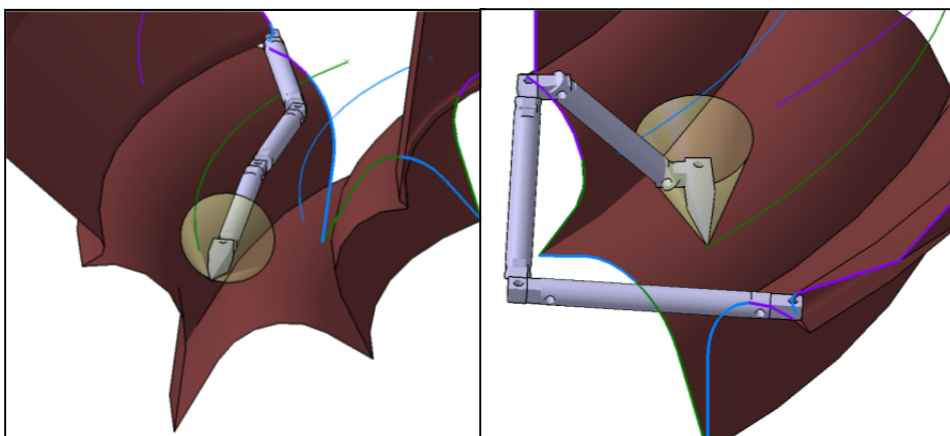**Point reached on the left picture is at the toroidal angle 53.9 deg.**

Fig. 4-13: Circle 2 extreme positions.
Point reached on the left picture is at the toroidal angle 50.7 deg.
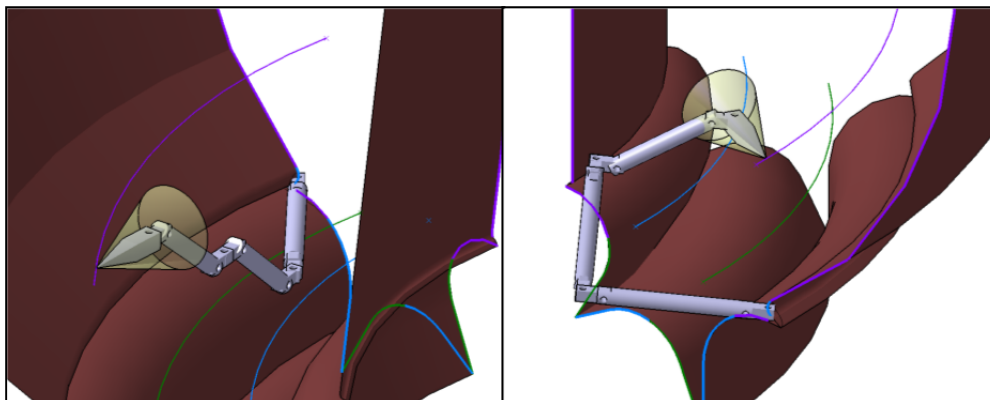

Fig. 4-14: Circle 3 extreme positions.
Point reached on the left picture is at the toroidal angle 42.5 deg.
Point reached on the right picture is at the toroidal angle 1.4 deg.

The inverse kinematics, giving the values of the angles so that the probe point follows the given trajectory, has been carried out using the Kinematics module of the CATIA software. The determination of the trajectory has therefore not been determined explicitly, but implicitly from the conceptual CAD design. The point of the probe has been fixed to the trajectory and moved at a constant speed. Because there are 7 degrees

of freedom in the robotic manipulator in total (including the linear rack q_{rack}), 4 additional joints are set: q_{y3}, q_{y2}, q_{p2} and q_{rack}. The values of the remaining degrees of freedom are given by the software from key frames set by the user, between which the positions are extrapolated linearly in 40 frames.

Once the maximal joint velocities are determined, the amount of time needed for the inspection can be evaluated by changing the time shift between the frames.

Fig. 4-15 gives the angular positions that represent the trajectories shown in Fig. 4-12, Fig. 4-13 and Fig. 4-14 in the same order, built using the procedure described above. A change in configuration is necessary in two trajectories, passing the payload over the point $q_{yPl}=0$ deg. This will undoubtedly lead to a play compensation phenomenon that will result in a loss of accuracy, which will not, however, be taken into account in the following study and the simulation.
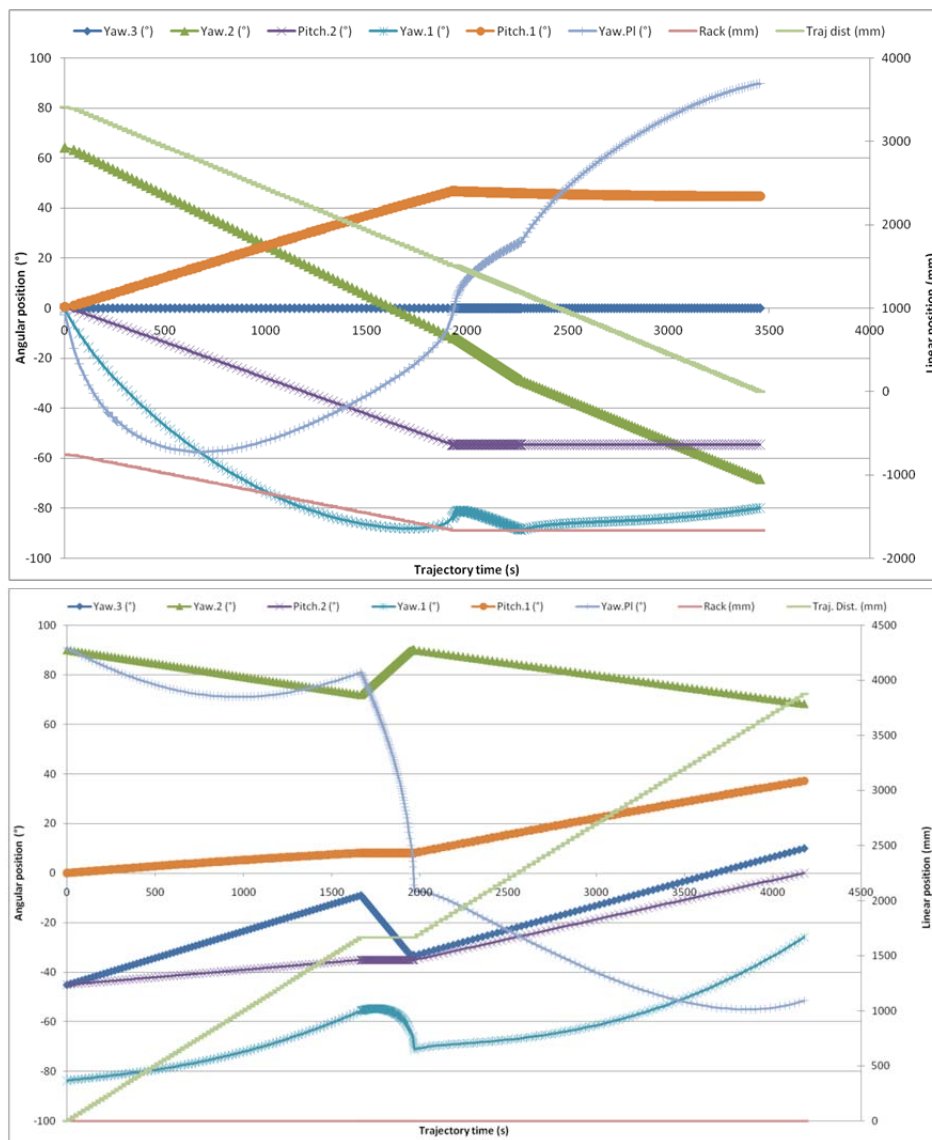

Fig. 4-15: Joint paths for scenarios described in Fig. 4-12, Fig. 4-13 and Fig. 4-14.
Joint angles refer to the left vertical axis; joint distance and distance run on the trajectory refer to the right vertical axis. Time is expressed in seconds, taking data given in Table 4-6 into account and limiting the velocity along the path to 1 mm/s.

Data points marked with light green on the graphs in Fig. 4-15 are showing the evolution of the probe along the trajectory, which leads to the limitations on the other curves. There are intervals of time where the light green data points stay constant: this is when the robotic manipulator reconfigures its degrees of freedom staying at the same position. During this reconfiguration, the probe does not make any measurement, and the joint velocities are not limited anymore. Actually, the limitations which set the time needed for reconfiguration are taken from the maximum joint velocities expressed later in Table 4-6. With these values, the limiting factor is the yaw velocity of the payload.

The joint paths described in Fig. 4-15 show that one hour is required for each of the three inspection paths. Linear velocity along the trajectory velocity, set at maximum 1 mm/s, is the limiting velocity of the system. However, this time estimation does not take into account that the probe prism does not have to turn one full turn each millimetre: in the case of both divertor inspections, as can be seen on Fig. 4-10, the probe prism should turn by 90 deg each millimetre, which speeds up the inspection time by a factor of 4. For the blankets, inspection time can be divided by two as the prism has to turn by 180 deg. Time required for inspections using the specified method are described in Table 4-4.

Inspection	Time required
Divertor	
40 deg section, inner divertor	30 min
40 deg section, outer divertor	30 min
20 deg section, inner divertor	15 min
20 deg section, outer divertor	15 min
Divertor – complete inspection	**60 min**
Blanket	
40 deg section	40 min
40 deg section – without inspection	15 min
20 deg section	20 min
20 deg section – without inspection	<10 min
Blanket – complete inspection	**<90 min**

Table 4-4: Inspection time estimation based on trajectory planning.

4.3. Component choices for demonstrator

Once the dimensions of the robot are set, it is now possible to determine the materials chosen for the robotic manipulator structure and then from experience from the AIA and PAC design to decide which materials will be used in which parts, what actuation means will have to be used and the electronics to be fitted in the robotic manipulator. Once this is set, it will be possible to go on with the weight draft of the robot and evaluation of torques required from the actuators.

4.3.1. Structural design

In order to limit the magnetisation forces, titanium alloy Ti-6-4 will be extensively used in long-reach inspection robotic manipulator structural elements. Stainless steel should not be used for massive parts, even though its high stiffness makes it excellent for critical structural parts. However, stainless steel can be used for thin sealed boxes and small components for which high strength material is compulsory, such as gears or bearings, and when no low-susceptibility material alternative is available.

4.3.2. Actuation and sensor designs

In this section, actuator and sensor designs for the proposed 7 degrees of freedom long-reach inspection robotic manipulator are presented and discussed. Fig. 4-16 shows conceptual design of proposed inspection robotic manipulator with the joint actuator installation positions and the constraints on their position in the robot.
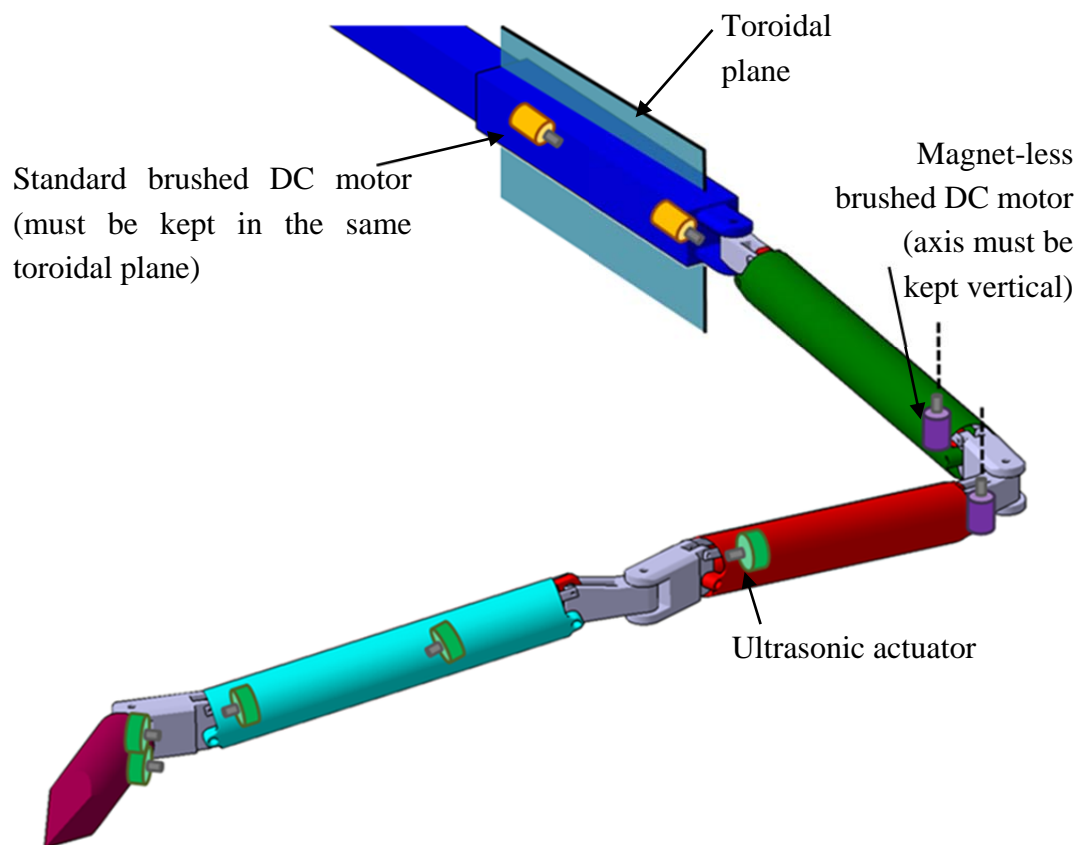

Fig. 4-16: Schematic drawing explaining the positions of the actuators in the robot.
Yellow actuators are standard brushed DC motors; they can be placed in any position as long as it is in the toroidal plane, pictured on the drawing. Purple actuators are magnetless motors, which should be kept with their axle vertical at all times, shown in dotted line on the drawing. Green actuators are ultrasonic motors, which can be placed in any orientation.

The actuator for the linear deployment movement at the base will be a standard brushed DC motor (yellow in Fig. 4-16), allowing simple deployment of the IVVS

probe. Another standard DC motor for driving joint q_{y3} will be placed in the parts on the linear joint, before the yaw joint itself. As standard brushed DC motors moving on the same toroidal plane, they can be operated as long as they are placed accordingly to the local field and motor's magnet direction as explained in the first part of section 3.3.2. These can operate both with and without the magnetic field.

Actuators for joints q_{y2} and q_{p2} are magnet-less DC motors, in purple in Fig. 4-16. The actuator for q_{y2} will be placed inside the tube of segment 3. The actuator for q_{p2} will be placed in the upstream clevis of segment 2.

Joints q_{y1}, q_{p1} and q_{yPl} will be actuated using UHV and magnetic compatible ultrasonic motors (pictured in green in Fig. 4-16), just like the IVVS probe inner joints. As amagnetic devices, they can be placed in any position and orientation inside the robotic manipulator.

This actuator configuration allows using the robot along the current baseline specified for the IVVS deployer because q_{y3} and q_{p1} can be actuated even without a magnetic field.

Considering the total number of actuators required and the space available for the umbilical cable, the solution using the magnet-less DC motor is chosen for actuators requiring high power. These motors' shafts should be kept vertical in all possible combinations of positions of the degrees of freedom. This is why motors for q_{y2} and q_{p2}, requiring the most power, have to be placed in clevis area or in the segment 3 tube, as it is not actuated, and therefore stays in the same orientation. Near the probe head, less space is available in the clevis to place magnet-less motor actuators and their gearings; therefore ultrasonic rotary piezomotors should be used here. Previous designs have proved that 10 W motor power is enough to move these joints at velocities in the range of tens of mrad/s.

Each joint will feature a resolver, turning at the same velocity as the motor. This allows resolvers to be used as magnetic field sensors to control the motors via gain scheduling, as well as position and velocity sensors. In addition, there will be an optical encoder with deported light source and sensor at the joint axle for ensuring high resolution positioning. The encoder resolution will be set according to past experience at CEA-LIST; 12bit will be used to describe the full pitch angle range (4096 values for 120 deg of maximum stroke) and 14bit for the yaw angle ranges (16384 values for 180 deg of stroke).

Each segment will also feature a 3D Hall sensor measuring the local magnetic field with high enough accuracy to compute the absolute position of the IVVS probe. Indeed, in order to achieve 0.5 mm accuracy positioning for the probe, and the field being the inverse of the square of the distance, the precision of the magnetic field sensor should be 0.6 mT, or 15 bits for a maximum measured field of 8 T.

4.3.3. Electronic processing and data transfer

Data processing inside the vacuum vessel will be limited to what is strictly necessary, typically fast loops for resolvers and ultrasonic motors, pre-amplification and the

multiplexing system. Considering the level of radiation, analogue to digital conversion will have to be carried out as close to the sensors as possible, using servoconverters [25] implemented with discrete SMD or TO-92 field-effect transistors. It is necessary to have one converter per analogue sensor embedded in the robotic manipulator. A common line multiplexer [8] with 8 common conductors will be used to transfer data to and from the electronics base placed at the safe side of the torus hall. As a result, the transferred signals in both directions will be 8-bit signals. Therefore, a signal that needs more than 8 bits for correct transcription will require two multiplexer frames.

Optical fibres will also be necessary to receive data from the encoders.

4.4.   Robot segment weight drafts and actuation torques

Now the actuators, materials, sensors and electronics are chosen, a fairly precise weight draft of the robotic manipulator may be determined in order to evaluate the actuation torques of each degree of freedom. This will allow making an estimation of the reduction ratio required for each degree of freedom on the one hand and the current required for the actuators, in particular the magnet-less actuators, on the other hand. With these values, it will be possible also to make recommendations on the design of the IVVS probe in order to reduce the force it will undergo inside the magnetic field.

The three segments experience different loads and, therefore, have different designs. For example, the parallelogram in segment 3 is not actuated, but the length of the parallelogram diagonal should be set by a rod. On the other hand, the parallelogram in segment 3 will have to transmit a negative torque, which would lead to a traction force on the tube and a large compression force on the rods, possibly leading to buckling. Therefore, segment 3 will feature a double parallelogram installed in parallel in order to keep the tube in compression whatever the head torque value is. The other segments will have a single parallelogram, although the rod of segment 2 will be dimensioned to face the compression force it should be able to manage without buckling.

Previous experience has shown that, in order to reduce the deflection at the end of the robotic manipulator, segments next to the base should preferably feature parts with higher stiffness, while head segments should have a light structure that undergoes smaller forces from gravity. Tube and rod stiffness in traction and compression are the critical factors. Considering the magnetic field forces the robot undergoes, this translates into avoiding stainless steel in head segments at all costs. On the other hand, elements with high conductivity placed in the design to increase the damping factor of the assembly should be placed at the head of the robotic manipulator for maximum effect but will translate into higher loads on the base segments actuators during movements. However, testing of magnetic field damping effects is out of scope of this thesis; no conductive part will intentionally be designed into the system in order to raise the damping factor.

The weight draft summed up in Table 4-5 has been carried out for a credible design of the robotic manipulator, supporting the forces with sufficient stiffness. Clevis masses are computed from experience from previous long-reach robotic manipulator programs, taking into account the material used and the forces. Tubes are dealt with taking into account thicknesses of different values (5 mm in segment 3, 1 mm in segments 2 and 1), these values being once again adapted from what has been designed in previous programs. Rod dimensions have been, again, adapted from previous experience (15 mm, 10 mm and 5 mm in segments 3, 2, 1 respectively).

	Segmt. 3	Segmt. 2	Segmt. 1	Probe (PI)	
Upstream	4,28	4,28	4,28	22	kg
suppl.	0	1,5	0	1	kg
TOTAL	**4,28**	**5,78**	**5,78**	**22**	**kg**
mag. force	0,60	2,70	2,70	6,16	kgf
Rods	6,13	0,70	0,11	--	kg
TOTAL	**6,13**	**0,70**	**0,11**	**--**	**kg**
mag. force	0,86	0,10	0,02	--	kgf
Tube	14,08	2,22	2,22	--	kg
suppl.	1,5	1,5	2,5	--	kg
TOTAL	**15,58**	**2,22**	**2,22**	**--**	**kg**
mag. force	4,07	0,31	0,31	--	kgf
Downstream	4,28	4,28	4,28	--	kg
suppl.	0	0	0	--	kg
TOTAL	**4,28**	**5,78**	**6,78**	**--**	**kg**
mag. force	0,60	2,70	4,10	--	kgf
Yaw torque	974,8	494,4	211,5	28,7	Nm
Pitch torque	*inactive*	628,2	424,4	--	Nm

Table 4-5: Weight draft and actuation torques of the suggested design.

In Table 4-5, clevises' masses are computed utilizing the experience from previous long-reach robotic manipulator programs. Structural parts are all manufactured in titanium alloy, allowing a margin of 5% maximum of AISI 316L stainless steel by mass. This margin is left for small elements requiring high strength – such as spindles for bearings – or accurate positioning; however, since the main part of the weight will come from the structural pats, all of them in Ti-6-4 titanium alloy as stated before, the portion in mass remains low. This portion of mass in stainless steel will allow computing the magnetization force on each segment, since this force is proportional to mass in each material.

Some weight tagged as supplementary is considered for allocating weight for actuators, sensors and electronics. For each segment, the amount of supplementary mass required has been evaluated, based on the number of actuators to carry, and their position in the segment. Sensors and electronics by themselves are low on weight; on the other hand, actuators parts – shafts and gearings in particular – will have to be made of titanium alloy. On the other hand, these elements have to be encapsulated inside tight boxes which are preferably manufactured of stainless steel. As a result, taking into

account that stainless steel is twice as heavy as titanium in volume, the percentage of AISI 316L stainless steel in mass has been set at 50%.

Actuators using a magnetless motor have been accounted for taking into account a total mass of 1.5 kg each. As a result, as can be seen in Table 4-5, tube in segment 3 is fitted with 1.5 kg of complementary mass, as this element carries the actuator for q_{y2}. Upstream clevis of segment 2 features another 1.5 kg of complementary mass for accounting the actuator for q_{p2}. On the other hand, another 1.5 kg has been accounted for ultrasonic motors moving qy1 and qp1, while the ones required for qPl and the two payload DOFs have been considered to weigh 2.5 kg in total. The reason for different weights in these two cases is the higher power ratings required for pitch and yaw actuation of segment 1.

Magnetization forces shown in Table 4-5 are computed by using the maximal values for magnetization force computed in section 3.2.1 at the highest field value in the ITER tokamak: 2.8 kgf/kg for AISI 316L stainless steel and 15.7 x 10^{-3} kgf/kg for Ti-6-4 titanium alloy.

Total gravity and magnetization torques at each segment origin is computed. Magnetization force being always horizontal, these two torques are orthogonal. Because of the slope of insertion (6 deg, or 10% slope), pitch torque accounts 99% of the gravity torque and 10% of the magnetization torque, while yaw torque accounts 99% of the magnetization torque and 10% of the pitch torque.
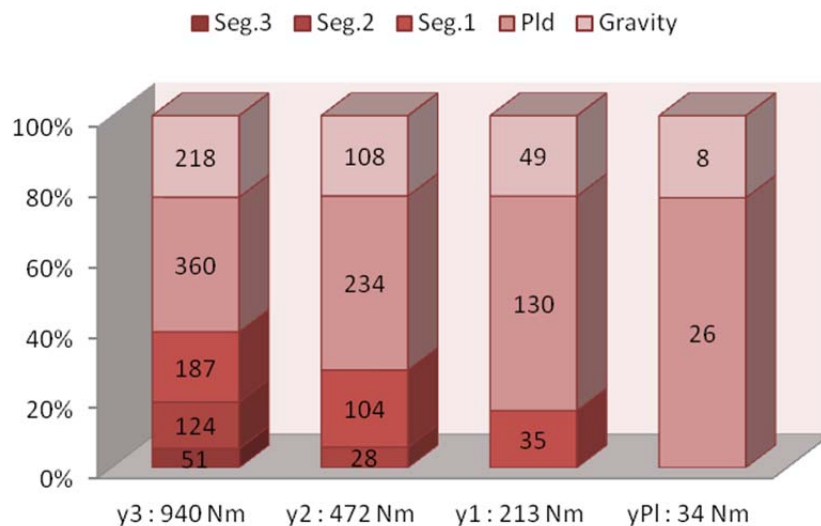

Fig. 4-17: Proportion of torque due to each segment and gravity on the yaw joints.

The current ENEA IVVS probe design is made entirely of AISI 316L stainless steel; this has not been taken into account here. The mass ratio of AISI 316L in the probe considered here is 10%, with the rest in Ti-6-4. Fig. 6-9 presents the amount of yaw torque on each segment and the payload due to magnetization force with regard to the total torque; it shows that even with a mere 10% of the probe being made out of stainless steel, 360 Nm out of 940 Nm on q_{y1} is due to the payload and is due in a large

part to the magnetisation force. A probe fully made out of AISI 316L stainless steel would undergo up to 62 kg of magnetization force, requiring 3 kNm on q_{y1}, 2 kNm on q_{y2}, 1 kNm on q_{y3} and 200 Nm on q_{yPl}. In its current design, it appears as though the ENEA proposal for the IVVS probe along its current design fully made of stainless steel may not be carried by a dextrous robotic manipulator. It would require much more powerful actuators, magnetless motors even for q_{y1}, q_{p1} and q_{yPl}, and a larger structure than the expected Ø150 mm outer diameter.

Once the torques that the motors must provide have been set, the reduction ratios can be detailed. The motors are assembled on a reduction mechanism to create an electrical jack, pulling with a cantilever arm on the joint's axis. The cantilever's length is set at 50 mm for the yaw axes and at the parallelogram height (75 mm) for pitch axes. The jack is made with a roller screw with 1 mm pitch, sitting on a thrust bearing generating friction torque proportional to the actuator thrust. The remaining reduction ratio described in Table 4-6 is set in order to overcome the maximum continuous torque of the motor tested in section 4.1 at 4 T. This torque includes the friction torque at the level of the motor, which is set at 90 mNm to allow the mechanisms to be irreversible without brake. The total efficiency of the reduction mechanism (not taking into account the additional friction at the level of the motor) is estimated at 50%.

Y_3		Y_2		P_2 (@0 deg)		P_2 (@60 deg)	
16	:1	10	:1	10	:1	10	:1
10.9	mrad/s @8 T	17.5	mrad/s @8 T	17.5	mrad/s @8 T	23.3	mrad/s @8 T
0.82	A @8 T	0.72	A @8 T	0.86	A @8 T	1.08	A @8 T
21.9	mrad/s @4 T	35.0	mrad/s @4 T	35.0	mrad/s @4 T	46.7	mrad/s @4 T
1.65	A @4 T	1.44	A @4 T	1.72	A @4 T	2.15	A @4 T

Table 4-6: Reduction ratios, max. joint velocities and max. torque currents.

Eddy current dragging torques on the joints at these angular velocities with the considered materials are in the range of Nm for yaw joints and even lower for pitch joints, against actuation forces of several 100 Nm. Eddy current drag will not be taken into account; only the magnetisation force will be computed.

Additionally, reduction ratios for the mechanisms of Y_1, P_1 and Y_{Pl} are not detailed, as they are actuated by ultrasonic motors that allow precise positioning. Moreover, their actual effect on the positioning accuracy is negligible due to the fact that they are close to the probe. Therefore, these joints will be presumed to be perfect – that is, they should exactly follow the position command they are given.

4.5. Simulation

In order to validate the design of the demonstrator robotic manipulator, a simulation of the system will be done using the available tools developed for the AIA and the PAC. The tracking errors of the probe on the different trajectories set in section 4.2.2 will be determined, considering a control scheme similar to the one already in place for PAC

and AIA, slightly modified to take into account the influence of the magnetic field on the brushed motors.

The simulation program that is used in the current section is described in Appendix B. Its structure has been taken from the simulation of a long-reach robotic manipulator previously developed at CEA-LIST, based on Newton-Euler equations computed on a fixed time step basis. Its operation is not to be considered a part of the contributions of this study.

The direct kinematic model that has been used was the model developed for the PAC and AIA, explained in Appendix A, including virtual joints in order to simulate the flexibility of the robot. This model is based on an iterative algorithm. The model has been adapted to the needs of the simulation program and improved to include parameters that take into account forces generated in all directions on any part of the robotic manipulator, particularly the magnetic forces. The model of the PAC and AIA has proved to converge with practice towards the local potential well drawn by gravity, but the theoretical proof of convergence has not been established. This theoretical proof has not been conducted in this study because the mathematical structure of the magnetic field is similar to that of gravity; it creates one single potential well, which is close to the first position at which the model is computed. The algorithm is still expected to converge at the correct position in the case of a robot operating in a magnetic field.

The control scheme used for this robotic manipulator is the same that has been successfully used in the PAC and AIA, a Proportional-Derivate current controller, featuring thresholds for the compensation of dry friction in the mechanisms. This controller is described in Appendix B, section 7). The controller is based on the difference between the measured joint angle and the angle computed from the trajectory at the present time for error computation.

The programming of the interface between the two models had to be executed specifically for this study, but this should not be considered a major contribution to the state of the art. The kinematic model is used in the simulation program in order to compute the positions of the main elements of the robotic manipulator. This allows computing the actuation torques and the actual inertias on every degree of freedom. The simulation program then makes the calculation of friction in the actuation chain using a Coulomb model for each of the reduction mechanism or bearing of the actuation chain.

Once the parameters of the simulation have been set, each of the joints are first tested independently to ensure that the friction forces are dissipative and that the PD control is correctly tuned for a mean field value of 6 T. The compensation of dry friction is set at the actuation block parameters, which are presumed to have been measured or estimated.

The chosen trajectory for the demonstration is the outer divertor trajectory, shown in green in Fig. 4-10 (the trajectory is described in Fig. 4-13).
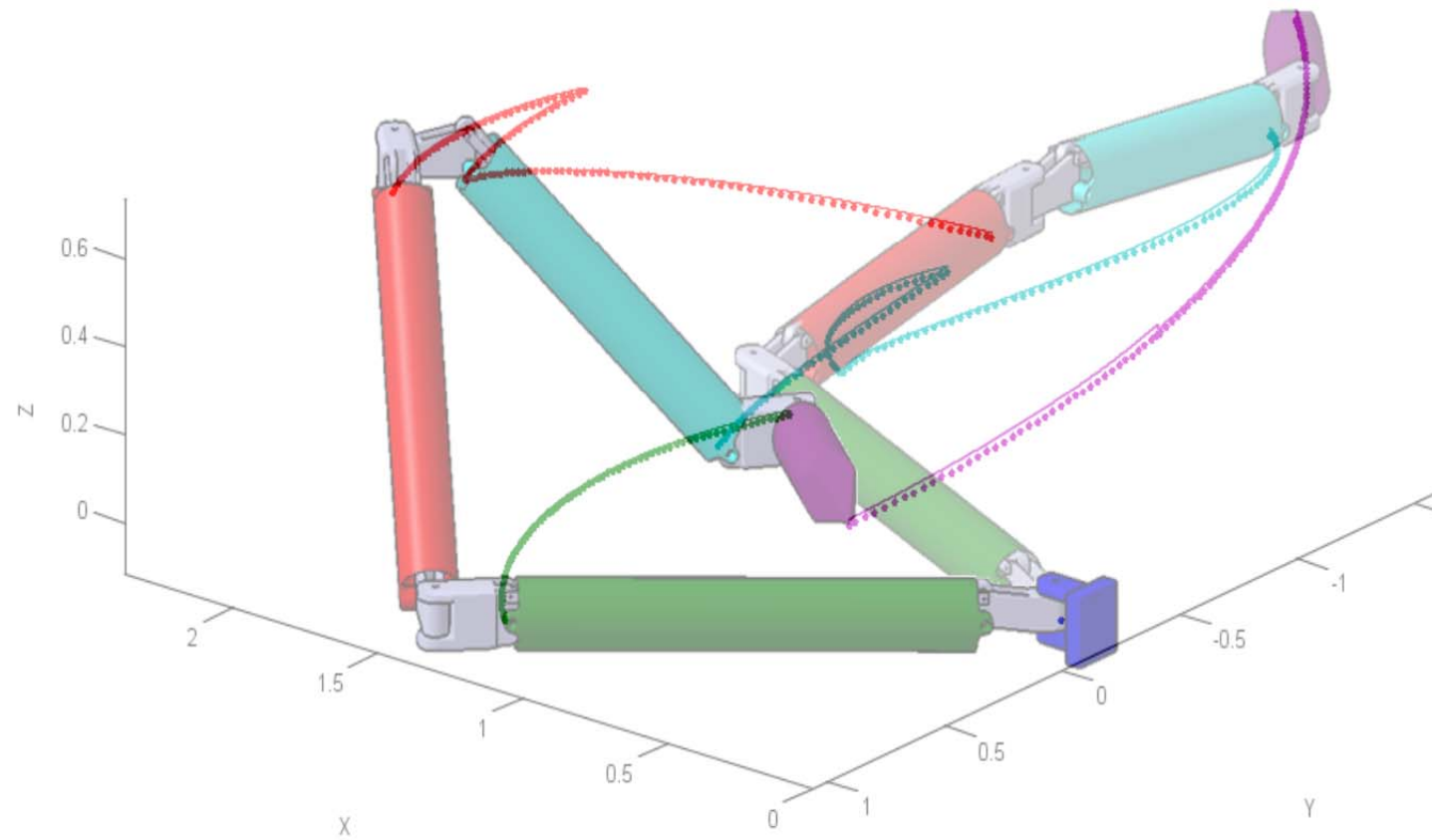
Fig. 4-18: 3D positions of downstream joint of parallelograms and probe points.
Dotted line is the input trajectory; continuous line is the simulated path.
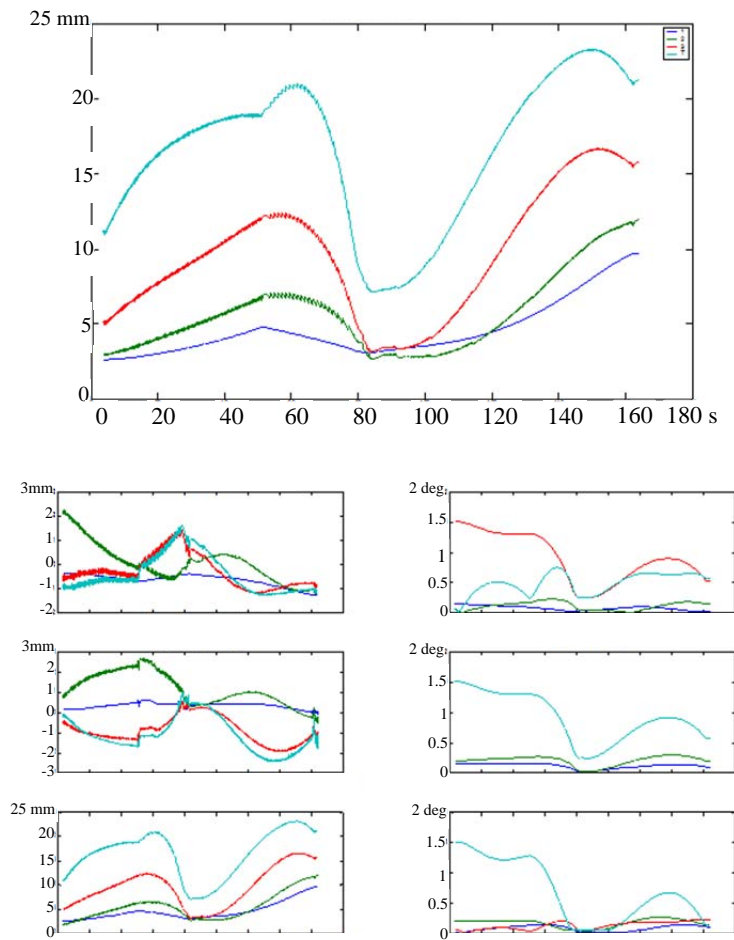**The two robot positions in the background show the initial and final positions of the path.**

Fig. 4-19: 3D position errors of the O_i points against simulation time.
Blue, green, red: points O_2, O_3, O_4; cyan: probe. Above: distance in mm.
Below left: position error along radial, toroidal and vertical, up to down.
Below right: angle error in yaw, pitch and roll, up to down.

Fig. 4-18 shows on the left the 3D trajectory of the points of interest in the segments and of the probe. Particularly, the purple line shows the path that the probe should follow in order to achieve a correct inspection of the outer divertor; the purple dots show the movement the robotic manipulator should follow, the distance between the two being due to control error and flexibility that is not measured by sensors. The distance between the presumed position given by the input trajectory and the actual position from simulation data is given against simulation time in Fig. 4-19.

The right figures in Fig. 4-18 show the positioning error of the robot along the trajectory for the reference points of each segment. This error is expressed in different directions, both in position and orientation.

According to the results given in Fig. 4-19, the trajectory tracking capability is 6 to 23 mm along the outer divertor inspection trajectory. The error is mainly along the vertical axis; its value on this axis matches 99% of the value of the 3D error, which is the difference at each time step between the position of the probe computed by the

trajectory and the 'real' simulated position. Due to the configuration of the torus and the position of the point of interest on the radial section, this error does not lead to any blind spot with the inspection scheme given in Fig. 4-13. A similar vertical error on the circle 3 trajectory (Fig. 4-14) would not have any effect on the viewed section either. Such an error during inner divertor inspection (Fig. 4-12) would however lead to a blind spot matching 14 mm of section length – 12 mm on the outer divertor edge and 2 mm on the inner divertor edge – out of 24.8 m of section length (0.05%). This error would therefore retain the requirement of reaching 99% of the complete section length with the probe within reach.

4.6.   Contributions of the chapter

The first contribution of the chapter deals with the operation of two critical components that have been developed in chapter 3. The proportional behaviour of the magnet-less motor, based on parts taken from an off-the-shelf coreless motor, has been established from measurements with a correlation factor of 0.9979. The nominal value of the torque constant is reached at a field that matches the peak field computed in finite element analysis of the motor with the magnet. Two means of operation have been discussed:

- First, at the same operation voltage as the original motor, where the torque rating is higher and velocity lower, making the power rating of the device the same value as the original motor, the motor operates with a 'magnetic reduction ratio' equal to the ratio between the local magnetic field and the field inside the original motor, which is 0.73 T in this case.

- Second, in pushing the motor to its nominal velocity by raising the operational voltage, the power rating of the motor is raised by the ratio between the local magnetic field and the field inside the original motor. Such a device shows an exceptionally high power rating to volume and weight ratio, which should prove useful in the design of a long-reach robotic manipulator. However, the tolerance of the insulation of the coil at the given voltage becomes a major concern. Further testing should be carried out on this specific issue, for example, with the motor manufacturer.

On the other hand, transistor operability, and therefore electronics, was proven to be insensitive to the magnetic field in any way at the level of field generated. Even if magnetic behaviours tend to be proportional to the local value of magnetic field density, it is advised to carry out the same tests at higher field values.

Further on, the structure of a robotic manipulator that has been proven through simulation capable of inspecting at least 99% of the IVVS vacuum vessel's first wall using three preferred trajectories has been presented. It uses technologies adapted to the environmental conditions presented in chapter 3, some of which actively use the local field for operation, in a long-reach robotic manipulator designed along the structure of the PAC and AIA presented in Appendix A. The control scheme of the robot is the one developed for the PAC and AIA, also presented in Appendix A. Such performance could not be achieved with the current state of art; to view 99% of the first wall, a

highly dextrous robotic manipulator is required, and the existing technologies were not sufficient to position the probe accurately. The only possibility was to shut off the magnetic field in order to use a design based on standard electric motors. Even with these conditions, and not taking into account the radiation levels, the AIA is the only device operating today capable of carrying out these tasks – with a severe constraint on the operation of the tokamak. One of the main issues of the AIA design is the vibration of the payload due to the flexibility of the design. This issue will be amplified when carrying a device such as the ENEA prototype for IVVS, as it carries a prism rotating at 1Hz, which is very close to the vibration mode of a long-reach robotic manipulator. In the suggested design, such a phenomenon can be damped thanks to the magnetic field, by placing conducting parts in the design as per the strategy developed in section 3.2.2, leading to better operating performance. In addition, magnetless motors will give an opportunity for a long-reach inspection robotic manipulator with a lower weight.

The work described in this chapter shows the operability of the stated technologies in order to build a long-reach robotic manipulator to carry a probe using the same principle as the ENEA design and matching the requirements regarding measurability on the first wall. This robot is designed based on the principles used to build the PAC, described in Appendix A. These are important contributions to the state of the art, because the only solution to carry out an inspection in ITER with the IVVS did not allow as great a view of the first wall as this one. In addition, the operation of a complex robot was believed to be impossible in this environment, yet the present study has proved that it is indeed possible, providing the technologies in the robot are correctly chosen and designed.

The study has also shown that the current construction of the ENEA prototype is not suited to this mode of operation; it is made exclusively out of 316L stainless steel, which will result in a horizontal magnetisation force towards the centre of the torus of up to 600 N. In any case, even with the simple deployer, this force will have to be taken into consideration. This issue has not been addressed in previous publications.

In order to prove the operability of these technologies, the behaviour of the robotic manipulator has been modelled using a simulation program. The typical control used on PAC architecture robotic manipulators has been tested on the trajectories expressed in the first part of the chapter to predict an accuracy that results in a positioning error at the probe of up to 20 mm, mainly along the vertical axis. This would result in not viewing part of the first wall – 14 mm out of the 28.4 m of the section length, which is compatible with the requirement expressed to be able to see more than 99% of the section length. In the current baseline ITER design, this requirement is not yet matched [58].

A detailed investigation on a control scheme more suited to the effects that the magnetic field has on the robotic manipulator has yet to be carried out. Such an investigation should compare different control schemes based on the measurements available that are discussed in the previous chapter. This particular topic has not been addressed in the thesis.

5.   CONCLUSION – CONTRIBUTIONS

5.1.   Summary of technological solutions

For each of the component families necessary to build a robot, numerous solutions have been provided to comply with the full set of environmental constraints of an inspection in ITER. All of these developments have been carried out by the author within the framework of the present study.

5.1.1.   Structures

- Magnetisation force: this force per volume is radial towards the inner wall of the torus when susceptibility is positive. All parts are affected even if they are not moving. Structural parts should be manufactured with paramagnetic materials with low susceptibility, such as Ti-6-4 (<0.16 N/kg). Stainless steel AISI 316L can be used for smaller parts as the magnetisation force is proportional to mass (28 N/kg).

- Eddy current drag: this dragging force fights rotating movement; translating parts are not affected. Low conductivity metals, such as again Ti-6-4 titanium alloy, should be preferred to keep eddy currents low, although the low velocity of a long-reach robotic manipulator keep them at a low level. However, placing conductive parts made of copper or beryllium alloy to obtain a controlled level of eddy current drag leads to a higher damping factor in structural dynamics and may therefore help achieve a better position accuracy in flexible designs.

5.1.2.   Actuation

- Ultrasonic rotary piezomotors: these fully UHV and magnetic compatible actuators should be used when low power (less than 10 W) is acceptable. Their tolerance to temperature is still to be assessed.

- Water hydraulics is the typical amagnetic high power solution. A correct design allows avoiding mechanical reduction gearings. Cavitation can be avoided by cooling down the system to 50°C or by using a circuit overpressurised by 20 bar on the whole hydraulic system, return and pump suction line included. Only jacks should be used, with a preference for single-way jacks to reduce the number of power lines to be returned to the base. Leaks should also be returned to the base. The 316 stainless steel jacks should be replaced by jacks with low magnetic permeability materials, such as Ti-6-4 titanium alloy. Valves or multiplexing cannot be used.

- Magnet-less brushed DC motor: a rotor and brushes taken from a standard coreless brushed DC motor, with a ferromagnetic part on the brush holder to tune the commutation with the local magnetic field. It uses the local magnetic field and thus requires it to operate. The high value of the field compared to that which a magnet can generate brings higher torque and lower velocity, just as a reduction gear would. By supplying higher voltage to match the original velocity, the power rating of the motor may also be raised, providing that the rotor supports the torque transmitted and the higher voltage mentioned previously. The motor's torque constant is proportional to the local field value; therefore, it is necessary to measure the field and use appropriate gain scheduling to control the motor. The weight of the motor is evaluated at 50% of the weight of the original motor.

- A standard brushed DC motor is an alternative in case the motor may only move on a radial plane of the torus or may not move at all. The magnet direction is to be aligned with the local field's, which is constant providing the above positioning conditions are met. It presents the same performance as the magnet-less motor when the field is on, and behaves like a standard motor when the field is off. The magnetisation force on the motor's yoke and magnet ranges between 60 N and 250 N towards the inner wall of the torus for a 500 g motor.

- In case of an electric actuation, rotational velocities are such that drag can become consequent, in particular on the first reduction gear. Drag formulas have been derived for a spur gear and a planetary gear for a given input torque, allowing the designer to choose the best solution in terms of drag.

5.1.3. Sensing

- Optical encoders with a deported light source and sensor are the most secure amagnetic design for an accurate position sensor in this environment. The maximum dose for these encoders is the actual dose of the optical fibre, which may be as high as a few dozen MGy.

- Coreless resolvers would be a standard two-pole resolver without its yoke, preferably a brushed resolver to avoid mutual induction between the primary and rotating transformer. The hull should be built in thick conductive materials to keep induction in the device and avoid induction to the wires outside the resolver. Multi-pole design is not operational in coreless configuration, leading to a lower resolution than standard resolvers. Such a device would be able to deliver the value of the local magnetic field and its direction, which is an important asset for magnet-less motor control. High shaft velocities (at least several rpm) would be required to make such a measurement.

- Absolute positioning of all the elements of the robotic manipulator can be achieved at the base by comparing local magnetic field measurements at different points of the robot with the actual magnetic field map of ITER. 10ppm field measurements throughout the robot, using 3D Hall sensors for

example, are necessary to achieve positioning accuracy of up to 0.8 mm. Of course, this can be done only when the magnetic field is on.

- Absolute velocity can be estimated by measuring the back electromotive force on coils placed in the device. Once again, the magnetic field is necessary to achieve this.

5.1.4. Data processing

- Electronics networks and circuits are highly affected by radiation, but simple digital circuits using discrete radiation tolerant transistors can be used. Analogue circuits may also be used but require more precise characterisation work on the transistors, particularly the evolution of their gain versus radiation levels. Such systems would take up a lot of space; therefore, circuits requiring few transistors are preferred. The high magnetic field effect on the components is negligible (except for the core of coils and transformers, which can be replaced by air cores), as is induction due to the natural movement of the robotic manipulator in the circuit loops. Twisting input and output wires together drastically reduces the effects of induction in the feed through. Printed circuit boards should be placed horizontally at parking to avoid induction in the circuit loops during quenches.

- Optical networks are completely immune to the magnetic field, except when using polarised light; therefore, input and output fibres should be twisted together to cancel the effect. Radiation tolerant fibres should be used.

5.2. Developments of the thesis

It has been proven here that it is possible to match the requirements of the combined constraints from temperature, vacuum, radiation and magnetic field for every element of a robotic manipulator. Moreover, among the solutions given here, a few turned the magnetic field constraint over to actually enhance the design, giving it better performance than would have been achieved in a magnetic-free environment:

- The possibility of using motors with behaviour close to that of a DC motor allows designing more accurate robotic manipulators.

- The possibility of increasing the power rating of a rotor by using the local field dramatically increases the power to weight ratio of such a device.

- The absolute positioning thanks to the measure of the field paves way for high precision positioning.

- Using conductive parts to generate a moderate eddy current drag damping the vibrations of flexible structures.

However, the choice of the actual components to be used in the robotic manipulator is highly dependent on the requirements of the robot. For example, for a robotic manipulator that should operate both with and without the magnetic field, a motor that may only use the local field for actuation can be considered. The goal of this study has

been to give a full array of possibilities, sweeping through the state of the art of robotics to select pertinent technologies from which the designer is free to choose the best ones for the given specifications.

This thesis also reveals which technologies can be used in the ITER inspection environment, allowing a complete dextrous remote handling device to be built that is temperature, vacuum, radiation and magnetic hardened for the deployment of an IVVS probe for other requirements. With additional hardening to radiation, these technologies can also be used for advanced first wall diagnostics mechanisms.

In order to illustrate those features a preliminary model has been set up using these technologies. According to the simulation results, it will be able to inspect more than 99% of the complete first wall. The region that are out of sight are between the blankets and the divertor – this region is impossible to see due to the configuration of the first wall and the limitations of the probe - and the last few mm of the divertor's edges, due to positioning errors.

REFERENCES

[1] R. Aymar, P. Barabaschi, Y. Shimomura, 'The ITER design', Plasma physics and controlled fusion, Vol. 44, Iss. 5, 2002, p. 519.

[2] F. Berghmans, B. Brichard, A. Fernandez, A. Goussarov, M. Van Uffelen, S. Girard, 'An introduction to radiation effects on optical components and fiber optic sensors', Optical Waveguide Sensing and Imaging, 2007, pp. 127–165.

[3] J. Campbell, Radiation hardness manual (RAD), Volume II: Gamma irradiation, Ref. ITER_D_222RR8, v1.0, ITER Organization, 2007.

[4] J. Chalfoun, C. Bidard, D. Keller, Y. Perrot, G. Piolain, 'Design and flexible modelling of a long reach articulated carrier for inspection', Proc. of the International Conference on Intelligent Robots, IROS 07, San Diego, USA, 2007, pp. 4013–4019.

[5] K. Chinzei, K. Miller, 'MRI Guided Surgical Robot', Proc. of the 2001 Australian Conference on Robotics and Automation, 2001, pp. 50–55.

[6] J.-J. Cordier, P. Hertout, L. Gargiulo, V. Cantone, B. Soler, 'New magnetic measurement of the Tore Supra toroidal field profile', Proc. of the 20th Symposium on Fusion Technology (SOFT98), 1998.

[7] S. Dhawan, D. Lynn, H. Neal, R. Sumner, M. Weber, R. Weber, 'Ideas on DC–DC converters for delivery of low voltage and high currents for the SLHC/ILC detector electronics in magnetic field and radiation environments', Proc. of the 12th Workshop on Electronics for LHC and Future Experiments, 2006, pp. 442–446.

[8] M. Ebertin, Y. Linda, Field effect transistor multiplexing circuit for time sharing a common conductor, U.S. Patent 3 601 634, 1970.

[9] L. Galbiati, T. Raimondi, P. Garetti, G. Costi, "Control and Operational Aspects of the Mascot 4 force feedback servomanipulator of JET.", Proc. of the 14th IEEE/NPSS Symposium on Fusion Engineering, IEEE, 1991, pp. 563–566.

[10] L. Gargiulo, P. Bayetti, V. Bruno, J.-J. Cordier, J.-C. Hatchressian, C. Hernandez, M. Houry, D. Keller, J.-P. Martins, Y. Measson, Y. Perrot, 'In-situ diagnostics handled by the AIA multipurpose carrier', Proc. of the 23rd Symposium on Fusion Engineering (SOFE 2009), San Diego, CA, 2009, pp. 1–4.

[11] D. J. Griffith, 'Chapter 11: Electricity and Magnetism', in E. R. Cohen, D. R. Lide, G. L. Trigg (eds.), AIP physics desk reference, Springer, 2003.

[12] K. Hameyer, R. Belmans, 'Permanent Magnet Excited Brushed DC Motors', IEEE Transactions on Industrial Electronics, Vol. 43, Iss. 2, 1996, pp.247–255.

[13] M. Houry, P. Bayetti, D. Keller, L. Gargiulo, V. Bruno, J.-C. Hatchressian, C. Hernandez, J.-P. Martins, Y. Measson, Y. Perrot, F.-X. Russotto, 'Development of in-situ diagnostics and tools handled by a light multipurpose carrier for tokamak in-vessel interventions', Fusion Engineering and Design, Vol. 85, Iss. 10–12, 2010, pp. 1947–1951.

[14] J. How, Plant description (PD) Chapter 12: Assembly, operation and maintenance, Ref. 2WAMC3, v2.1, ITER Organization, 2009, pp. 35–48.

[15] M. Imori, Y. Kanada, 'Low voltage power supply incorporating ceramic transformer', Proc. of the 7th Topical Workshop on Electronics for Particle Physics (TWEPP-07), 2007, pp. 389–393.

[16] A. Janot, C. Bidard, F. Gosselin, M. Gautier, D. Keller, Y. Perrot, 'Modeling and identification of a 3 DOF Haptic interface', Proc. of the 2007 IEEE International Conference on Robotics and Automation (ICRA), 2007, pp.4949–4955.

[17] S. Kakudate, K. Shibanuma, 'Rail deployment and storage procedure and test for ITER blanket remote maintenance', Fusion Engineering and Design, Vol. 65, Iss. 1, 2003, pp. 133–140.

[18] D. Keller, P. Bayetti, J. Bonnemason, V. Bruno, P. Chambaud, J.-P. Friconneau, L. Gargiulo, M. Itchah, S. Lamy, R. Le, Y. Measson, Y. Perrot, D. Ponsort, 'Real time command control

architecture for an ITER relevant inspection robot in operation on Tore Supra, Fusion Engineering and Design', Proc. of the 25th Symp. on Fusion Technology (SOFT-25), Vol. 84, Iss. 2–6, 2009, pp. 1015–1019.

[19] D. King, 'Space servicing: Past, present and future', Proc. of the 6th International Symposium on Artificial Intelligence and Robotics & Automation in Space (i-SAIRAS 2001), Canadian Space Agency, St-Hubert, Quebec, Canada, June 18–22, 2001.

[20] J. Knaster, E. Baynham, 'The determination of the current center line of the TF coils in ITER', IEEE Transactions on Applied Superconductivity, Vol. 20, Iss. 3, 2010, pp. 1475–1478.

[21] C. Lange, J.-C. Piedboeuf, M. Gu, J. Kövecses, 'Flexible space manipulators: Modeling, simulation, ground validation and space operation', in M. O. Tokhi, A. K. M. Azad (eds.), Flexible robots manipulators: Modeling, simulation and control, IET, 2008, pp. 147–206.

[22] P. Leroux, W. De Cock, M. Van Uffelen, M. Steyaert, 'Design and radiation assessment of optoelectronic transceiver circuits for ITER', Proc. of the 2008 Topical Workshop on Electronics for Particle Physics (TWEPP-08), CERN, 2008, pp. 167–171.

[23] P. Leroux, M. Van Uffelen, F. Berghmans, A. Giraud, 'Design and assessment of a high gamma-dose tolerant VCSEL driver with discrete SiGe HBT's', Proc. of the 8th European Conference on Radiation Effects on Components & Systems (RADECS 2005), IEEE/RADECS, 2007, pp. J2-1–J2-7.

[24] R. Liang, P. Dosanjh, D. A. Bonn, W. N. Hardy, A.J. Berlinsky, 'Lower critical fields in an ellipsoid-shaped $YBa_2Cu_3O_{6.95}$ single crystal', Physical Review B., 1994, Vol. 50, Iss. 6, pp. 4212–4215.

[25] B. Loriferne, Analog-Digital and Digital-Analog Conversion, Heyden & Son Ltd., London, 1982.

[26] A. Loving, P. Allan, N. Sykes, S. Collins, P. Murcutt, 'Development and application of high volume remote handling systems in support of JET and ITER', Fusion Engineering and Design, Vol. 87, Iss. 5-6, 2012, pp. 880–884.

[27] G. Matthews, M. Beurskens, S. Brezinsek, M. Groth, E. Joffrin, A. Loving, M. Kear et al., 'JET ITER-like wall—overview and experimental programme', Physica Scripta, Iss. T145, 2011.

[28] S. Michelis, F. Faccio, A. Marchioro, M. Kayal, 'Inductor based switching DC-DC converter for low voltage power distribution in SLHC', Proc. of the 7th Topical Workshop on Electronics for Particle Physics (TWEPP-07), 2007, pp. 399–403.

[29] M. Muntener, A. Patriciu, D. Petrisor, D. Mazilu, H. Bagga, L. Kavoussi, K. Cleary, D. Stoianovici, 'Magnetic resonance imaging compatible robotic system for fully automated brachytherapy seed placement', Urology, Vol. 68, Iss. 6, 2006, pp. 1313–1317.

[30] C. Neri, A. Coletti, ITER IVVS: EFDA Task TW6-TVR-IVV final report, Ref. 2ECEH7, v1.0, ENEA, 2008.

[31] C. Neri, P. Costa, M. Ferri De Collibus, M. Florean, G. Mugnaini, M. Pillon, F. Pollastrone, P. Rossi, 'Iter in vessel viewing system design and assessment activities', Fusion Engineering and Design, Vol. 86, Iss. 9, 2011, pp. 1954–1957.

[32] H. Olsson, K. J. Åström, C. Canudas de Wit, M. Gäfvert, P. Lischinsky, 'Friction models and friction compensation', European Journal of Control, Vol. 4, No. 3, 1998, pp. 176–195.

[33] Y. Perrot, L. Chodorge, P. Desbats, J.-P. Friconneau, G. Piolain, 'Scale one field test of a long reach articulated carrier for inspection in spent fuel management facilities', Proc. of the 10th American Nuclear Society Meeting, 2004.

[34] Y. Perrot, L. Gargiulo, M. Houry, N. Kammerer, D. Keller, Y. Measson, G. Piolain, A. Verney. 'Long-reach articulated robots for inspection and mini-invasive interventions in hazardous environments: Recent robotics research, qualification testing, and tool developments', Journal of Field Robotics, Vol. 29, Iss. 1, 2012, pp. 175–185.

[35] J.-C. Piedboeuf, M. Doyon, P. Langlois, R. L'Archevêque, 'SYMOFROS: A flexible dynamics modeling software', Fifth International Symposium on Artificial Intelligence, Robotics and Automation in Space (ESA SP-440), 1–3 June, 1999.

[36] C. S. Pitcher, B. LaBombard, R. Danforth, W. Pina, M. Silveira, B. Parkin, 'Divertor bypass in the Alcator C-Mod tokamak', Review of Scientific Instruments, Vol. 72, No. 103, 2001.

[37] I. Ribeiro, C. Damiani, A. Tesini, S. Kakudate, M. Siuko, C. Neri, 'The remote handling systems for ITER', Fusion Engineering and Design, Vol. 86, Iss. 6, 2011, pp. 471–477.

[38] A. Rolfe, 'Experience from the first ever remote handling operations at JET', BNES Conference on Remote Techniques for Hazardous Environments, 1999.

[39] W. J. Rugh, 'Analytical framework for gain scheduling', Control Systems Magazine, Vol. 11, Iss. 1, Jan. 1991, pp. 79–84.

[40] H. Saarinen, T. Kivelä, L. Zhai, V. Hämäläinen, J. Karjalainen, L. Aha, L. Heikkilä et al. 'Results of CMM standalone tests at DTP2', Fusion Engineering and Design, Vol. 86, Iss. 9, 2011, pp.1907–1910.

[41] P. Schnizer, H. R. Kiesewetter, T. Mack, T. Knapp, F. Klos M. Manderla, S. Rauch, M. Schonecker, R. Werkmann, 'A mole for measuring pulsed superconducting magnets', IEEE Transactions on Applied Superconductivity, Vol. 18, No. 2, 2008, pp.1648–1651.

[42] D.J. Schulten, U.G. Termote, M.J.H. Couwenberg, 'EuroSim and its applications in the European robotic arm programme', in B. Schürmann (ed.), Proceedings of 19th Data Systems in Aerospace Conference (DASIA 2000), Montreal, Canada, 2000, European Space Agency, ESA SP-457, 2000, p. 417.

[43] J. Shammai, M. Athans, "Guaranteed properties of gain scheduled control for linear parameter-varying plants", Automatica, Vol. 27, No. 3, 1991, pp. 559–564.

[44] N. Smick, B. LaBombard, C.S. Pitcher, 'Plasma profiles and flows in the high-field side scrape-off layer in Alcator C-Mod', Journal of Nuclear Materials, Vol. 337–339, PSI-16, March 2005, pp. 281–285.

[45] J. L. Smith, J. S. Brooks, C. M. Fowler, B. L. Freeman, J. D. Goettee, W. L. Hults, J. C. King, P. M. Mankiewich, E. I. De Obaldia, M. L. O'Malley, D. G. Rickel, W. J. Skocpol, 'Low-temperature critical field of YBCO', Journal of Superconductivity, Vol. 7, Iss. 2, 1994, pp. 269–270.

[46] G. R. Sutherland, P. B. McBeth, D. F. Louw, 'NeuroArm: an MR compatible robot for microsurgery', International Congress Series, Vol. 1256, 2003, p.504-508.

[47] T. Tajima, 'Possibility of MgB2 application to superconducting cavities', Proc. of the 8th European Particle Accelerator Conference (EPAC), 2002, pp. 2289–2291.

[48] J. Tammisto, J. Mattila, M. Irving, M. Siuko, M. Vilenius, 'Radiation effects on friction and leakage properties of water hydraulics seals', Proc. of the Tenth Scandinavian International Conference on Fluid Power, SICFP'07, 2007.

[49] E. Trostmann, Water hydraulics control technology, Marcel Dekker, Inc., New York, 1996.

[50] M. Van Uffelen, 'Radiation tolerance assessment of remote handling components', EFDA Task TW1 – TVA / RADTOL Final Progress Report, SCK CEN – ENEA Report R-3706, 2002.

[51] M. Van Uffelen, S. Geboers, P. Leroux, F. Berghmans, 'High total dose gamma radiation assessment of commercially available SiGe Heterojunction Bipolar Transistors', Proc. of SPIE, 2005, pp. 58970–58971.

[52] J. Virtanen, 'Enhancing the Compatibility of Surgical Robots with Magnetic Resonance Imaging', Doctoral Dissertation, University of Oulu, 2006, ISBN 951-42-8066-0.

[53] J. Virtanen, M. Malila, Y. Louhisalmi, P. Hyvärinen, K. Nevala, 'Machine vision based fiber optic joint sensor for MR-compatible robot', International Congress Series, Vol. 1268, 2004, p.555-560.

[54] C. Völlinger, 'Superconducting magnetisation modelling for the numerical calculation of field errors in accelerator magnets', Doctoral Dissertation, Technical University of Berlin, 2002.

[55] P. Wenschot, 'A new nickel-aluminum bronze alloy with low magnetic permeability', Metallurgical and Materials Transactions A, Vol. 28, Iss. 3, 1997, pp. 689–697.

[56] L. Worth, R. Pearce, D. Sands, Y.-H. Kim, N. Holtkamp, ITER Vacuum Handbook, Ref. ITER_D2EZ9UM, v2.3, ITER Organization, 2009.

[57] Design Description Document DDD 2009, DDD 11-2: Toroidal Field Coils and Structures, Ref. ITER_D_2MVZNX, v2.2, ITER Organization, 2009.

[58] Design Description Document DDD 2004, DDD 23-5: In-Vessel Viewing, Ref. ITER_D_2LHCDZ, v1.0, ITER Organization, 2004.

[59] In-Vessel viewing system for ITER: Task TW3-TVR-IVV Final Report, Ref. 25X68M, v1.1, ENEA, 2004.

[60] Belgian Nuclear Research Centre, Nuclear systems research, Available at: http://www.sckcen.be/en/notre-recherche/scientific-institutes-expert-groups/advanced-nuclear-systems/advanced-reactor-instrumentation. Last accessed: 4/3/2012.

[61] Topical Workshop on Electronics for Particle Physics (TWEPP 09): http://twepp09.lal.in2p3.fr. Proceedings of TWEPP 08: http://doc.cern.ch/yellowrep/2008/2008-008/cern-2008-008.pdf.

[62] Magnetic Component Engineering Inc., Materials / Neodymium Iron Boron (Sintered) / N3575, http://www.mceproducts.com/materials/material-details.asp?id=1008&MaterialTypeCode=1003. Last accessed: 4/3/2012.

[63] Magnetic Component Engineering Inc., Materials / Samarium Cobalt (Sintered) / S3069, http://www.mceproducts.com/materials/material-details.asp?id=1041&MaterialTypeCode=1005. Last accessed: 4/3/2012.

[64] MatWeb, Available at: www.matweb.com.

[65] Discovery Technology International ultrasonic rotary actuators, from Ø38 mm to Ø80 mm motors http://www.discovtech.com/files/categoryDownload/RotaryPiezomotorBrochure11090121231.pdf. Last accessed: 4/3/2012.

[66] Maxon Motor USA, Available at: www.maxonmotorusa.com. Last accessed: 4/3/2012.

[67] Gaussmeter and probe datasheets (last accessed: 4/3/2012): http://www.oeco.com/FWBell/PDF%20Documents/5100%20datasheet.pdf http://www.oeco.com/FWBell/PDF%20Documents/5100_probes_datasheet.pdf.

[68] Faulhaber 3257 motor http://www.faulhaber.com/uploadpk/EN_3257_CR_DFF.pdf. Last accessed: 4/3/2012.

[69] EuroSim, Available at: http://www.eurosim.nl.

Page intentionally left blank

Appendix A. PAC and AIA structure

This Appendix presents the layout of the AIA ([18], section 2.2.1) and the PAC ([33], section 2.2.2) that was chosen for the demonstrator.

1) Presentation of the kinematics

The design is made of several similar segments. The number of segments is chosen in respect to the task to be executed. Each segment yaw and pitch joints are actuated. The pitch movement features a parallelogram structure in each segment in order to support the pitch torque (Fig. A-1).
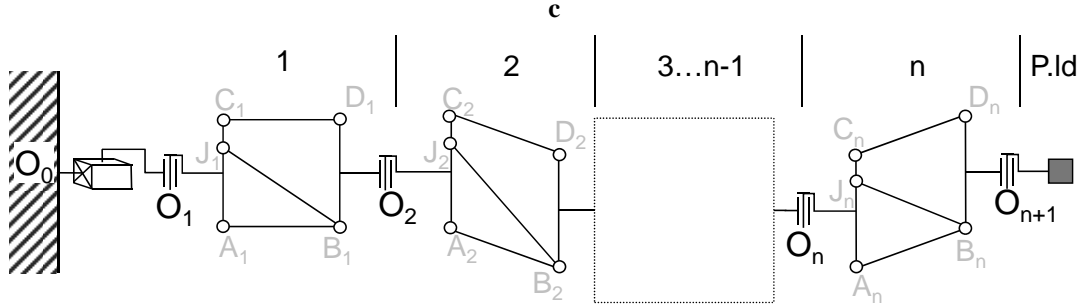
Fig. A-1: Kinematics of the device.
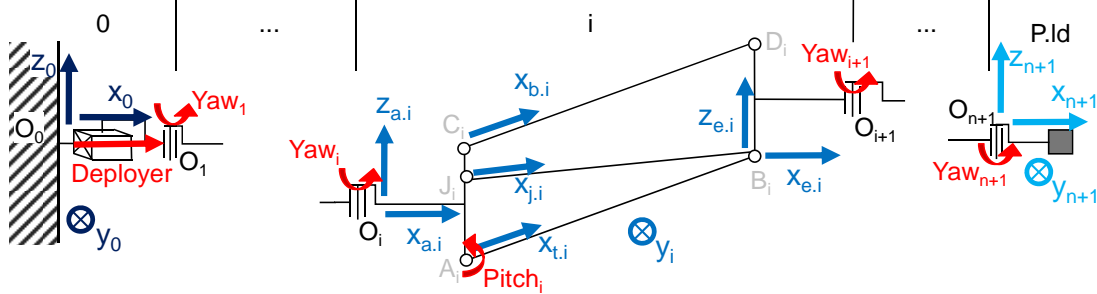
Fig. A-2: Angles and frames of the device.
y_i **is common to all the frames of segment i.** $z_{b.i}$, $z_{j.i}$ **and** $z_{t.i}$ **are not represented.**

In PAC and AIA, actuation is performed by DC motors with a high reduction ratio gearbox linked to roller lead-screws sitting on an axial bearing and featuring low pitch. This configuration allows small diameter motors that fit on the diagonal of the tube without interfering with the structure for the considered parallelogram pitch strokes and low actuation velocities in order to avoid exciting the eigenmodes of the structure that could lead to severe vibration. In the PAC and AIA, the actuation velocities are 15 mrad/s. The resulting actuator is an electric jack. For the yaw joint, the jack pulls on a cable that is attached to a pulley located on the yaw axis; for pitch, the jack is on the diagonal J_iB_i of the parallelogram. There are two sets of sensors for each joint: one at the level of the joint and another at the level of the motor.
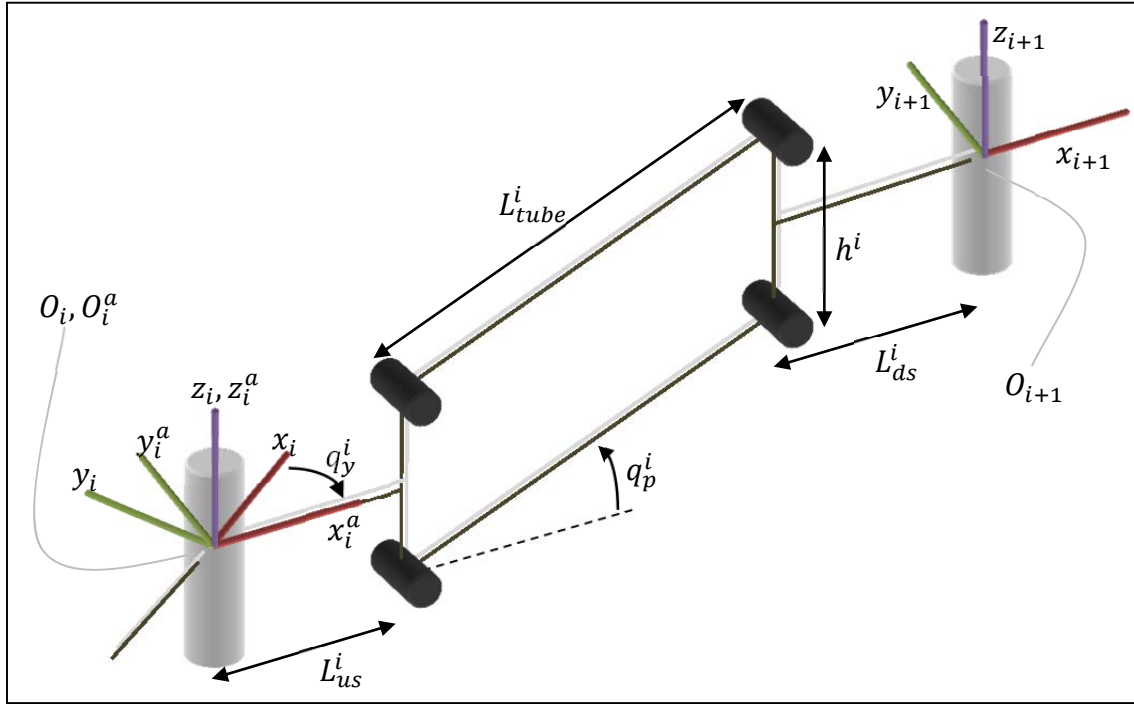
Fig. A-3: Parameters of a segment.

With the parameters given in Fig. A-3, it is possible to give the transformation matrix from the frame of reference (O_i,x_{ei-1},y_{i-1},z_{ei-1}) to (O_{i+1},x_{ei},y_i,z_{ei}), expressed in (A-5-1). This expression allows the computation of the transformation matrix from the base frame of reference to the end-effector's by multiplying the matrices of the n segments together.

$$T_i^{i'} = \begin{bmatrix} cy^i & -sy^i & 0 & 0 \\ sy^i & cy^i & 0 & 0 \\ 0 & 0 & 1 & 0 \\ 0 & 0 & 0 & 1 \end{bmatrix}, with \begin{cases} cy^i = \cos(q_y^i) \\ sy^i = \sin(q_y^i) \\ cp^i = \cos(q_p^i) \\ sp^i = \sin(q_p^i) \end{cases}$$

$$T_{i'}^{i+1} = \begin{bmatrix} 1 & 0 & 0 & L_{us} + L_{tube}.cp^i + L_{ds} \\ 0 & 1 & 0 & 0 \\ 0 & 0 & 1 & L_{tube}.sp^i \\ 0 & 0 & 0 & 1 \end{bmatrix}$$

$$T_i^{i+1} = T_i^{i'} T_{i'}^{i+1} = \begin{bmatrix} cy^i & -sy^i & 0 & 0 \\ sy^i & cy^i & 0 & 0 \\ 0 & 0 & 1 & 0 \\ 0 & 0 & 0 & 1 \end{bmatrix} \begin{bmatrix} 1 & 0 & 0 & L_{us} + L_{tube}.cp^i + L_{ds} \\ 0 & 1 & 0 & 0 \\ 0 & 0 & 1 & L_{tube}.sp^i \\ 0 & 0 & 0 & 1 \end{bmatrix}$$

$$T_i^{i+1} = \begin{bmatrix} cy^i & -sy^i & 0 & cy^i(L_{us}^i + L_{ds}^i + L_{tube}^i.cp^i) \\ sy^i & cy^i & 0 & sy^i(L_{us}^i + L_{ds}^i + L_{tube}^i.cp^i) \\ 0 & 0 & 1 & L_{tube}^i.sp^i \\ 0 & 0 & 0 & 1 \end{bmatrix} \qquad \textbf{(A-5-1)}$$

The parallelogram is composed of:
- A thin tube of outer diameter Ø160 mm made of stiff material, mostly undergoing compression and torsion forces.
- Rods in the upper region of the parallelogram that are solicited in traction.

From there on, 5 bodies are selected for each segment (from O_i to O_{i+1}):
- Index a for the second yaw clevis (points Oi, Ai, Ji, Ci).
- Index t for the tube (points Ai, Bi).
- Index b for the rods (points Ci, Di).
- Index j for the jack (points Ji, Bi).
- Index e for the remaining end of the parallelogram (points Bi, Di, Oi+1).

2) Flexibility

Considering its length and weight, such a structure is inherently flexible, which means it is difficult to take it into account. Indeed, if the parallelogram structure allows facing vertical forces without giving much flexion when the robot is in full extension (the total vertical deflexion at the end of the arm is 3 mm in the case of the AIA, based on testing, through setting the length of the rods at a value that compensates for flexion), this same vertical deflexion reaches as high as 320 mm when the arm is drawing a circle (yaw joint angle values around 45° for every segment). Because of the torsion of the tubes, there is an additional horizontal deflexion of 140 mm. In total, the deflexion can therefore get as high as 350 mm at the end effector.

Extensive work has been carried out at CEA-LIST to construct a mathematical flexion model of the arm [4] on the basis of which a MATLAB program has been written. This is a static model; therefore, all the dynamics aspects of the structural equations have been ignored. Several flexible parameters have been identified in the design for each parallelogram, as shown in Fig. A-4.
- T1 is the torsion of the first yaw clevis.
- F is the flexion of the yaw axis.
- R is the flexibility of the yaw actuation cable.
- T2 is the torsion of the second yaw clevis.
- Tp is the torsion of the parallelogram due to the flexibility of the tube.

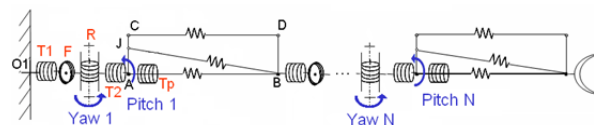Each yaw joint is the succession of the flexible (T1, F, R, T2) and rigid (yaw) axes between O and A.

Fig. A-4: **Flexible model of the manipulator.**
Flexible parts of the parallelogram are represented with a spring to which is associated a flexible parameter, length or angle. Arrows show the rigid yaw and pitch axes.

The parallelogram is then supposed to stay planar, which means that A, B, C, D and J are in the same plane. This plane is the vertical plane transformed successively by T1, F, R, yaw, T2, pitch and Tp. Once the plane is set, the different angles of the parallelogram (Fig. A-5) are computed from the lengths of the rods, tube and jack. Thanks to a forward kinematics model, these allow the position of the different points of the parallelograms to be obtained and, therefore, of the whole robot.
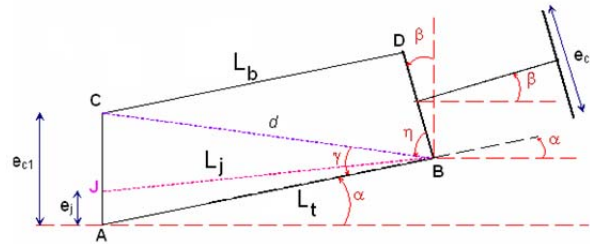

Fig. A-5: **Flexible angles in the parallelogram**
due to the lengthening of the tube, the rods and the jack.

From these positions the forces on each of the given flexible axes are computed, which give via their stiffness (calculated with the robot parameters) a new set of flexible parameters. These new flexible parameters are fed back in the model until they are assumed to have converged, the criterion being the variation of the deformation values when it drops below 10^{-6} m or rad. The program then uses the flexible parameters on which the program converged in order to compute the positions of the links of the robot.
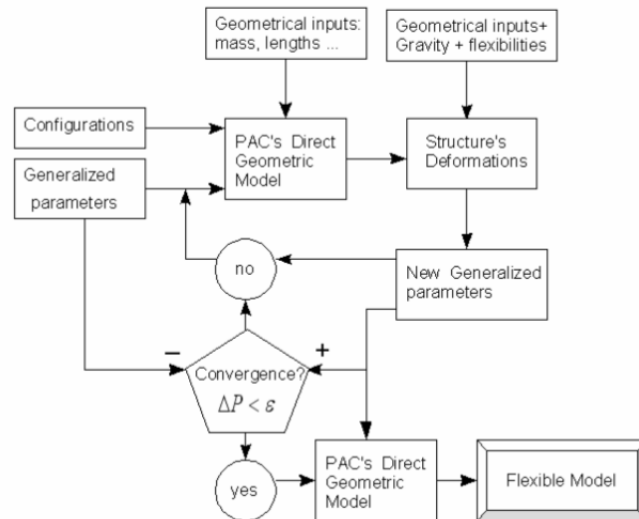
Fig. A-6: Flexible model algorithm, developed in [4].

There has been no theoretical proof of the convergence of this algorithm, but it appears that it converges after 3 to 4 iterations. When implemented on the PAC in [4], the error between the measured position of the tip of the 10 m long robot and the

position estimated by the program has been calculated at 22 mm, 50% of which is due to the lack of calibration of the geometrical inputs.

3) Control scheme

In order to avoid exciting the dynamics of the design, a Proportional Derivative controller has been implemented based on the error calculated between the measure of the present joint angle and the expected angle from a trajectory computed offline. Considering the large amount of friction in the actuation block, an offset on the command has been added. The control strategy, described in Fig. A-7, is the same for all of the joints.
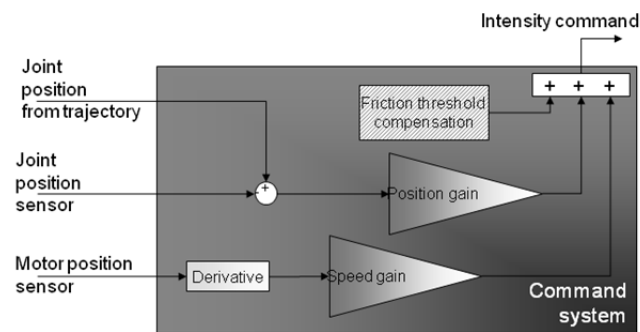
Fig. A-7: Typical control scheme of a PAC architecture.

Appendix B.   Simulation program

Complete simulation programs that include models for actuation, sensing and control of a robot are already in use in space robotics, a field of application where testing in real operation conditions is a considerable issue. A program of this kind named SYMOFROS [21][35] has been developed by the Canadian Space Agency (CSA) for the Canadarm [19] used on the International Space Station (ISS). The robot is modelled inside the program as several rigid and flexible links (beams flexible in torsion and bending) that the robot is built from; these links can also be connected to create kinematical loops. The program may be controlled by a user-custom controller written with MATLAB Simulink. The program can also be run in real-time.

A similar program exists for the European Robotic Arm (ERA) [19], which has been written using EuroSim [42][69], a reconfigurable real-time execution environment complying with the European Space Agency (ESA) requirements. ERA features an open-chain of flexible and rigid bodies representing the robot with a model for actuation, sensors, communication and on-board software and allows hardware-in-the-loop simulations for training sessions.

These programs are mainly meant for training simulation due to the impossibility of operating the system in similar conditions on Earth. However, they cannot be used for any robot; EuroSim cannot handle kinematic loops and dealing with linear joints in SYMOFROS, in the case of a jack or of a traction rod, is presently impossible, even if this last program offers many possibilities in terms of mechanical layouts. They actually include their own kinematical models and do not allow the designer to put his own models in the loop.

At CEA-LIST, during the different design phases of the PAC and the AIA, different models for geometrics, flexibility, actuation and friction with increasing complexity over time have been developed and identified [4][16]. Using these models was essential to avoid a costly phase of rewriting the models. From this point on, the simulation program is designed as a way to assemble these models together, using the Newton-Euler equations for determining new position from forces on the degrees of freedom, converted into an acceleration through Newton-Euler equations.

1) Structure of the simulation program

The goal is to simulate the behaviour of a long-reach robotic manipulator with the structure of the PAC and AIA (presented in 2.2.1 and 2.2.2, and completely described in Appendix A). The main issue of simulating such a robot is the mechanical behaviour of the closed kinematical loop; this specific problem has been solved by the direct kinematical model described in Appendix A, section 2), using an iterative algorithm. The simulation program developed here is therefore tailored around this model and the

program used to solve it, which has already been proved to be accurate in real conditions [4].

The main issue is that the model deals with a static structure. However, the low velocity of long-reach robots generally allows discarding of the dynamic effects in the structure. The simulation will therefore be addressed as a series of juxtaposed static configurations solved by the model and separated by a constant time delay.

Each configuration is determined by the joint angles, which are determined from the previous configuration in the list. Consider a solved configuration #N in the list. The model computes the forces that are necessary to support the structure at position #N, which are summed to the forces that generate the actuator based on a control and actuation model. Using an estimated inertia computed from the position of the different bodies in the robot, provided by the direct kinematical model, the resulting force is converted into a joint acceleration #N through the use of Newton-Euler equations written in the space of the degrees of freedom of the robot.

Considering the presence of a constant time shift between two configurations, a resulting velocity can be computed based on the velocity #N, and therefore a position #N+1 can be used to represent configuration #N+1.
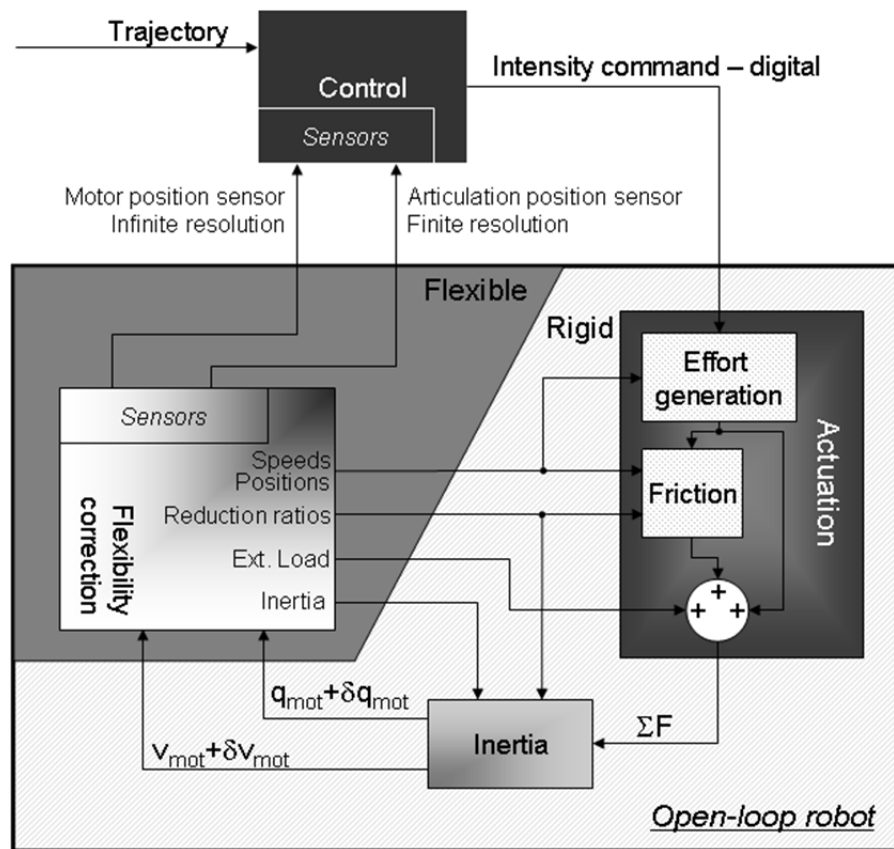
Fig. A-8: Structure of the simulation program.

The simulation program (Fig. A-8) is written in the same way as a closed-loop system. The degrees of freedom addressed here are the actuated degrees of freedom. The program enclose the different blocks simulating the controller, the motors and the inertia for each joint. This is a major difference from the simulation programs presented in the introduction of this Appendix, as these program consider the robot as a whole system depicted by its kinematical links; each of them transfers movement and forces to the next one, and the program computes the movement equations at the level of each link. This simulation program computes these equations for the robot's controlled degrees of freedom only and depicts the rest of the robot using a forward kinematical model. This difference is due to the nature of the program developed for this architecture that has been used as the basis for this simulation program, presented in Appendix A: the forward kinematical model of the robot taking into account the flexibility joints developed for the PAC and AIA architecture.

The open-loop robot simulation is addressed in two phases. The first phase computes the forces and applies the Newton-Euler equations to compute a new position: flexibilities of the system are not yet considered, as such it is as is the program simulates the robot and its components as if they were rigid. Actuation and inertia blocks are designed this way. Out of the inertia block, each component is given a reference position and velocity that are accounted for as if the robot were a rigid assembly.

In a classical closed loop system, the inertia block would provide velocities and positions for each actuated joint, which would be used by the other blocks as inputs at the next step. In a rigid robot, these reference positions and velocities would be directly used to compute the forward kinematics of the robot, and as a result the forces, inertias and sensor feedbacks of each degree of freedom. Instead of this, during the second phase of this simulation program ('flexible' section), reference velocities and positions given by the inertia block and for the flexible joints are corrected in order to take into account the flexibilities of the robot. These corrections are necessary to take into account in particular the flexion of the parallelogram mechanism in the case of pitch, and the elasticity of the actuation cable in the case of yaw. These corrected positions and parameters are computed by the flexibility correction block, which includes a forward kinematical model with flexible virtual joints for the static resolution of the vertical parallelogram architecture presented in Appendix A. The corrected positions and velocities are then fed into the other blocks of the open-loop robot at the next step.

Such a correction algorithm is possible due to the dynamics of the system. The robot actuation dynamics are expected to be slow with respect to the structural dynamics of the assembly. This velocity is acceptable for slow long-reach robots such as those presented in [18][19][21][33] moving at a few 10^{-2} rad.s^{-1} at each joint. Such a low velocity allows discarding the effects of the structural dynamics equations coupling component mass and flexibility, while keeping an eye on the expected effects of flexibility on the control.

These calculations imply computing the forces undergone by each of the 5 bodies expressed in Appendix A in each of the 3 segments and, therefore, the position of the different bodies of the robot in space. These are taken into account in the computation of the forward kinematical model.

Prior to the launching of the simulation itself, the simulation program is first initialised. The first step of the operation consists of obtaining the robot's parameters from the parameters file and getting the simulation parameters (including the controller parameters) from another file.

Considering that it is a fixed time-step simulation, the diagram has a starting point with a starting value to be calculated. The second role of the initialisation is to compute this starting value. The starting point of the simulation is right after the forward kinematical model; the first calculation of the model takes place during initialisation

The following sections show the constitution of the 'flexibility correction', 'control', 'actuation chain' and 'inertia' blocks.

2) Flexibility correction

The flexibility correction block embeds the forward kinematical model of the robot taking into account the flexibility joints, coined further in the text as "flexible forward kinematical model", in order to distinguish it from the forward kinematical model of the robot taking into account only the joints of the mechanism. This flexible forward kinematical model is used by the designer to calculate the position of any part of the structure for a given input joint configuration, taking into account the various flexibilities in the mechanism. With the positions of the bodies of the robot (upstream clevis, tube, rods, jack and downstream clevis), it is possible to compute the loads and inertias on the different degrees of freedom.
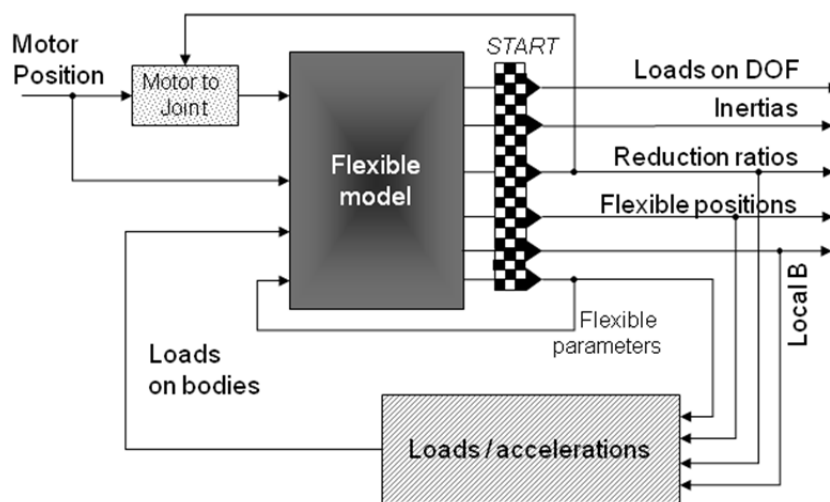
Fig. A-9: Flexibility correction block construction.

Fig. A-9 shows the starting point of the simulation. The resolution of the flexible forward kinematical model is the critical block for time optimisation; therefore, at each time step, the values from the flexibility correction block are the values from the previous step.

Loads and accelerations taken into account here are the gravity and eventual forces on the bodies, such as magnetic forces in the case of the robotic manipulator developed in this thesis. Forces can be added on any part of the robot and included in the body's reference or in the global reference, and can be set in function of the position of the said part. The different forces thus computed are summed, thus providing a load for each of the degrees of freedom that are representative of the total force that the actuator has to provide.

The input configuration is the motor position converted into an articulation position using the speed reduction ratios calculated during the previous step. This means that the input configuration takes into account the "real" speed reduction ratio for pitch, taking into account the flexibility of the mechanism.

3) Actuation chain

This block contains the actuation model that includes components such as motors, gearboxes, etc., and the friction model computed from the forces delivered by the actuators. The purpose of this block is to calculate the sum of the forces on the different degrees of freedom. It is separated in two subsystems: the effort generation block containing the actuation model and the friction block for the friction model. The model for external loads calculation depending on position is included in the flexibility correction block.

For the example developed here, the effort generation block simulates the electronics and mecatronics phenomena involved in the components that produce torques or forces. The flexibility correction block provides the position, velocities and other environmental values needed for resolution, such as the local magnetic field density value at the motor for magnet-less motors.

The computed force is used to estimate the friction force through the friction block. In the program developed here, a Coulomb threshold friction model is used, with consideration on the reversibility of the actuation chain based on friction thresholds at the level of each component of the actuation chain. Advanced friction models [32] can be applied here, such as the LuGre friction model, in order to investigate low-velocity phenomena such as stick-slip.
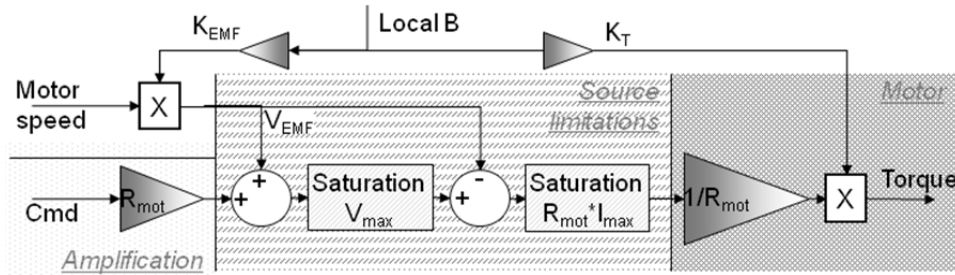
4) Effort generation

Fig. A-10: Diagram: Effort generation.

The torque is generated by DC motors powered by an amplifier converting the digital current command. The amplifier is capable of generating at most in absolute value V_{max} in voltage and I_{max} in current. Motor velocity is also an input from this same block.

On the other hand, the motor (resistance R_{mot}, torque constant K_T, EMF constant K_{EMF}), when turning at a velocity v_{mot} and given a current i_{mot}, shows a voltage of $K_{EMF}*v_{mot}+R_{mot}*i_{mot}$. This voltage is balanced by the amplifier voltage. From i_{mot} it generates a torque equal to K_T*i_{mot}. Electrical transient states are not considered.

An addition to the original simulation program has been implemented here, specifically for the thesis. Indeed, because the design studied uses standard or magnet-less DC motors as presented in section 3.3.2 whose torque constants change with the local value of the field, these values have to be changed according to the value computed from the motor position.

5) Friction

Each element of the actuation chain that produces friction is represented in the friction block: the motor, the gears, the axial bearing of the lead screw, the lead screw itself and the articulation bearing(s). Each of these components is characterised in the robot's parameters file with either an efficiency parameter or a threshold friction, applied using the Coulomb model. The direction of friction is given by the velocity at the considered point of the chain. The coupling matrices and the reduction ratios allow stepping from one component of the actuation chain to the next.

However, if the motor velocity is computed by inertia and not prone to any correction because of the elasticity of cables used for actuation, the joint velocity will require such a correction if it is to be accurate. The flexible model calculates angles due to the flexibility of the actuation chain and lengths as a function of the forces: the actual velocity is then computed by deriving the joint positions.

6) Inertia

This block applies Newton-Euler equations with the sum of the forces from the actuation block (that is the sum of the loads on each degree of freedom and the friction generated in each actuation chain) in order to calculate the acceleration of the different degrees of freedom. The inertia is provided thanks to the calculation of the position of the bodies of the robot by the flexible forward kinematic model. The acceleration is then integrated into velocity and then position.

The new position is then ready to be fed back into the flexible model for the next time step.

7) Control
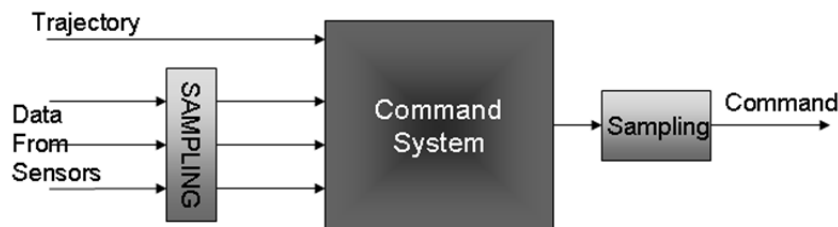
Fig. A-11: Construction of the control block.

The control block is the only block outside the open-loop robot system. This means that it has limited access to the data given by the flexibility correction block: only data recovered by a real physical sensor may be transmitted to the control block. This is a significant difference with respect to the other blocks inside the open-loop robot, since they can access any data computed by the forward kinematical model. It includes both the control model and the sensor models.

The purpose of this block is to contain the command system of the robot. It gathers data from the sensors, considering that the resolution of those sensors may be finite, compares it to the trajectory it has been given, and delivers a command – whose resolution may also be finite – to the robot's actuators.

Any data that has not been recovered via the sensors must be calculated by separate means. For example, a controller without any force sensor must be able to evaluate the forces on the degrees of freedom if it is to compensate for it. This evaluation must be included in the control block.

The closed-loop controller uses the feedback from two sensors per degree of freedom. The first one, the motor sensor, is linked to the rotation of the motor; its resolution is supposed to be infinite. The other sensor is linked to the actual axis of the movement; its resolution is supposed to be finite; this sensor is the joint sensor. In order to avoid current and, therefore, torque surges that may lead to undesired vibration of the whole structure, the command is a current command. Each motor amplifier receives it as digital data.
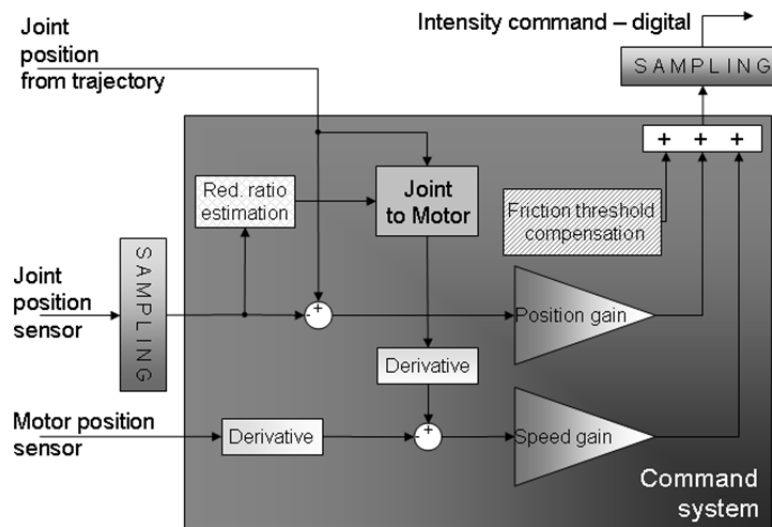
Fig. A-12: Diagram: Controller.

The closed-loop control is constructed using the joint reference calculated from the trajectory. Joint position is given by the joint sensor, but joint velocity must be computed from the motor sensor. However, the controller needs the reduction ratio in order to compare the trajectory velocity with the velocity obtained by derivation of the motor position. This velocity is estimated using the articulation position given by the sensor. The error is then transformed into a motor current using a Proportional–Derivative controller design. As a result, the gains in the closed-loop control will have to integrate the reduction ratios of the system as well as the coupling factor.

In addition to error compensation, the controller compensates for an estimation of the threshold friction in the actuation chain and for the amount of torque it must supply.

8) Post-processing

At each step, the simulation program saves the input fed into each block. Once the simulation has been computed, this data can be individually fed back into the models in order to retrieve information that is not required for any simulation (for example, stress on a mechanical part, position of a point of interest in the robot, etc.) and that has therefore not been computed during the simulation itself.

The trajectory data can also be fed into the flexible model block. This way, the trajectories for all the different bodies are retrieved and may be compared to the actual path of the bodies. The distance point to point of these paths is the tracking error of the robot. Unitary vectors or points as well as bodies may be compared this way.
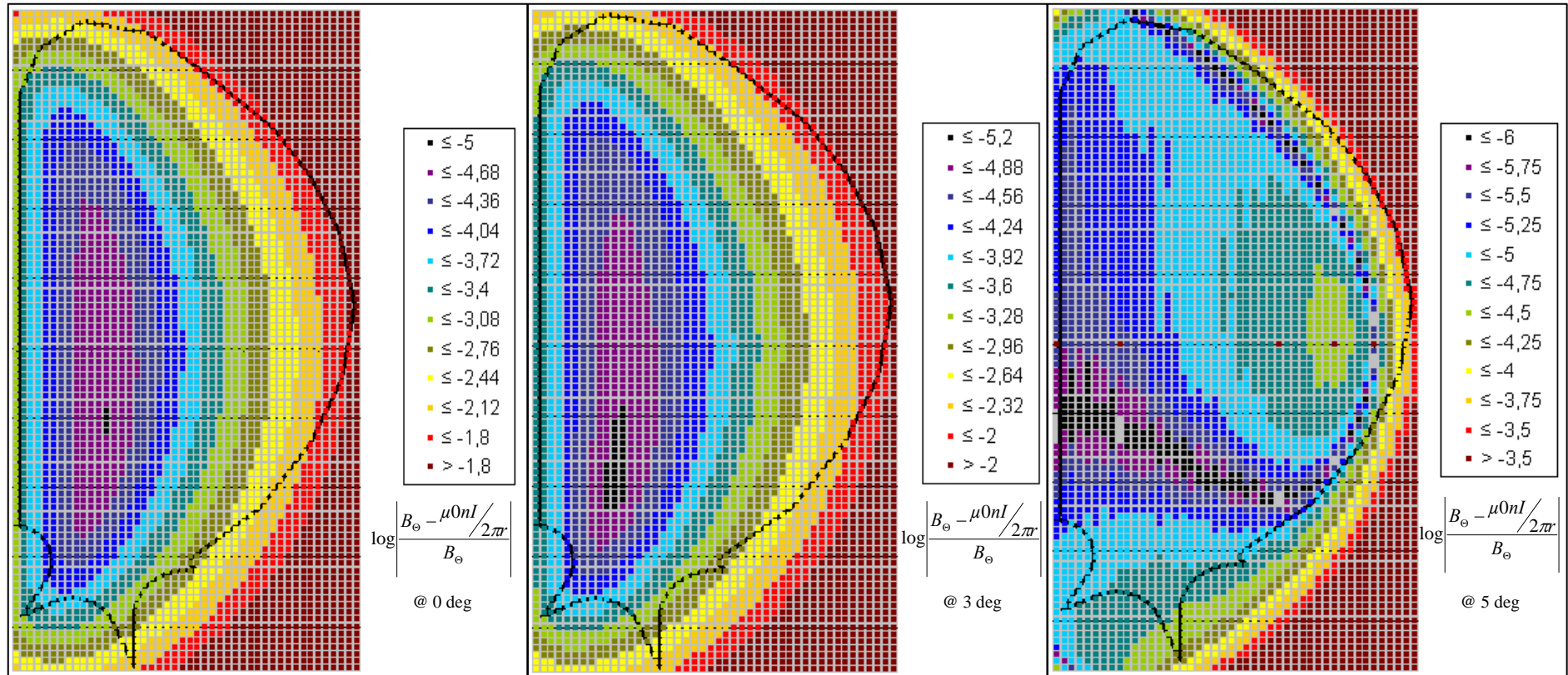
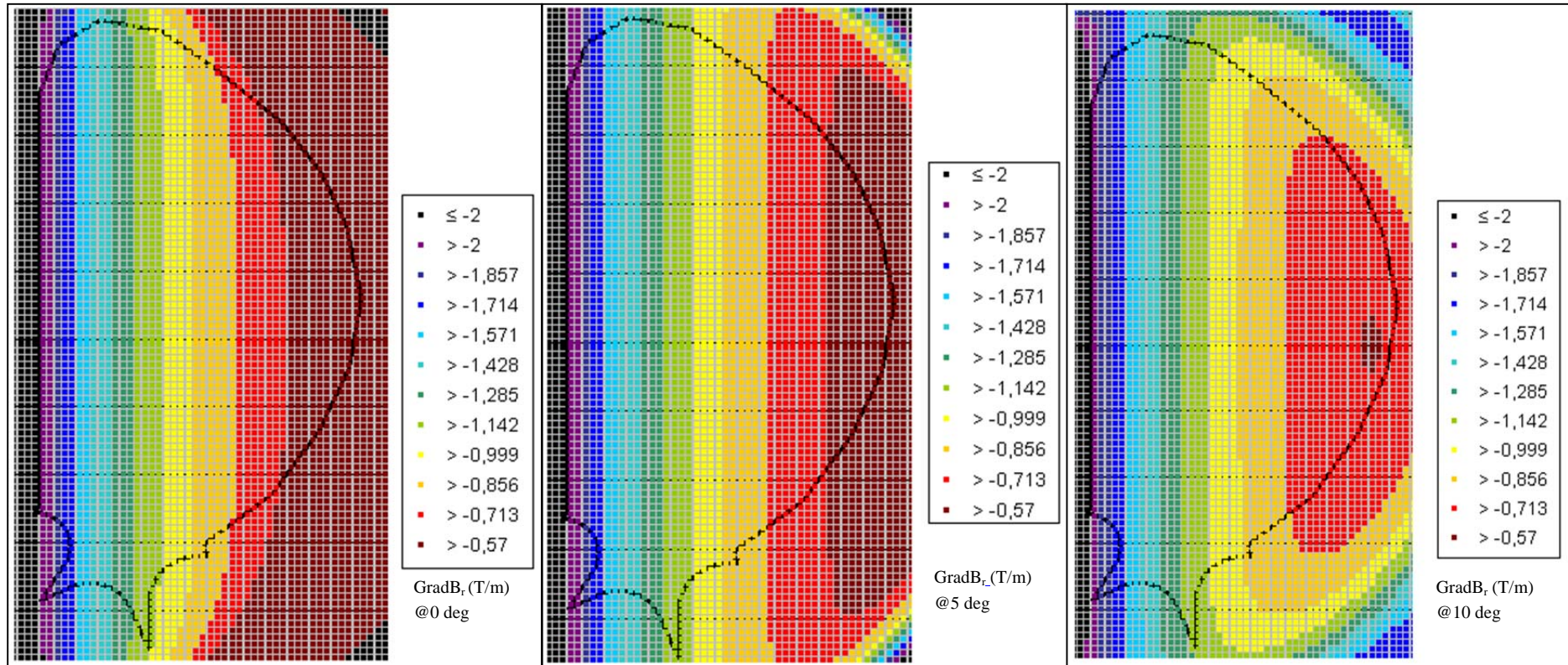## Appendix C.   ITER Toroidal Field Cartography
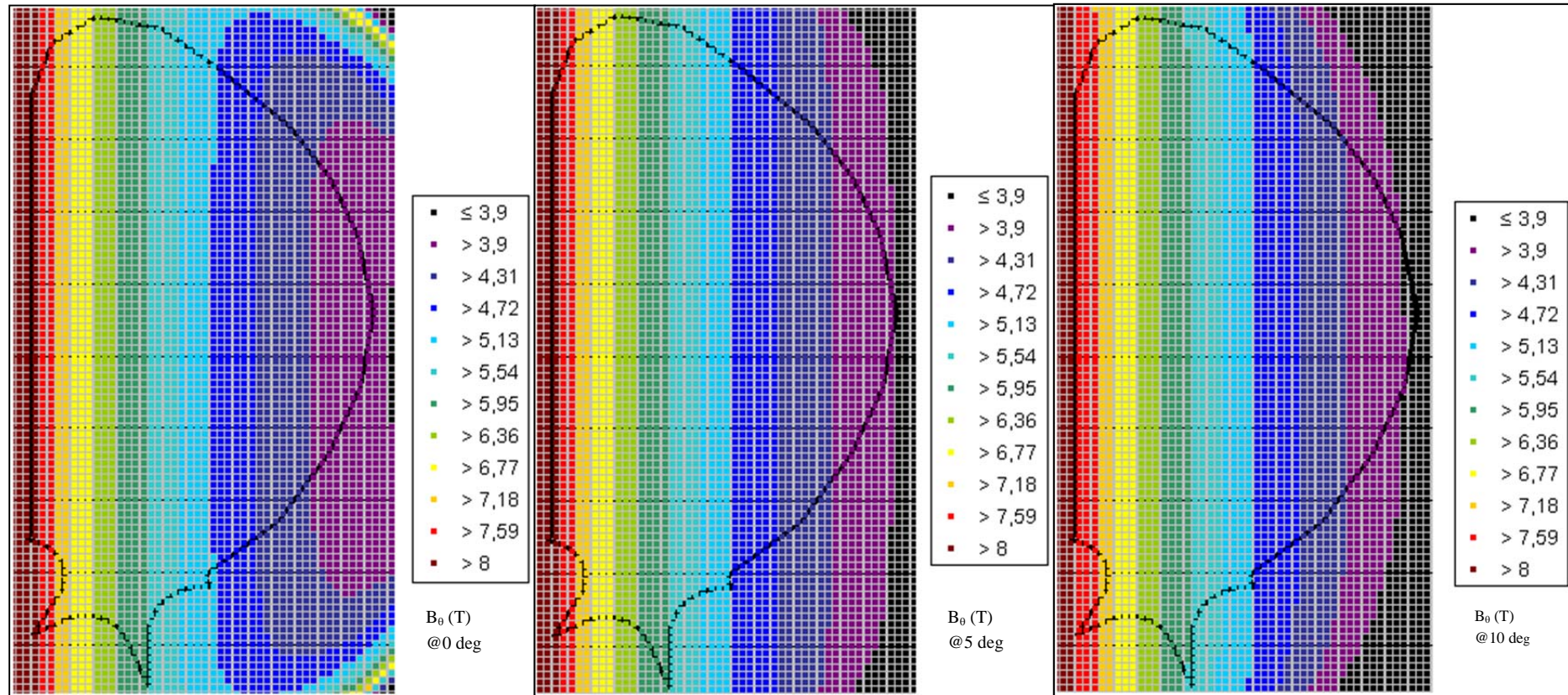
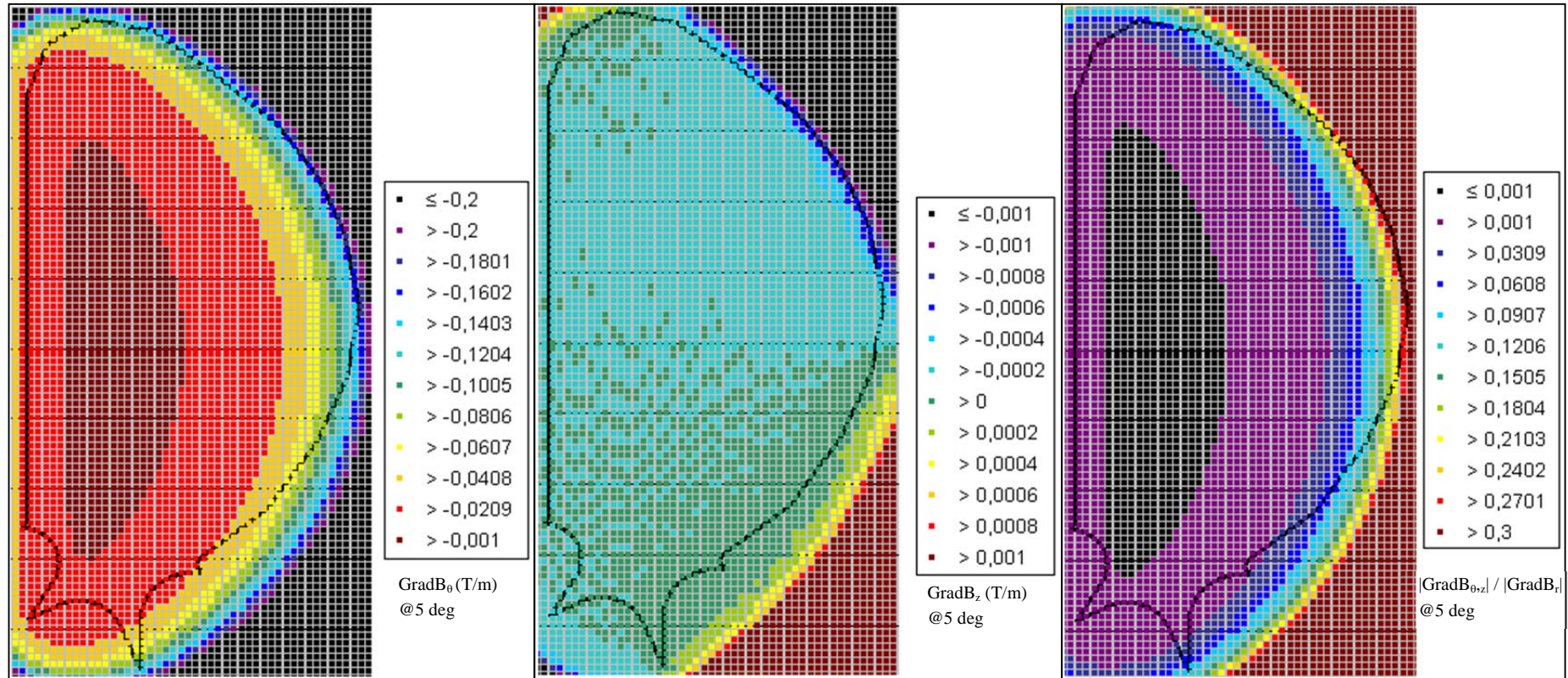Toroidal field values at different toroidal angles.
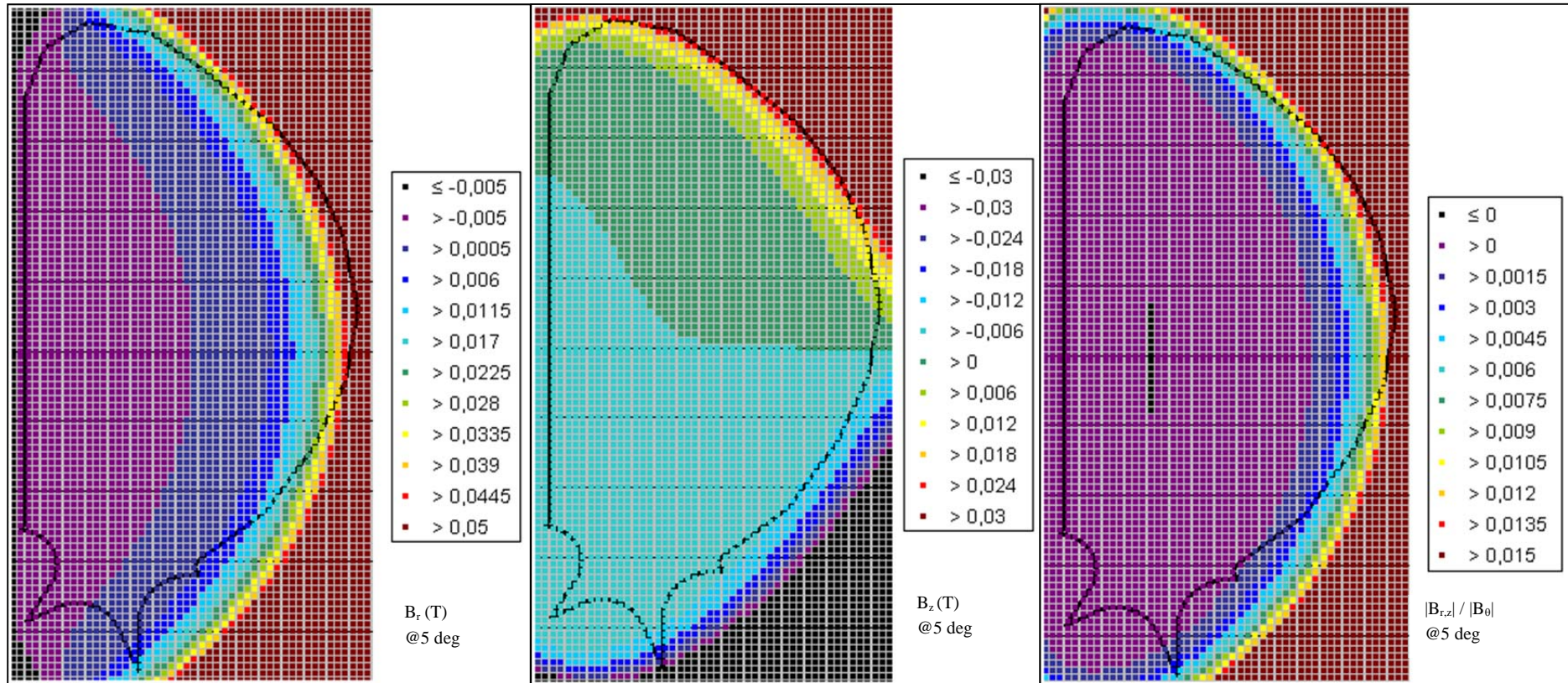
Components on r and z of the field and ratio against the toroidal component at 5 deg.

Relative difference between toroidal component value and Ampere's law approximation in logarithmic scale.
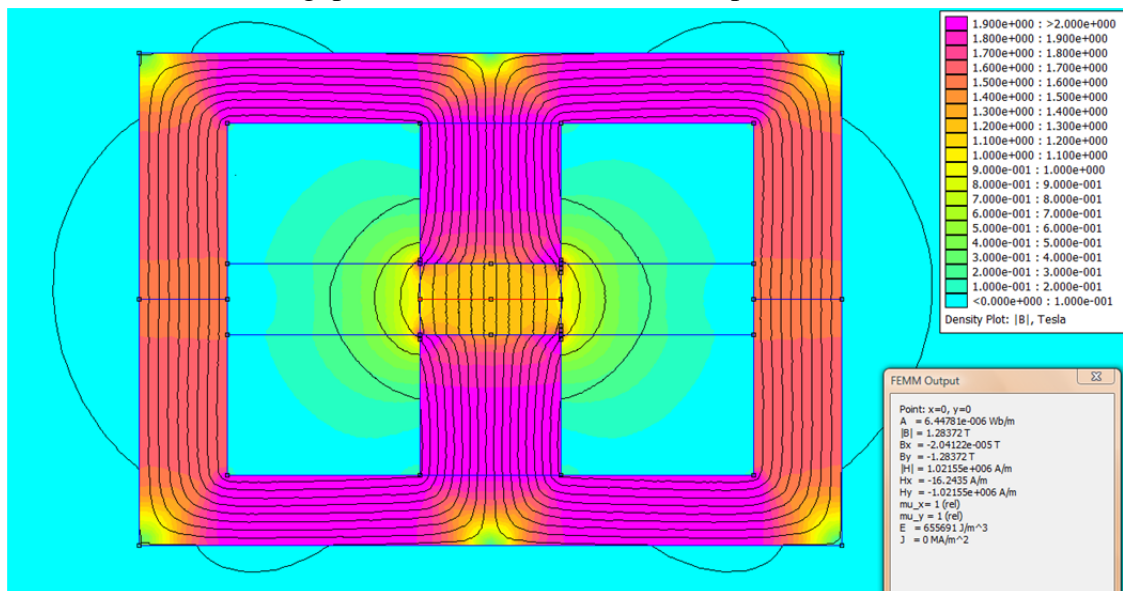
Radial gradient values at different toroidal angles.

Components on r and z of the gradient and ratio against the radial component at 5 deg.

Appendix D. Magnetic field generator field maps

Field maps are computed with the nominal 1038 saturation field at 1.5 T, with a coil current of 400 A.

Flat (nominal): air-gap is constant at 40 mm. Centre point field is 1.28 T.

Slope +2.5 mm: air-gap length is 35 mm on the right against 40 on the left. Centre point field is 1.32 T.
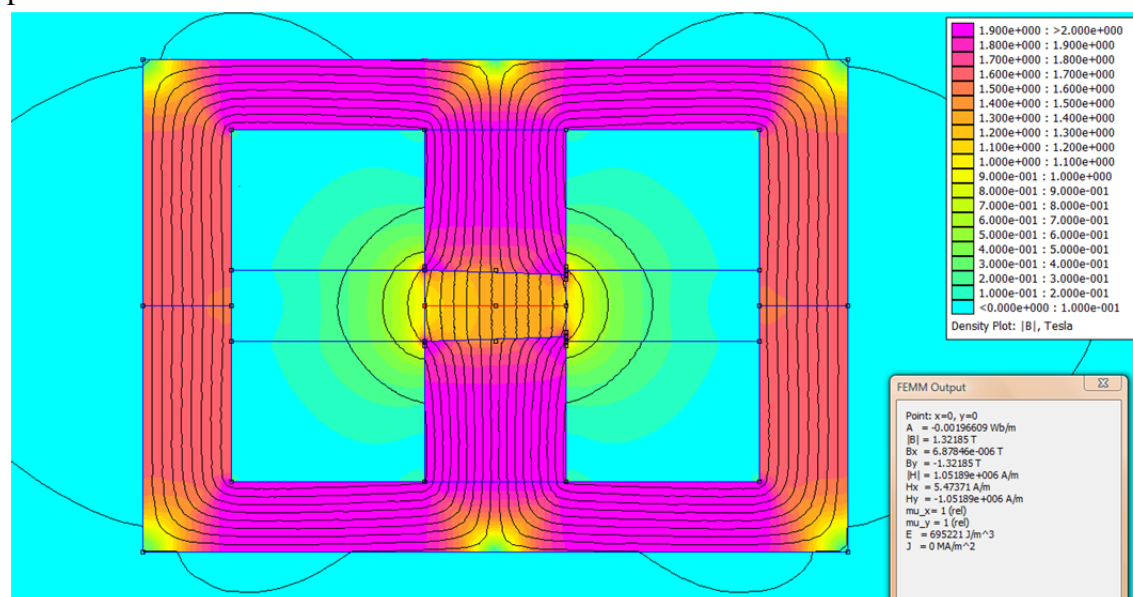
Slope +5 mm: air-gap length is 30 mm on the right against 40 mm on the left. Centre point field is 1.36 T.
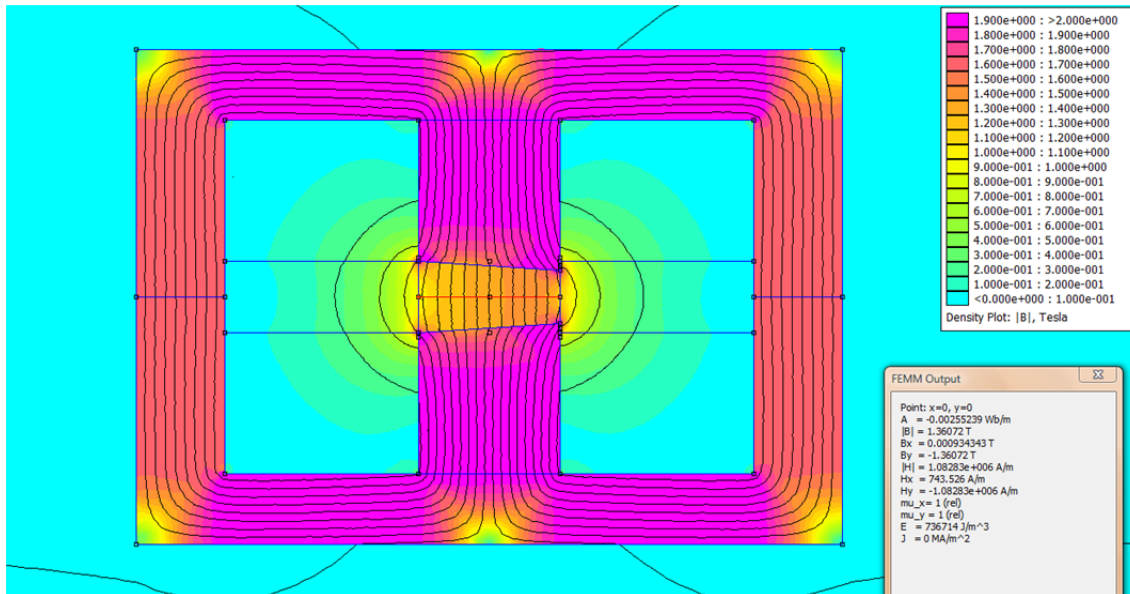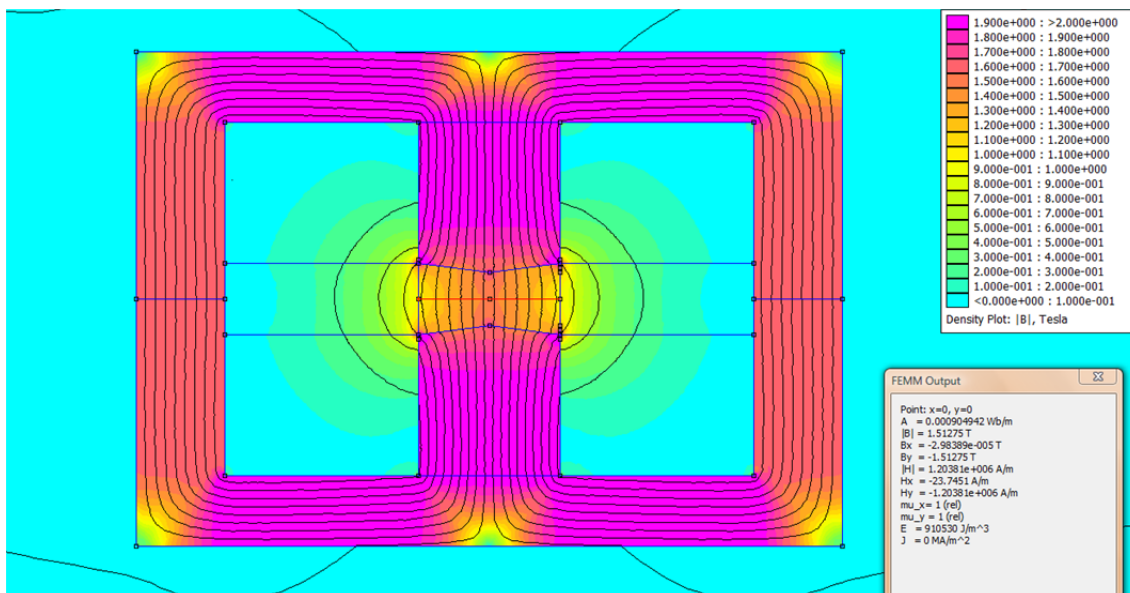

Edge -2.5 mm: air-gap length is 40 mm in the middle and 45 mm on the sides. Centre point field is 1.29 T.
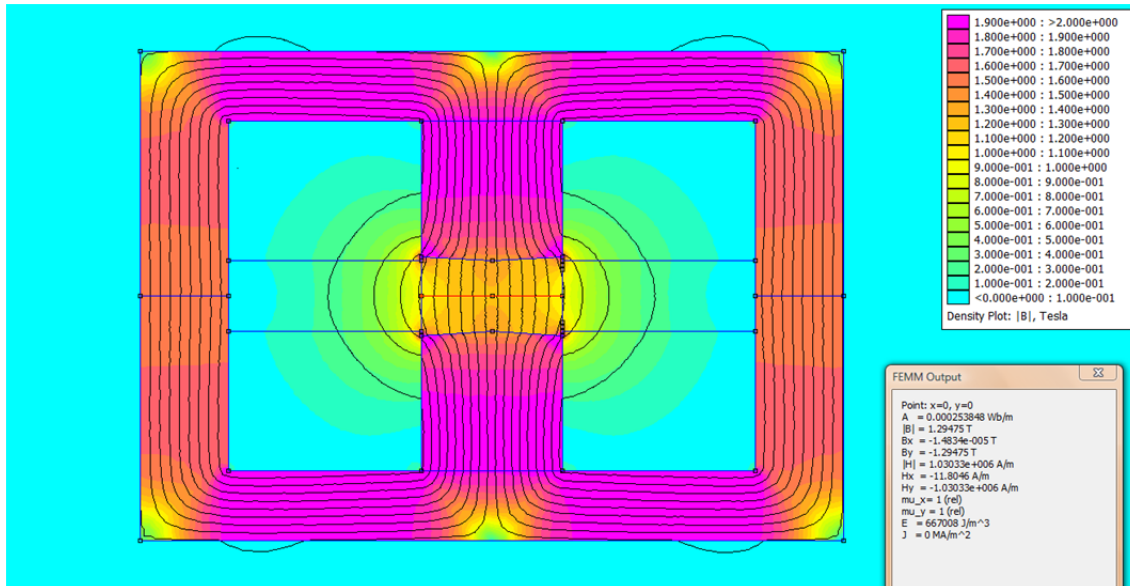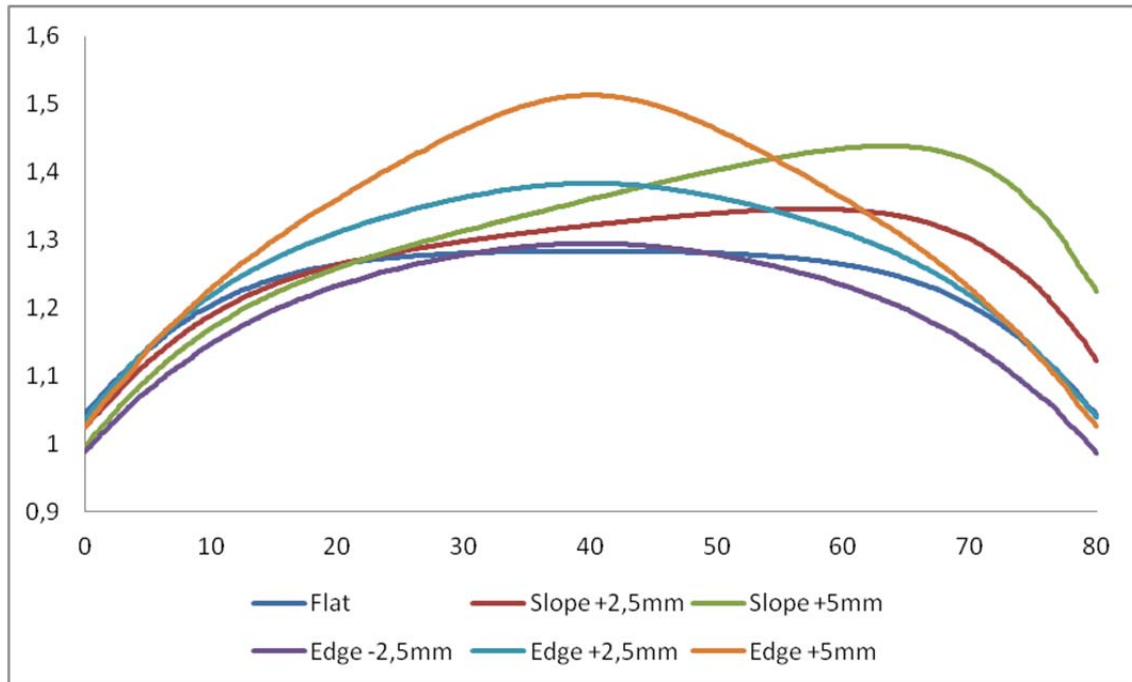
Edge +2.5 mm: air-gap is 35 mm in the middle and 40 mm at the sides. Centre point field is 1.38 T.
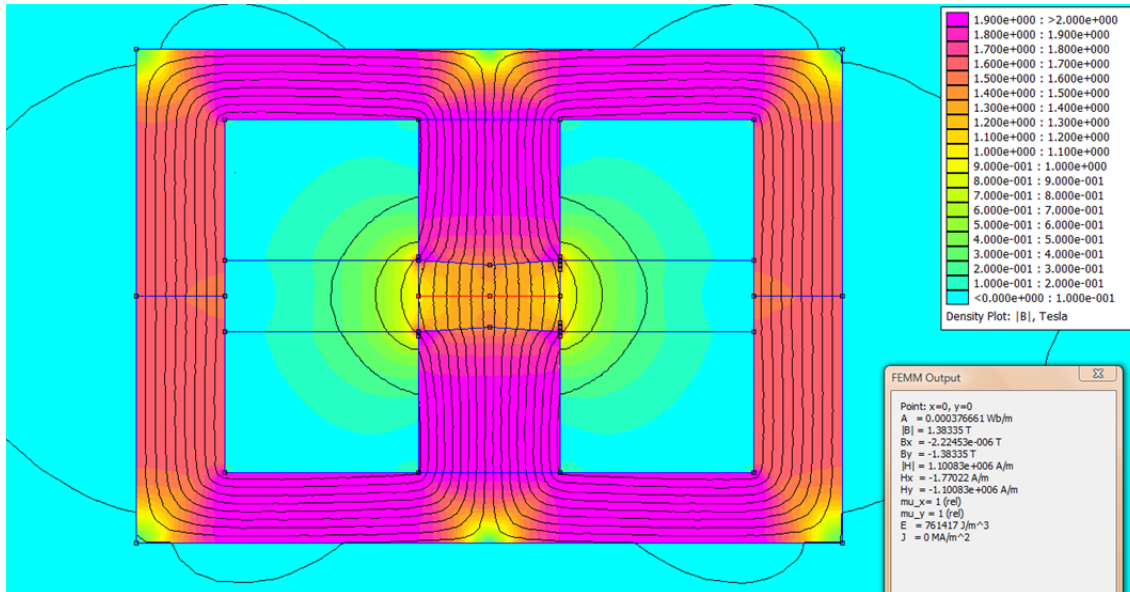
Edge +5 mm: air-gap is 30 mm in the middle and 40 mm at the sides. Centre point field is 1.51 T.

Shown below is the value of the magnetic field for the above maps along the centre line of the air-gap (in red on the images):